DOCTOR OF PHILOSOPHY

The cavitation subharmonic signal
mechanistic source and optimised detection

Johnston, Keith

Award date:
2016

The cavitation subharmonic signal: mechanistic source and optimised detection

By

Keith Johnston

A thesis submitted in fulfilment of the requirements for the degree of doctor of Philosophy (PhD) to the School of Medicine, Nursing and Dentistry, University of Dundee, Scotland, UK.

August 2016

Declaration

I hereby declare that this thesis titled “The cavitation subharmonic signal: mechanistic source and optimised detection” has been prepared by me under the direct guidance of Dr Paul Prentice and Professor. Sandy Cochran as a part of my study for the award of PhD degree at the University of Dundee, Dundee, Scotland. I have not submitted this thesis previously for the award of any degree or diploma at any other institution.

Signature: ..... Date: 01/08/2016

Certificate

This is to certify that Mr. Keith Johnston has done his research under my supervision and complied with all the requirements for the submission of this Doctor of Philosophy thesis to the University of Dundee, Dundee, Scotland.

Signature: ..... Date: 01/08/2016

Acknowledgements

Some three plus years ago, I was fortunate to gain a PhD studentship to study Cavitation. At that time my knowledge of bubbles was insignificant, but through the passion, expertise and dogmatism of my primary supervisor Paul, my knowledge and active enjoyment of studying bubbles has grown, for which I have to thank Paul. They are quite remarkable after all.

My sincere thanks go to my second supervisors Professor Sandy Cochran for his mentoring and encouragement through tough times and Professor Cuschieri for his advice and financial support through CODiR European Research Council (ERC) funded grant. Additional thanks goes to Paul for financial support through TheraCav ERC grant.

Anybody who has undertaken the monumental task of completing a PhD will know it cannot be completed without the help of friends, family and work colleges. Therefore, my gratitude is given to Björn and Spiros for helping me finding my feet at the beginning and teaching me about high-speed cameras and the ways of the lab. In addition, I would like to thank Rui, Xu, Han and Nhan for the early discussion of transducers and ultrasound. Special thanks go to the technicians Graham and Tim for sharing experience, knowledge of device design and general good banter and off course to Cecilia who, although very busy herself, has helped me a lot over the years.

I am grateful to the guys from the CavLab, Kristoffer and Jae for their constructive feedback, help with MATLAB and the odd beer we enjoyed together. I would also like to thank Mariam for letting me use her chamber and help during writing up. To my

good friends Markus, Stuart and Jan, thanks for the happy times spent over BBQ's, which was a much needed requirement to relax from the lab and Helen and Brian, these guys have always been a constant source of joy, chat and were always there when I needed them.

I think the love of and from a partner is the key to success, so I have to whole heartily thank my wife-to-be Julia, for giving me the strength to finish it. Your patience, love and the odd kick-in-the bum definitely got me to the finish line, for which I will be eternally grateful.

Finally, I would like thank to my family for their love and support despite the distance. I would like to especially thank my mum, for her wise advice when nothing else helped and my brother Thomas for sending that application form in the first place; he is always a source of motivation.

Dissemination of Thesis

Publications

Peer-reviewed journals

- **Keith Johnston**, Cecilia Tapia-Siles, Bjoern Gerold, Michiel Postema, Sandy Cochran, Alfred Cuschieri, Paul Prentice. *Periodic shock-emission from acoustically driven cavitation clouds: A source of the subharmonic signal*. Ultrasonics, vol. 54, pp. 2151-2158, 2014.

- Kristoffer Johansen, Jae Hee Song, **Keith Johnston,** Paul Prentice. *Deconvolution of acoustically detected bubble-collapse shockwaves*. Ultrasonics, 2016. (Currently under second stage of review process)

- **Keith Johnston**, Jae Hee Song, Kristoffer Johansen, Paul. Prentice, *Optimisation of a Single Element Passive Cavitation Detector for the Subharmonic Signal*, Sensors 2016. (Under preparation)

Conference papers

- **Keith Johnston,** Sandy Cochran and Paul Prentice.
  Non-linear cavitation cloud oscillations in High Intensity Focused Ultrasound: A mechanistic source of the subharmonic signal. Ultrasonics Symposium (IUS), 2014, IEEE, 373-376.

- **Keith Johnston,** Paul Prentice and Bjoern Gerold.
  Cavitation cloud translation in focused ultrasound. Ultrasonics Symposium (IUS), 2014 IEEE, 61-64.

Conferences attended

- **IEEE** International Ultrasonic Symposium, Chicago Illinois USA, presentation entitled '*Revealing the source of the Subharmonic* signal'. 2014

- Anglo-French Physical Acoustics Conference (AFPAC), Selsdon Park, Surrey UK, presentation entitled '*Cavitation – cloud manipulation in dual frequency focused ultrasound'*. 2014

- National Physics Laboratory Cavitation Forum, Teddington London UK, poster presentation entitled '*Cavitation – cloud manipulation in dual frequency focused ultrasound'*. 2013

Awards

- **Keith Johnston**, Sandy Cochran and Paul Prentice.
  Non-linear cavitation cloud oscillations in High Intensity Focused Ultrasound: A mechanistic source of the subharmonic signal. Ultrasonics Symposium (IUS), 2014, IEEE, 373-376. **(IEEE IUS Student Paper Competition Award)**

- **Keith Johnston,** Paul Prentice**.**
  Cavitation – cloud manipulation in dual frequency focused ultrasound. National Physics Laboratory Cavitation Forum 2013.
  (Best student poster prize)

- **Keith Johnston**, Paul Prentice.
  Cavitation Detector Optimisation using PZFlex. PZFlex User Meeting 2015.
  (Best student poster prize)

Table of Content

Glossary

A	active area	T	transmission coefficient
A_0	amplitude at source	t	time
B/A	non-linear parameter	U_t	particle velocity
c	speed of sound	V	bubble volume
C_0	equivalent capacitance	V_0	open-circuit voltage
d_{3n}	piezoelectric charge constant	V_L	oscilloscope output voltage
C_{MI}	derating factor	V_t	phase velocity
f_c	centre frequency	W	power
f_0	fundamental frequency	x_n	applied stress
$f_0/2$	subharmonic frequency	Z_c	PVdF resistance
f_r	resonant frequency	Z	impedance
F	radiation force	$\lambda.$	wavelength
F_n	Force in *n* direction	ρ	density
g_{3n}	piezoelectric voltage constant	α	attenuation coefficient
p	acoustic pressure	γ	polytropic exponent
p_0	ambient pressure	ε	dielectric constant relative to ε_0
R	reflection coefficient	ε_0	dielectric constant
R_0	equilibrium radius	ω	angular velocity
R_L	oscilloscope input resistance		
t_{ck}	thickness		

Acronyms

- Active cavitation detection (ACD)
- Blood-brain barrier (BBB)
- Computed tomography (CT)
- Extracorporeal shockwave lithotripsy (ESWL)
- fast Fourier transform (FFT)
- Finite element (FE)
- Fibre optic hydrophone (FOH)
- High-Intensity focused ultrasound (HIFU)
- High-speed camera (HSC)
- Cavitation index (I_{CAV})
- Laser-induced bubble (LIB)
- Laser-nucleated acoustic cavitation (LNAC)
- Passive cavitation detector (PCD)
- Passive acoustic mapping (PAM)
- Peak negative pressure (PNP)
- Polyvinylidene Flouride (PVdF)
- Peak-positive amplitude (PPA)
- Magnetic resonance imaging (MRI)
- Magnetic Resonance guided Focused Ultrasound Surgery (MRgFUS).
- Mechanical index (MI)
- Microbubbles (MBs)
- Radio frequency (RF)
- Sound navigation and ranging (SONAR)
- Sonochemiluminescence (SCL)
- Shockwave PCD (swPCD)
- Thermal index (TI)
- Ultrasound contrast imaging (UCA)
- Ultrasound guided Focused Ultrasound surgery (USgFUS)

List of Figures

List of Tables

Abstract

The cavitation subharmonic signal, emitted at frequency values sub-multiple to that of the acoustic driving, is held to be exclusive to the occurrence of driven bubbles within a host medium. Recently, detection of the subharmonic signal has seen a resurgence of interest, particularly for the prospect of cavitation-mediated therapy during the application of focused ultrasound to tissue. Remarkably, bubble-based mechanisms for the origin of the subharmonic signal - which can account for the range of experimental configurations from which it has been detected - have remained elusive since the signal was first identified, by Esche in 1952.

This thesis describes cavitation observations in water, driven by propagating focused ultrasound fields typical of those used for medical therapy, using ultra high-speed shadowgraphic imaging at frame rates well in excess of the fundamental driving frequency. Moreover, single nanosecond laser pulses at energies below the plasma-forming threshold, are used to nucleate acoustic cavitation such that activity may be observed from the outset.

Clouds of densely packed and strongly interacting bubbles are seen to rapidly develop from the nucleation event. Within a few acoustic cycles, the cloud adopts a breathing mode response, with component bubbles collectively oscillating, approximately in-phase. The frequency of cloud oscillation matches that of the fundamental driving, however, at intervals dependent on the pressure amplitude of the driving, the cloud undergoes strong collapses, coincident to emitting a shockwave. In parallel to the high-speed imaging, a number of hydrophone detectors are used to

collect the acoustic emissions, and confirm that *periodic shockwaves* mediate the subharmonic signals.

Acoustic detection of broadband, impulsive pressure transients is particularly susceptible to convolution with the frequency response of the detector. Accordingly, a PVdF needle hydrophone was calibrated for magnitude and phase from 125 kHz – 20 MHz, at the National Physical Laboratory. Detector deconvolution is demonstrated for shockwaves emitted during the formation of large plasma-mediated bubbles, each generated with a laser pulse of energy above the threshold. Similarly, the needle hydrophone is deconvolved from the emissions collected from acoustic cavitation clouds, indicating peak-positive pressure amplitudes for periodic shockwaves in the order of 10 kPa, at the distance detected. The development of a single element passive cavitation detector, dedicated to the detection of low-amplitude shockwaves with high sensitivity, is subsequently described. Detector construction, specifically the selection of matching and backing layers, is guided via a Finite Element model of the device, adapted to support simulated shockwave propagation. Detector performance is characterised with plasma bubble shockwaves, and evaluated for the detection of the subharmonic signal from a cavitation cloud, against a commercially available device.

1 An introduction to acoustic cavitation, and the subharmonic signal

Most attempts to define *cavitation* refer to the formation, and subsequent activity of bubbles of gas or vapour, within a liquid host environment. Beyond that, it is challenging to concisely capture the quite extraordinary range of bubble occurrences and behaviour in nature, and the often pivotal role they play.

One particularly prevalent example is the existence of bubbles in ocean waves, breaking onto a shoreline. Indeed, the crashing sound of a breaking wave may be attributed to the bubble activity within it, and hints at the intimate relationship between bubbles and sound. Perhaps less well known is the critical role that such bubbles have in aerating the seas, or delivering water vapour into the atmosphere, both of which critically influence both local and global climate.

Bubbles and bubble structures can be generated, or nucleated, when a liquid is subjected to tension, or when energy is deposited into it. A solid object moving rapidly through a liquid, such as a ships' propellers or a hydrofoil, can generate the tension required to produce what may be generally termed *hydrodynamic cavitation*. Local heating within a liquid, such as when a saucepan of water is brought to the boil, results in the formation of vapour bubbles. This can also be achieved with rather more precision, via focusing a laser pulse into a liquid, such that a plasma is generated in a process known as optical breakdown. The plasma expands explosively to form a (laser-induced) bubble, centred on the point to which the laser is focused, fig. 1.1.

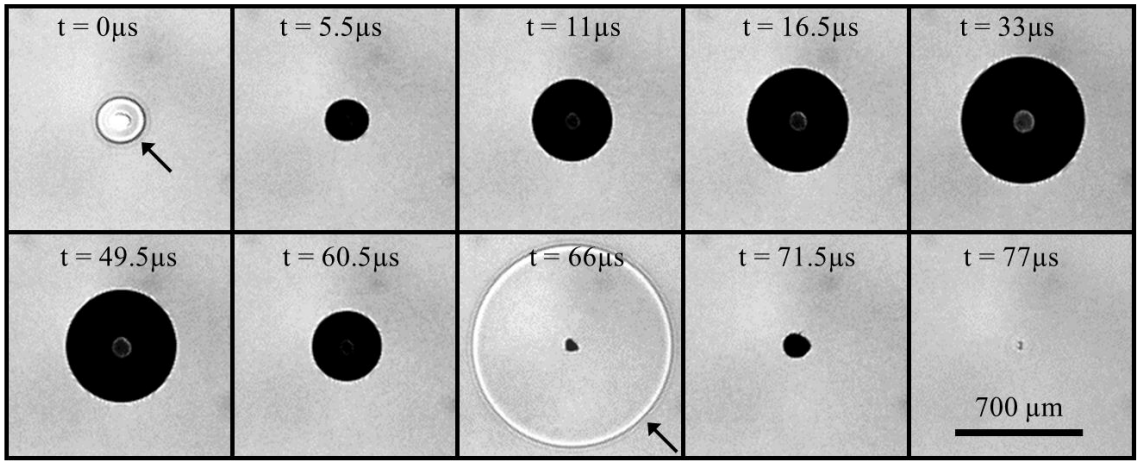

Figure 1.1. The rapid expansion and collapse of a plasma-mediated bubble. imaged with high-speed photography at 2 million frames per second, formed via focusing a laser pulse into water. This process was used for developing a bubble shockwave (arrowed) detector, during the work described in Chapter 7.

Acoustic cavitation refers specifically to bubbles generated within a medium that is exposed to acoustic radiation, of sufficient intensity. Such bubbles nucleate at impurities, including microscopic and sub-microscopic gas inclusions, resident in bulk liquids. The subsequent interaction of these bubbles with the ensuing acoustic wave, however, drives acoustic cavitation into distinctive dynamical behaviour, that sets it somewhat apart from other types of cavitation. For example, a resonance condition exists linking the frequency of the acoustic driving, and the size of the bubble that will tend to form.

Generally, cavitation endures a negative reputation, largely because hydrodynamic cavitation can erode and degrade the surfaces around which it is generated, causing component failure or at least reduction in efficiency and performance of the pump or propeller system. This is testament to the destructive potential of bubbles in liquids. Acoustic cavitation, however, has found constructive application particularly in industrial

contexts, such as acoustic cleaning where it is used to remove contaminants from objects such as surgical instrumentation. Another application is sonochemistry, where acoustic cavitation mediates the degradation of organic pollutants, or the synthesis of nanoparticles.

Over the last 20-30 years there has been a renewed and vigorous interest in the application of high intensity ultrasound, for medical therapy. Current clinical practise for the non-invasive treatment of prostate and uterine disorders, involves focusing ultrasound to achieve targeted heating, or ablation, of diseased tissue. Preclinical development of the techniques for a range of other organs is also underway, with a particularly exciting application emerging for focused ultrasound treatment of the brain (Elias et al., 2013). The occurrence of acoustic cavitation within the tissue hosting the focused ultrasound, can pose a significant risk of collateral damage to healthy tissue, beyond the targeted pathology. Alternatively, if the cavitation could be targeted and controlled – which would certainly require a more thorough understanding of the phenomenon, generally – it could provide a powerful mechanism through which tissue could be locally disrupted, and rendered susceptible to the delivery of chemical therapies, for example. This topic is a vibrant and active research field, with ongoing efforts seeking to demonstrate therapeutic biomedical effects such as reversible disruption of the blood-brain barrier, or blood clot dissolution for treating stroke.

Cavitation bubbles are well known to be sources of sound. Indeed, the relationship that dictates the size of a bubble that may be expected in an acoustic field of a certain frequency, was first investigated in the reverse sense; the characteristic sound (in terms

of pitch, or frequency) that a bubble of a certain size will emit ((Minnaert, 1933), XVI. On musical air-bubbles and the sounds of running water). Much of the literature seeking to develop medical and industrial applications of cavitation, report on the acoustic emissions collected during the cavitation occurrence, by some hydrophone – or cavitation detector - device. The application of a Fourier transform to the signal collected, such that it is represented in terms of its frequency content, is a very common technique. Indeed, the resulting *acoustic cavitation spectrum*, an example of which from this work is presented in fig. 1.2, is a near ubiquitous figure in cavitation publications.

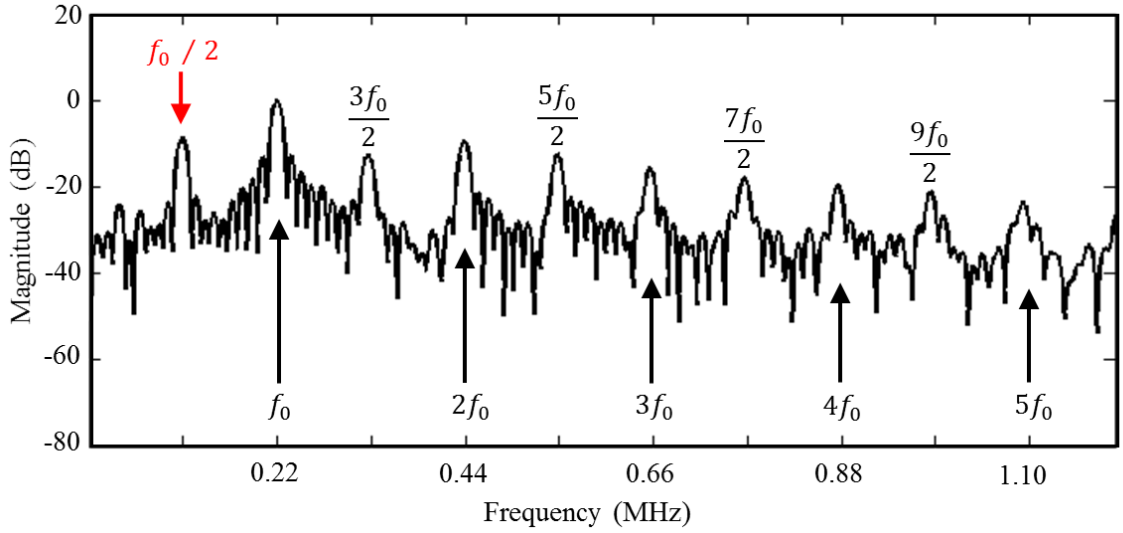

Figure 1.2. A typical cavitation spectrum, generated from the signal emitted by the cavitation activity of fig. 1.3.

The cavitation spectrum is defined relative to f_0, the fundamental frequency of the acoustic driving. For intermediate or high intensity exposures, cavitation spectra will be rich in other features, including peaks at multiple (harmonic) values of f_0, but also submultiple (subharmonic) values, and indeed, higher harmonics of the subharmonic. The cavitation subharmonic signal was first reported by Esche in 1952, ((Esche, 1952),

Untersuchung der schwingungskavitation in flüssigkeiten)[1] and has since been recognised as being exclusive to the occurrence of cavitation. A seminal paper describing the 'subharmonic route to acoustic chaos', for which the order of the subharmonic increases from $f_0/2$ to $f_0/3$, $f_0/4$, up to $f_0/8$ and ultimately broadband white noise across all frequency values, with increasing intensity of driving, was published in 1981 (Lauterborn and Cramer, 1981).

Remarkably, and despite a number of speculative theories having been suggested in the late 1950's to early 1980's, a convincing bubble-based mechanism for generating the subharmonic which accounts for all experimental configurations from which it is detected, has remained elusive. In this thesis a novel experimental configuration, described in Chapter 5 and 6, combining a pulsed laser and high-intensity focused ultrasound (HIFU), is used to study acoustic cavitation clouds in unprecedented detail. Cloud activity is resolved with high-speed shadowgraphic imaging at up to 5 million frames per second, such that impulsive acoustic transients (shockwaves) may be directly observed, fig. 1.3, via refractive index effects. A range of acoustical cavitation detectors are employed to simultaneously monitor the activity, and specific features in the signal collected correlated to the observed cloud activity.

Fig. 1.3. illustrates the key observation behind this thesis; the emission of low-amplitude *periodic shockwaves* (PSWs) from a driven cavitation cloud, coincident to moments of strong collapses within the oscillations. Chapter 5 demonstrates that the

[1] English translation: Study of oscillating cavitation in liquids

frequency of PSW emission is subharmonic to that of the driving, of an order primarily dependent on the intensity. Accordingly, PSWs are proposed as the mechanistic source of the subharmonic signal (Johnston et al., 2014b).

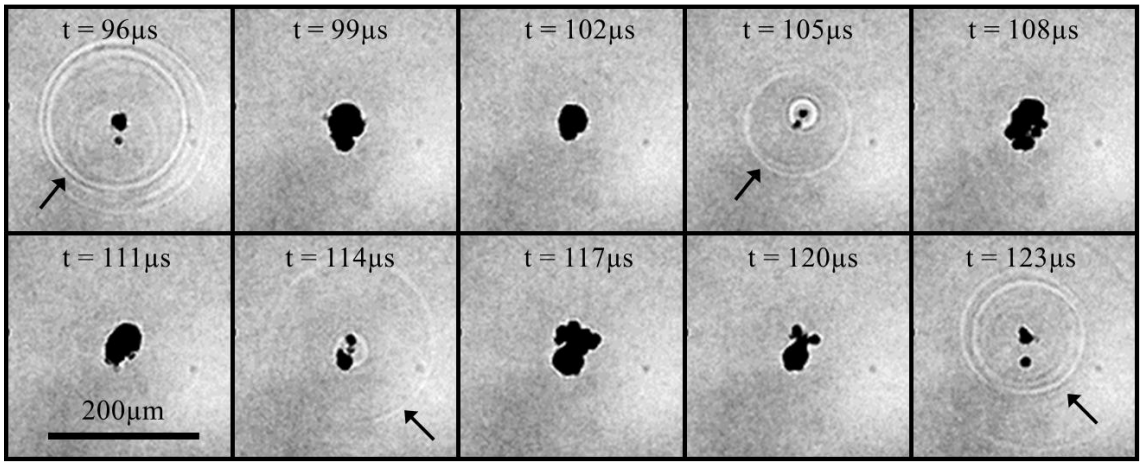

Figure 1.3. Sample high-speed images of an acoustic cavitation cloud, captured at 1 million frames per second, driven by focused ultrasound at f_0 = 220 kHz.

The latter part of the thesis is concerned with the development of an economical and easily constructed cavitation detector, optimised for the detection of shockwaves and therefore the subharmonic signal. The acoustically active component of the *shockwave passive cavitation detector* (swPCD) is commonly available Polyvinylidene Flouride (PVdF) film, due to its broadband sensitivity. A finite element model (PZFlex®) is then used to guide the choice of backing and matching layer materials, with an overriding objective of maximising the voltage output during the detection of low-amplitude shockwaves. The modelling and construction of the device is validated against the highly reproducible shockwaves generated by laser-induced bubbles, fig. 1.1, and the performance for detection of acoustic cavitation clouds, compared to a commercially available PCD.

2 Background

This Chapter is organised to introduce sound as a wave §2.1.1.and review a brief history of ultrasound in medicine, §2.1.2. This will be followed by demonstrating a knowledge of the characteristics of an ultrasound field §2.1.3 - §2.1.6 and a discussion of microbubbles that are commonly for cardiovascular imaging and drug delivery, §2.1.7. Finally, various indices that are used for medical applications, will be reviewed in §2.1.8.

2.1 Overview of ultrasound

2.1.1 Sound as a wave

Sound is truly remarkable; it facilitates the communications of humans, animals and mechanical devices over a GHz frequency range. Sound can be described as a mechanical pressure wave that propagates through a gas, liquid or solid medium transmitting energy. As the wave moves through the medium, energy is transmitted so that particles oscillate and are forced together (compression) or pulled apart (rarefaction). A wave that displaces particles in the direction of propagation is known as longitudinal, as opposed to shear, which refers to perpendicular displacement. Acoustic shear waves only occur in solid mediums; in the experimental results reported in Chapters 5-7, sound waves propagate through water, therefore the discussion is limited to longitudinal waves only. The time-period for a single cycle of compression and rarefaction determines the frequency f_0 of the sound wave. The primary characteristics of an ultrasonic wave consist of frequency, wavelength, speed, pressure amplitude, with secondary characteristics including power, intensity, radiation force and acoustic streaming. Frequency f_0 is related to the wavelength λ and speed of the wave c, using the formulae $f_0 = c / \lambda$. Pressure waves can

be produced by guitars, dependant on the pitch of the vibrating string, with the resulting sound wave, detectable by the human ear when in the 20 Hz to 20 kHz frequency range. Above 20 kHz sound is no longer audible to humans and is now termed ultrasound, below 20 Hz and it is termed infrasound. The vibration amplitude of the oscillating sound wave determines the intensity at which the wave is perceived. Medical applications tend to favour intensity, which is defined as the power radiating per unit area (W/cm^2). Animals such as bats use ultrasound as an echo-location technique for navigation and hunting. Moths and beetles actually use the ultrasonic pulse send by a bat to trigger a reflex action and avoid capture.

The discovery of the piezoelectric effect by the Curie brothers in 1881, encouraged the development of devices to produce (transducers) and listen (hydrophones) to ultrasonic waves (see §4.1). Unfortunately, it would not be until the start of World War I for the electronics to be developed to full utilise the Curies discovery. Physicist Paul Langevin developed a high-powered quartz transducer for the communication and navigation of submarines and ships by Sound Navigation And Ranging (SONAR). Other applications have since been developed including ultrasonic welding of plastics, ultrasonic cleaning of jewellery and surgical instruments. More recently, a major driver for the refinement of transducer and hydrophones has been for ultrasound in medicine, for diagnosis and therapeutic purposes. Typical diagnosis frequencies range from 2 to 12 MHz., and therapeutic from 0.2 to 3.5 MHz (Miller et al., 2012). Diagnostic imaging relies on reflection and scattering from tissue to create high quality ultrasound images. For therapeutic applications, the ultrasound beam is tightly focused to thermally ablate a

cancerous tumour in tissue, using a high intensity focused ultrasound (HIFU) treatment. This will be discussed in more detail in the following sections.

2.1.2 A brief history of ultrasound for therapy

Paul Langevin was also the first to observe the death of fish in the sea and pain in the hand in the presences of high intensity ultrasound (As referenced by (Jagannathan et al., 2009)). The first therapeutic studies started in 1938, when Raimar Pohlman described "therapeutic" effects, when an ultrasound beam was introduced to human tissue. Lynn and Putnam reported the first use of focused ultrasound in 1942 to destroy brain tissue in animals (Lynn et al., 1942). In HIFU, the effect of focusing an ultrasound beam of sufficient intensity initiates a localised rise in temperature inside the focal volume, causing tissue necrosis or a "lesion" to form, fig. 2.1.

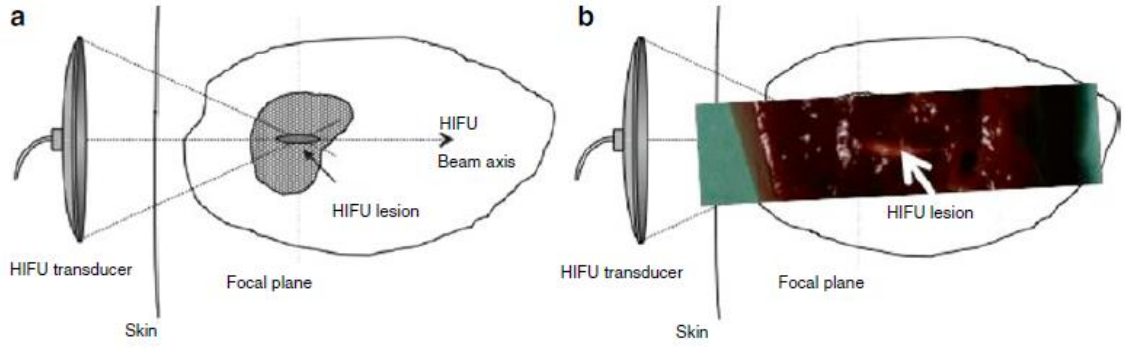

Figure 2.1. (a) Schematic representing the principles of HIFU. (b) Slice of ex-bovine tissue showing a HIFU lesion. Taken from (Escoffre and Bouakaz, 2015).

Successful HIFU treatments depend on a temperature increase between 56-80˚C and of short duration (Ter et al., 1991). Dependant on the pulse length, intensity and frequency, acoustic cavitation (see §3.2) may also occur causing necrosis (Hynynen, 1991). The predictable lesion development from thermal effects was considered more suitable than the unpredictable lesion formation caused by cavitation. This combined with

an established negative reputation cavitation had led to a negative impact of cavitation research in HIFU throughout early experiments.

During the early 1950's William and Francis Fry developed a 4-transducer system, to produce an accurate pinpoint lesion in the basal ganglia brain of a primate model (Fry, 1958). This system was also used to treat humans, suffering from brain disease such as Parkinson's (Fry and Meyers, 1962). Petter Lindstrom applied HIFU for neurological disorders, such as epilepsy, depression and anxiety using intensity over several hundred W/cm^2 (Lindstrom, 1954). In 1956, Burov suggested using short pulses of HIFU for the treatment of cancer, which may produce non-thermal anti-tumour effects (As citied by (Kremkau, 1979)). Since that time, the use of ultrasound to treat tumours has remained a subject of much scientific research. In Japan, many scientists investigated Burov approach to present positive clinical treatments of breast and thyroid cancers (As referenced by (Kennedy et al., 2014)).

During the 1950's and 1960's significant advancement were made to determine the correct frequency, intensity and duration required for successful treatment in neurosurgery. Although these experiments were limited in terms of real time imaging and the need for a cranial window (craniotomies) (Newell, 1963). In 1966, Hill combined the use of ultrasound and chemotherapy for cancer treatment (As referenced by (Kremkau, 1979)), also during this time-period scientists reported results to increase understanding between sensitivity to electromagnetic radiation and ultrasound. During the 1970's many studies investigated raising the temperature above 37˚C to kill cancer cells, successful studies using cell cultures in vitro and experimentally induced in vivo tumours, led to

clinical applications of tumour therapy with hyperthermia which can be combined with radiotherapy or standalone (Wust et al., 2002).

The use of HIFU as a therapeutic non-invasive surgery technique was renewed during the 1970's and mid-1980's, primarily driven by a new image guidance technique to identify tumour locations. A real-time imaging technique was developed using high frequency transducers to generate B-mode (Bright mode) images, combined with FUS, in a technique known as Ultrasound guided Focused Ultrasound Surgery (USgFUS). USgFUS treatment plans included short HIFU bursts of 2 to 3s and increasing acoustic power until hyperechoic regions become visible on the B-mode diagnostic image, which indicated a successful ablation (Ter Haar et al., 1989). A change in grey scale on the B-mode image was also to assess the extent of the treatment care. The success of USgFUS has led to the development of commercial systems that were used in clinical trials for the treatment of bladder, (Watkin et al., 1996) liver and kidneys, (Illing et al., 2005) breast, (Wu et al., 2003) uterine fibroids, (Ren et al., 2007) and bone (Wu et al., 2001). A large number of clinical trials have taken place in China, using focal peak intensities from 5000 to 20,000 W/cm^2 and operating frequencies 0.8 to 3.2 MHz (Wu et al., 2004, Kennedy et al., 2014). Treatment for prostate disease using HIFU can be applied using a transrectal probe (Foster et al., 1993).

Neuroscience research continued during the 1980's using cats and monkey brains without a craniotomy, still using a single element focused bowl. The key difference from earlier experiments was the use of lower ultrasound frequency, in the 0.5 to 1 MHz range, which was shown to minimise distortion of the ultrasound beam upon passage through the skull. However, it was reported that the skull had the effect of distorting and shifting

the foci, which caused excessive heating of the skull (Fry et al., 1981). These problems were resolved by the development of large scale, high powered, hemispherical phased array transducers that could correct for phase aberrations caused by variable skull thickness, fig. 2.2. (Clement et al., 2000). The uses use of such an array with a large geometric gain means the energy loss in the highly attenuating skull can be overcome, and indeed a sharp focus of the ultrasound beam in the brain can be obtained (Hynynen and Jolesz, 1998).

Figure 2.2. Multi element phased array. Consists of 256 individual elements, enclosed in a 3D printed shell. Taken from (Escoffre and Bouakaz, 2015).

However, these early designs still required an invasive diagnosis of the tumour using a biopsy and the placement of an implantable hydrophone to correct for phase aberrations. A major boost to medicine occurred at the beginning of the 1990's by the introduction of *Magnetic Resonance Imaging* (MRI). When a patient is positioned inside a MRI scanner, the hydrogen protons present in water and fat molecules spin on its axis and align with the magnetic field creating a magnetic vector. When additional energy in the form of radio frequency (RF) waves is added, this causes the hydrogen nuclei to

resonate. When the RF is switched off, the magnetic vector returns to its resting state and a radio wave signal is emitted, which is detected by receiver coils and used to create MR images. MRI was combined with HIFU to provide the most advanced imaged modality for clinical monitoring and targeting of tumours, in a technique called Magnetic Resonance guided Focused Ultrasound Surgery (MRgFUS). Also during the 1990's a non-invasive method was developed using phased arrays, requiring a pre-operative high resolution CT-scan, to measure the skull thickness across various acoustic pathways (Aubry et al., 2003). The main problem with this method was that every patient required a time consuming, tailored treatment plan, to apply phase offsets to individual elements (Aubry et al., 2003). Nonetheless, MRgFUS was used for the first successful treatments of patients with malignant glioma in 2010 (McDannold et al., 2010). Further pilot studies demonstrated the effectiveness of the non-invasive method to thermally ablate the thalamus to suppress tremors (Elias et al., 2013). MRgFUS is also used to treat tumours in the liver, renal, and breast (Escoffre and Bouakaz, 2015).

Comparing USgFUS and MRgFUS, MR-thermometry has the advantage of detecting real-time temperature changes during treatment, therefore treatments can be altered before any irreversible tissue damage can occur (Hynynen et al., 1997). USgFUS cannot measure temperature change, a strong hyperechoic B-mode image is actually generated by acoustic cavitation or cavitation by boiling. Additional USgFUS drawbacks include poor tissue contrast, limited field of view and the deterioration of image quality over time, but the treatment is real-time and relatively economical. MRI imaging is more expensive, the MRI equipment is large and noisy and has a lower spatial resolution

compared to CT, the correlation between the focused ultrasound and MR images can be slow and more complex compared to USgFUS treatments.

A potential limitation of transcranial MRgFUS is still the unwanted heating of brain tissue in close proximity to the skull. However, this may be overcome by the introducing microbubbles (see §2.1.7, §3.5.2.) into the blood stream, which reduces the time-averaged power required for transcranial focused ultrasound ablation (As reference by (Jagannathan et al., 2009)). MRgFUS may be the gold standard of imaging modalities (Hynynen et al., 2001b) but it is not mainstream, as the relative simplicity and cost of USgFUS offer an attractive clinical option. Escoffre and Bouakaz provide an excellent and recent review of the current status of MRgFUS (Escoffre and Bouakaz, 2015).

2.1.3 Power and Intensity

Acoustic power is a measure of the amount of energy contained in an ultrasound beam and intensity is measure of power through a given cross sectional area. Diagnostic and therapeutic beams are normally focused, to improve image resolution, and increase pressure amplitude and intensity at the focal region. Intensity varies with both position and time in a beam profile, and ultrasound can be administered in a pulsated wave or continuous. There are therefore many different types of acoustic intensity that exist to characterise different ultrasonic conditions, some are summarised in Table 2.1.

Table 2.1: Spatial and temporal dependent intensities according to HIFU administration modes. Where P is the instantaneous acoustic pressure, ρ is density, c is speed of sound, PRF is the pulse repetition frequency and A is area.

No	Symbol	Formulae	Description
1	I	$P^2/\rho c$	Instantaneous Intensity
2	I_{ta}	I_{Pi}/PRF	Temporal-Average Intensity
3	I_{sa}	$\int I_{ta}\, dA$	Spatial-Average Intensity

A dynamic pressure field can be spatially calibrated using a hydrophone, which detects changes in the pressure amplitude over its active area. A raster scan across the acoustic field can be used to map the pressure gradients and calculate intensity.

2.1.4 Attenuation

As an ultrasound beam propagates through a medium, energy is absorbed due to internal friction effects, intrinsic to the medium. Acoustic impedance Z is a measure of the internal resistance a medium presents to the passage of an ultrasound wave, and is a product of density ρ and speed of sound c. A difference of impedance between different tissue types will result in a reflection, scattering or transmission of the wave at the boundary between them, and this underpins the mechanism behind diagnostic imaging. Thus, the amplitude of the acoustic wave decreases with distance, and is known as attenuation due to absorption and scattering. Attenuation can be calculated using the following exponential formulae:

$$A = A_0 e^{-2\alpha x} \tag{2.1}$$

Where the initial pressure amplitude A_0 has been reduced to an attenuated amplitude A, after propagating a distance x. The attenuation coefficient α is quite variable even for tissue of the same type, in soft tissue, 80% of attenuation is caused by absorption, resulting in the production of heat. The attenuation coefficient of bone is much greater than that of soft tissue. The coefficient is also a function of frequency, such that for both therapeutic and diagnostic ultrasound, higher frequencies are more attenuated. As such, for treatment of the prostate, where a transrectal probe can be used to position a FUS source close to the gland, a relatively high frequency of ~ 3 MHz, is clinically employed

transrectal. For diseases deeper inside tissue, however, higher frequencies cannot be applied, because higher penetration of the acoustic wave is required. Similarly, for diagnostic imaging, frequency is a trade-off between image resolution and depth of imaging. A higher frequency results in a greater resolution but a decrease in image depth, thus to image deeper within tissue a lower diagnostic frequency is required.

Acoustic streaming is a steady flow of fluid driven by the attenuation of an acoustic wave (Wiklund et al., 2012). This type of streaming can occur during medical ultrasound application, where a pool of liquid exists, such as the bladder. Acoustic streaming is 30 times greater in blood, due to increased absorption by red blood cells. Acoustic streaming can be used to differentiate between fluid-filled lesions (cysts) and solid lesions in breasts (Nightingale et al., 1999) or in diagnostic ultrasound to distinguish between stagnant blood and tissue as well as clotted and unclotted blood (Shi et al., 2002). Small scale acoustic streaming, is often termed microstreaming or boundary-layer streaming, occurs near the surface of an oscillating bubble. Microstreaming was first observed by Elder in 1959 (Elder, 1959) and is thought to be one of the main mechanisms to increase membrane permeability (Wu et al., 2002).

2.1.5 Radiation force

If an object is positioned into the path of an ultrasound wave, the wave is reflected or absorbed and results in a radiation force exerted onto the object. The radiation force *F* exerted onto a totally absorbing object, in an ultrasound field of power *W*, is given by (Torr, 1984):

$$F = \frac{W_{absorbed}}{c} = \frac{2\alpha I}{c} \tag{2.2}$$

Where c is the speed of sound in the medium α is the absorption coefficient and I is the temporal average intensity. If a focused acoustic beam exists, the radiation force is applied through the focal region. For a strongly reflecting objects, the force is larger as the net change in momentum of the wave can be up to twice as large, compared to complete absorption, (Fowlkes and Holland, 2000). Some biological effects that are attributed to radiation force, including migration of cells in an acoustic field, cell aggregation, stasis of red blood cells and reduction of aortic pressure in frog hearts (As referenced by (Dalecki et al., 1997)).

2.1.6 Non-linear propagation

In a linear regime, the shape of a sound wave will remain the same as it propagates with distance. For large amplitude waves that are used in diagnostic and therapeutic ultrasound, a linear regime should not be assumed. The speed at which the wave propagates depends on the local pressure. Under non-linear conditions, the phase velocity V_t is greater for higher pressure, compressional regions than lower pressure, rarefaction regions. Increasing the pressure amplitude leads to a greater difference of the phase velocity between the two regions. Thus, as higher-pressure regions move with a greater velocity than the lower pressure regions, the waveform 'steepens' until a shock front is formed. The steepening of the wave front transfers energy from the fundamental frequency into higher harmonics, which are absorbed and the shock front dissipates until the wave ends up as a ('old age'), low amplitude sine wave fig. 2.3.

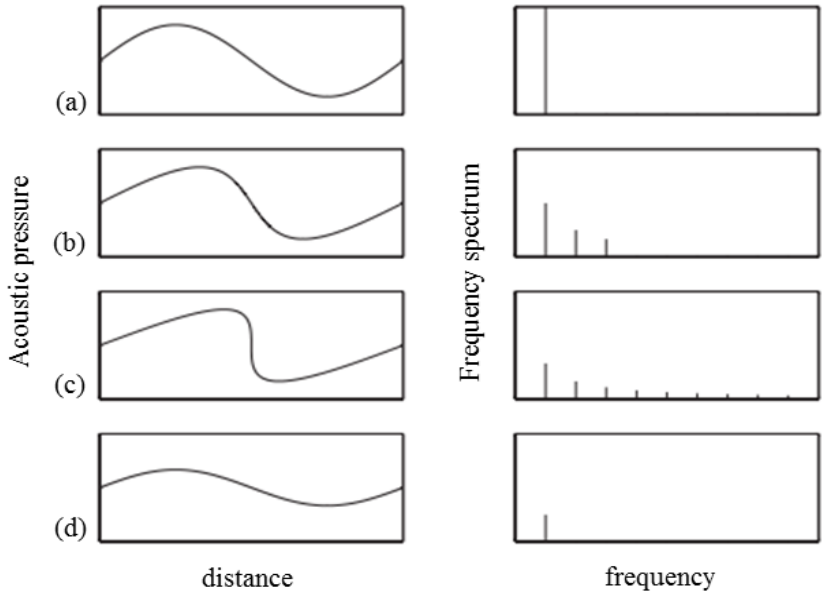

Figure 2.3. Wave steepening and harmonic content due to non-linear propagation. (a) Single frequency large amplitude wave. (b) Steeping of wave front as high-pressure moves at a greater velocity than lower (c) shock formation and harmonic components. (d) Sinusoidal 'old age' due to strong absorption at higher frequencies. Adapted from (Cox, 2012).

An approximation for the phase velocity in relation to the particle velocity U_t, can be shown as:

$$V_t = c + \left(1 + \frac{B}{2A}\right) U_t \tag{2.3}$$

Where c is the wave speed, the ratio *B/A* is known as the non-linear parameter and has its origins from the variation in pressure with density in a medium (Duck, 2002). *B/A* is different for different tissue types, the *B/A* parameter was measured in water ≈5.3, beef liver ≈7.23 and pig fat ≈10.9 (Law et al., 1985). The formation of harmonic components increases the potential for biological effects by the enhancement of heating from the absorption of harmonics (Bacon and Carstensen, 1990). As the absorption coefficient

increases with frequency (§2.1.4. attenuation), higher harmonics are therefore rapidly attenuated.

In terms of acoustically driven cavitation dynamics, a good understanding of the driving field is important, because bubbles directly respond to the frequencies that are driving them. A fast Fourier Transform (FFT) of a hydrophone voltage signal will reveal any harmonic components present in an ultrasound field.

2.1.7 Microbubbles

Microbubbles (MBs) typically have a diameter between 1 to 10 μm and contain a gas core such as nitrogen, or a perfluorocarbon gas, surrounded by a stabilising outer shell, composed of albumin, lipid or a polymer. The small diameter means the MBs can cross the pulmonary capillaries and were primarily developed to enhance ultrasound imaging. The intrinsic compressibility of the microbubbles is ≈ 17,000 greater than water, and therefore they are strong scatters of ultrasound (Kiessling et al., 2012). At low driving pressure, the MBs have a linear response but can generate a non-linear harmonic response with an increase in driving amplitude. MBs are normally injected intravenously into the blood stream and are highly echogenic due to the impedance mismatch between the gas core and surrounding tissue. There are number of commercially available MBs, some of the most common include Definity®, Optison™ and SonoVue® but there are many types under development. Clinically the use of MBs have been established for diagnostic echocardiography, fig. 2.4.

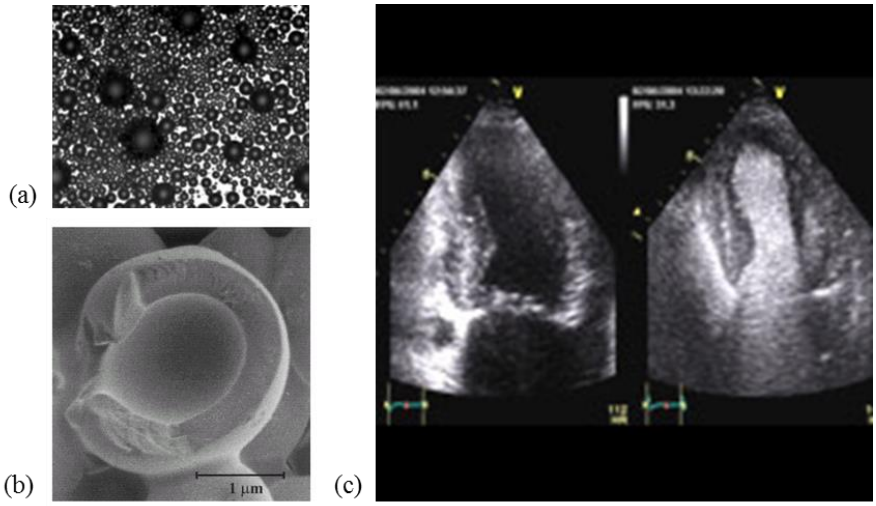

Figure 2.4. (a) Microbubbles are originally developed for enhanced contrast of cardiovascular imaging (a) A solution of MBs of various diameters (b) a ruptured MB shell (c) Diagnostic echocardiography.

MBs can also be used as drug/gene carriers, in the presence of a sound wave the MBs can modify the permeability of the cell membrane, in a process known as 'sonoporation' (Prentice et al., 2005). Targeted MBs that are specially designed for drug delivery via sonoporation have a gas-filled core but a stabilising outer coating where drugs can be incorporated, a targeted ligand can be attached to the surface of the MB to target specific cells or tissue and are widely used for cancer treatment (Ferrara et al., 2007) and blood-brain barrier (BBB) disruption (O'Reilly and Hynynen, 2012). BBB disruption will be discussed in more detail in §3.5.2.

2.1.8 Various indices used for medical application

Power, pressure and intensity are used in diagnostic ultrasound systems to monitor acoustic outputs but individually they are not good indicators for bio-effects, including from thermal and non-thermal (cavitation) mechanisms. If heat is not dissipated in the tissue by conduction and circulation mechanisms, a localised rise in temperature will

occur (Kennedy et al., 2014). The *Thermal Index (TI)* is used to gauge the likely maximum temperature rise in tissue exposed to an ultrasound field and is calculated by:

$$TI = \frac{W}{W_{deg}} \tag{2.4}$$

Where W is the acoustic power from the transducer and W_{deg} is the power required to increase the temperature of the tissue by 1˚C.

The propagation of a pressure wave may also generate non-thermal mechanical effects from radiation force and cavitation. Although the intensity applied during diagnostic ultrasound is relatively low, cavitation may still occur. Thus, the *Mechanical Index (MI)* was developed to gauge the likelihood of inertial cavitation occurring and is defined by the following formulae:

$$MI = \frac{PNP}{\sqrt{f_c}} \tag{2.5}$$

Where *MI* is a dimensionless number, *PNP* is peak negative pressure (*PNP* in MPa) and f_c is the centre frequency measured in MHz (Apfel and Holland, 1991). It is intuitive from Eq. (2.5) that by increasing *PNP* or decreasing frequency increases the likelihood of cavitation too occur. However, this equation gauges the likely hood of cavitation to occur using a single cycle pulse; a modified version of the *MI* was introduced to assess the cavitation threshold and the effect of pulse length:

$$MI = \frac{PNP}{P_{t,n}(f_c, L_p)\sqrt{f_c}} \tag{2.6}$$

Where $P_{t,n}$ is the cavitation threshold as a function of f_c centre frequency and L_p, the number of acoustic cycles. As pulse length increases the threshold for inertial cavitation

decreases, therefore the likelihood of cavitation to occur or *MI* increases (Church, 2005). It is generally accepted that a *MI* greater than 0.4 will result in some adverse bioeffects, such as damage to animal models which include gas pockets (As referenced by (Nelson et al., 2009)) and there is a significant probability of cavitation occurring if *MI* is greater than 0.7. An *MI* of 0.9 was correlated to extensive lung damage in rats when exposed to 4 MHz pulsed Doppler ultrasound (Holland et al., 1996). The *MI* has also been used to correlate bioeffects when MBs are present. For example, an *MI* of 1.6 led to capillary damage using a cardiac ultrasound system in rabbit hearts (As referenced by (Miller, 2007).

The *MI* was originally developed to predict the likelihood of bioeffects from inertial cavitation (see §3.5), Bader and Holland developed a cavitation index I_{CAV} for considering bubble activity as stable cavitation. The index assumes the presence of optimally sized MBs, that rupture and the shell acts as a nucleus for bubble activity.

$$I_{CAV} = \frac{PNP}{f} \tag{2.7}$$

The index gauges the likelihood of the subharmonic emission from stable cavitation, which is defined as the -20 dB ratio of the subharmonic to the fundamental. Most commercially engineered MBs have resonant frequency between 2 and 10 MHz, although Definity resonant frequency for their 10μm microbubble is approximately 0.8 MHz. This model only therefore applies from 0.8 to 14 MHz, and outside this frequency band the I_{CAV} index is no longer valid because sufficiently sized UCA nucleation sites are not present. An $I_{CAV} \geq 0.09$ predicts a threshold for subharmonic emission and potential bio-effects may occur (Bader and Holland, 2012).

3 Cavitation

This Chapter aims to introduce acoustic cavitation §3.2, and the laser based techniques §3.3 that have been fundamental to the obtaining the results discussed in Chapters 5-7. This will be followed by explaining the previously reported theories that have been primarily cited in relation to the subharmonic signal, §3.4 and the medical applications that use the subharmonic signal as in indicator for cavitation, §3.5. The only medical application that specifically use shockwaves to break up kidney stones extracorporeal shockwave lithotripsy (ESWL) will be discussed in §3.6. However, first a brief history of cavitation research will be reviewed, §3.1.

3.1 A brief history of cavitation research

The industrial revolution, where the effect bubbles can have on the speed and erosion of ships propellers, first ignited interest into understanding the power of cavitation. In 1894, the latest British torpedo boat destroyer “Daring” only achieved 24 knots, instead of the predicted maximum of 27 knots. The engineer Barnaby proposed that a threshold for the propeller speed or a specific tensile strength of water, caused propeller inflow to break down. The problems associated with propeller thrust led to the first cavitation tunnel for studying cavitating flows, developed by Parsons in 1895 and the first photographs of propeller cavitation, in 1911. The cavitation tunnel facilitated a series of experiments to observe propellers rotation at lower rotation speeds 1500 rpm compared to normal operation 12000 rpm, fig. 3.1.

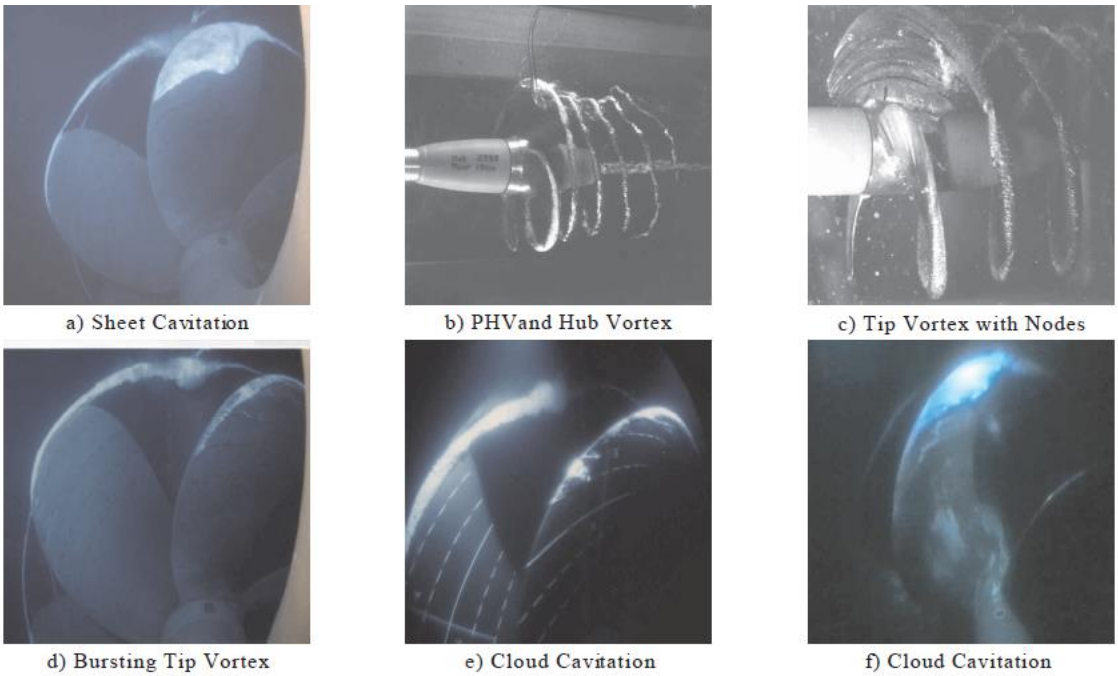

Figure 3.1. Different types of cavitation formations generated by rotating ship propellers. Taken from (Weitendorf, 2001).

The main cause of thrust breakdown was attributed to the formation and collapse of vapour cavities on backside the blade, and was best avoided by increasing the surface area of the blades. Following a proposal by R.E. Froude the phenomenon for harmful propeller damage was termed "Cavitation" derived from the Latin word *"cavus,-a,-um"*, meaning "Hollow". Propeller cavitation is known to affect thrust, vibration and noise experienced on board a ship (As referenced by (Weitendorf, 2001)). The effect of collapsing vapour bubbles, which causing erosion and pitting of propeller blades is still a problem today, fig. 3.2. (Van Terwisga et al., 2009).

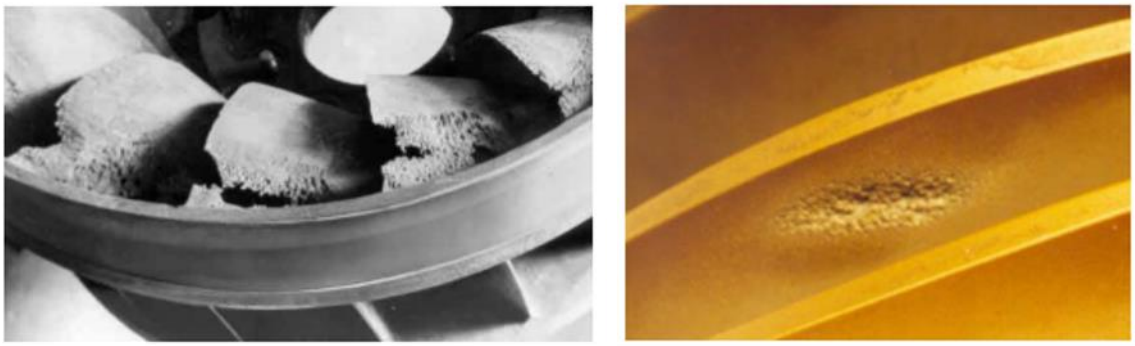

Figure 3.2. Cavitation erosion damage. Blades from a Francis turbine (on Left), localised damage to pump impellor (On right). Taken from (Brennen, 2011).

Lord Rayleigh published the first mathematical model for the collapse of a vapour cavity in an incompressible fluid in 1917 (Rayleigh, 1917). The first biological and chemical effects of cavitation in relation to ultrasound where reported in 1927 (Richards and Loomis, 1927). Marinesco & Trillat observed the blackening of photographic plates when immersed in a water solution, and discovered the emission of light from a single bubble in 1933. The effect was attributed to light emission that was associated with acoustic cavitation by Frenzel & Schultes in 1934. The emission of light from a bubble driven by an ultrasound it termed sonoluminescence, and is indicative of fleeting temperature and pressure conditions in excess of 1000's K and 100's of atm, respectively. This was confirmed in 1949, when Paunoff demonstrated that blackening only occurs at antinodes in a standing wave field (As referred by (Ohl et al., 1999)). Single bubble sonoluminescence and multi-bubble sonoluminescence has been studied extensively using bubble traps (Gaitan et al., 1992). The sonolysis of water, that is the production of free radicals (§3.2 Acoustic cavitation) was studied comprehensively during the 1950's with the primary products confirmed by electron spin resonance and spin trap experiments (As reference by (Riesz and Kondo, 1992)). The high pressure, temperature and free

radicals generated during by a bubble collapse enhances chemical reactions within the trapped gas, for applications including the synthesis of nanomaterials, polymers, or degradation of organic pollutants (Bang and Suslick, 2010). The physical effects attributed to a bubble collapse such as shockwaves and jetting were embraced for industrial processes, such as ultrasonic cleaning of surgical tools or more delicate silicon chips (Mason, 2016).

3.2 Acoustic cavitation

Acoustic cavitation specifically refers to bubble activity driven by acoustic radiation, and has generally been classified in two types: stable (non-inertial) and transient (inertial) cavitation. This classification has its origins in the 1960's, when Flynn used the categories to describe the first visual observation of cavitation activity (As referenced by (Gaitan et al., 1992)). Literature has strongly adopted stable or inertial categorisation, although this classification may be a simplification and a combination of stable and inertial cavitation may occur in an ultrasound field (Church and Carstensen, 2001). At low driving amplitude, a stable cavity refers to a bubble that undergoes low energy oscillations about its equilibrium size for many acoustic cycles and is associated with shape oscillations and surface waves (see §3.4.2.) which results in microstreaming of fluid in close proximity to the bubble wall. This is opposed to inertial cavitation, which refers to high-energy growth, expansion and collapse of the bubble, above a threshold pressure value, fig 3.3. (As referenced by (Apfel, 1981)).

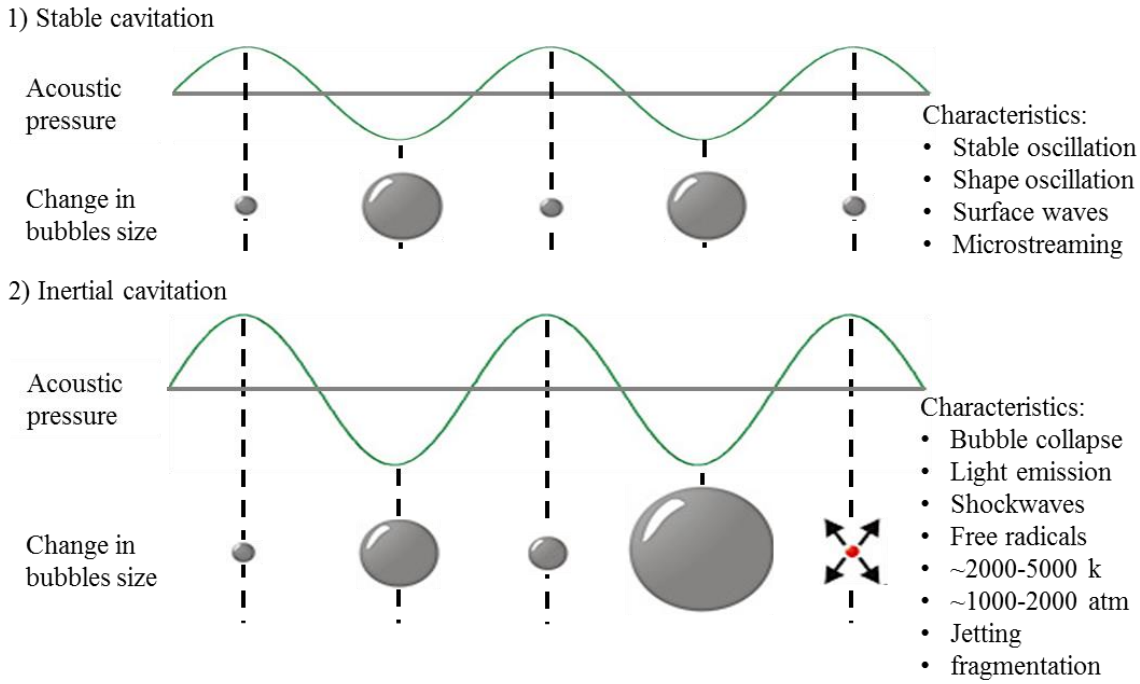

Figure 3.3. Graphical summary for the oscillation behaviour and characteristics associated with stable and inertial cavitation. Low driving pressure amplitudes results in stable oscillation of bubble, depicted here in phase with the applied sound wave, contraction during compression, expanding during rarefaction. As driving amplitude increases, the bubble, grows, oscillates and collapses, and is known as inertial cavitation.

During the final moments of bubble collapse, many interesting phenomena occur; pressure and temperature of the core gas can get so high, that the bubble sonoluminesces, as previously discussed in §3.1. (Gaitan et al., 1992). It is the van der Waals repulsion forces between the atoms or molecules that prevents further compression (Louisnard and González-García, 2011). Under theses extreme conditions water molecules dislocate to generate free radicals (Suslick and Crum, 1998). As a bubble deflates into a strong collapse, the velocity of the bubble wall exceeds the speed of sound and a shockwave is emitted (Brujan et al., 2012). If a bubble is in close contact with other bubbles or surfaces, irregularities or surface instabilities of the spherical shape may develop, leading to fragmentation or a jetting of liquid through the bubble, directed toward the surface or

other bubbles (Leighton, 1995). When two bubbles approach each other during mutual attraction (see §3.2.3), there is a sudden increase in velocity, they coalesce to form a single bubble and the bubble grows, alternatively a bubble grows via a process known as rectified diffusion (Leong et al., 2011).

Acoustic cavitation is nucleated (see §3.2.4) by decreasing the local pressure, within the rarefactions (see §2.1.1), on the application of sound waves. This is distinct to hydrodynamic cavitation that is formed by a decrease in local pressure by the constriction and release of a fluid flow for example; it is this type of cavitation that limits the efficiency of hydraulic machinery, like turbines or pumps (Suslick et al., 1997).

3.2.1 Resonant frequency

When a bubble is excited by a pressure wave of specific frequency, the wavelength dictates the resonant size of which the bubble will have its greatest radial oscillations. It was Dr Minnaert's pioneering work in 1933 that related the equilibrium radius of a bubble R_0, to its natural oscillating frequency f_r using the polytropic exponent γ, density ρ and ambient pressure p_0, of the gas inside (Minnaert, 1933). This is known as the Minnaert equation:

$$f_r = \frac{1}{R_0}\sqrt{\frac{3\gamma p_0}{\rho}} \tag{3.1}$$

In the case of an air bubble in water, Eq. (3.1) reduces to $f_r = 3/R_0$ (Leighton et al., 1990). In 1949, Blake's Harvard report discussed both experimental results and mathematical development for the growth of a bubble. He obtained an approximate solution where it is assumed that the bubble remains stationary, but its area and gas

concentration vary as if it was oscillating from a pressure wave. The term "Blakes threshold", refers to the calculation of a critical pressure for rapid growth, where the bubble needs to exceed a critical radius (As referenced by (Neppiras, 1980)). Holland and Apfel developed an improved theory for the threshold pressure of inertial cavitation as a function of frequency, initial bubble radius, final collapse temperature taking into account the viscosity, surface tension and density of the medium. For a small radius, ~ 0.1µm surface tension dominates bubble motion below 1 MHz, for larger bubble nuclei ~ 1µm, viscous and inertial forces dominate (Holland and Apfel, 1989). This theory is used to predict the onset of cavitation using the mechanical index (see §2.1.8) from a population of nuclei that undergo growth and collapse in a single cycle of ultrasound. Fig. 3.4. demonstrates the threshold between inertial and stable cavitation, using peak negative pressure vs initial bubble radius as a function of frequency (Apfel and Holland, 1991).

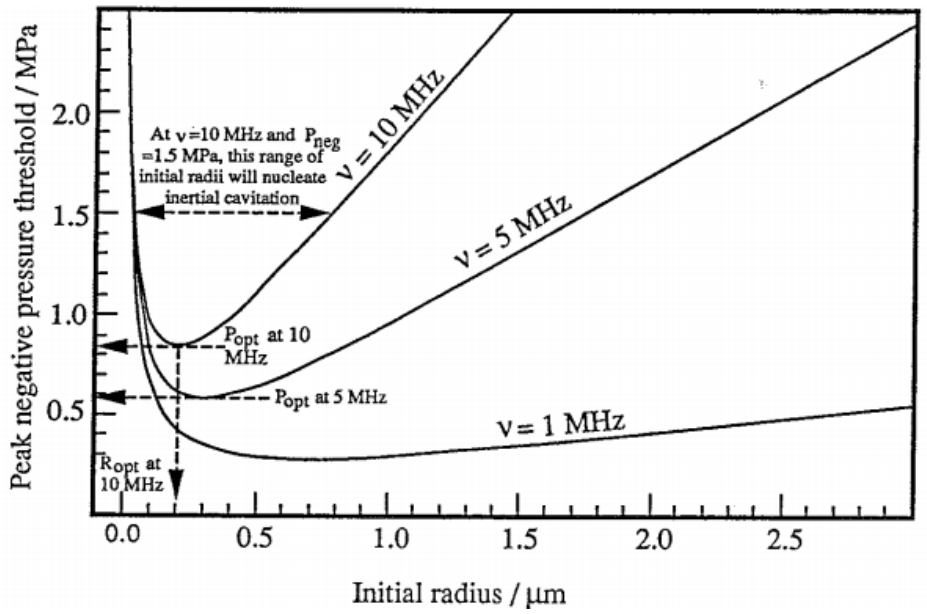

Figure 3.4. Threshold for inertial cavitation, as predicted by Apfel and Holland. The theoretical model illustrates the acoustic pressure required for a bubble to undergo inertial cavitation dependant on the initial radius of the bubble and driving frequency. I.e. At 10MHz and 1.5MPa PNP, inertial cavitation will only be generated if the medium

contains bubbles within the range 0.03-0.77μm. As the driving pressure decreases, the range of bubble radii than can nucleate inertial cavitation decreases. At 0.84MPa, the only bubble radius to nucleate inertial cavitation is 0.2μm. The model assumes nucleation of isolated, spherical, free-floating bubbles in the first acoustic cycle. In reality other nuclei may be present, generated by bubble fragmentation or in the form of stable gas pockets, located in crevices or cracks, these presents a direct limitation of the model to represent real world mediums. Taken from (Leighton, 1997).

3.2.2 Cavitation in a standing wave

In a plane wave standing field, bubbles that are less than resonance size are attracted to pressure antinodes, as opposed to bubbles that are greater than resonance size (see §3.2.1), that are attracted to nodes (Leighton, 1995). From a nucleation site (see §3.2.4), a bubble travels in the direction of a pressure antinode, where a cloud of bubbles occur. The smaller than resonant size bubble moves to specific locations within the acoustic wave, due to primary Bjerknes force (see §3.2.3), during this time it reaches higher-pressure amplitude regions, which allows the bubble to oscillate and grow to a maximum size (Parlitz et al., 1999), via rectified diffusion of coalescence. If, during the translation the bubble grows to size greater than its equilibrium, it either migrates to a node, moves out of the primary field due to buoyancy force or it is subjected to surface instabilities and fragments into smaller bubbles (Strube, 1971). A cloud is quite positionally stable, even at higher driving pressure in a partial standing wave (Thiemann et al., 2011). Dynamic stability can be observed at high intensity in an acoustic cleaning bath, in which clouds can exhibit a double filament layer structure, that form on two sides of a pressure node (Koch, 2014), fig. 3.5.

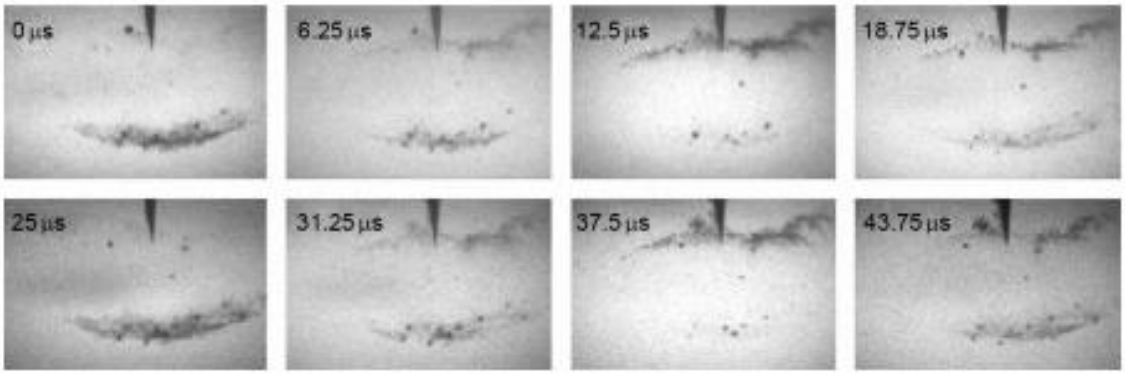

Figure 3.5. Bubble double filament layer driven at 40 kHz. Two periods of the driving sound field are visible (width 1cm), also included is a fibre optic hydrophone visible as a dark tip in the centre of each image. Taken from (Lauterborn and Mettin, 2015).

When a cloud of bubbles is not subjected to standing wave field, they are still responsive to the pressure gradient within an acoustic field, thus primary, secondary bjerknes forces (see §3.2.3), coalescence and rectified diffusion will still apply. In this this work, the sonoptic chamber version 1 (see §5.1.2) and version 2 (see §6.1.2) were carefully designed to avoid a standing wave formation, and the clouds are driven by a purely propagating sound wave.

3.2.3 The bjerknes forces

When a vapour bubble is subjected to a sound wave, the bubble walls undergoes volumetric oscillations, and if a pressure gradient exist within the field, then it couples with the bubble oscillations to create a translation force, exerted onto the bubble. This is termed primary bjerknes force and results in the translational motion of the cloud in the direction of propagation (Johnston et al., 2014a). Bjerknes first identified this force in 1906 but Blake described its origins in 1949 (Blake Jr, 1949). The time averaged force F, on a bubble volume V, in a pressure gradient $\Delta P(r , t)$ can be expressed as:

$$F = - (V(t) \Delta P(r , t)) \quad (3.2)$$

The mutual attraction or repulsion of two bubbles oscillating in a sound field is termed the secondary Bjerknes force. If the radial motion of the bubble walls are in phase and they are of a similar size, which is either larger or smaller than the resonant size (see §3.2.1), then mutual attraction will other. Alternatively, if a single bubble is of greater size than the other, then the volume oscillations are out of phase and they will repel each other (Blake Jr, 1949). A special case exists where if the driving frequency is between the linear resonance of the two bubbles, then they will repel each other (As referenced by (Mettin et al., 1997)). Many authors have investigated the two types of force both experimentally and theoretically (Crum, 1975, Oguz and Prosperetti, 1990, Doinikov, 2001, Pelekasis et al., 2004). The above theories may be a simplification and the dynamics more complicated, if a bubble population density is large and the driving sound wave is of high intensity (Leighton, 1995).

3.2.4 Cavitation nucleation

Theoretically, the tension required for the nucleation of bubbles in pure water is ≈1322 atm. However, in real-liquids the reported experimental pressures for cavitation to occur are much lower, and this is due to stress concentrations or imperfections in the medium (Caupin and Herbert, 2006). If undissolved gas, in the form of very small gas bubbles are present, they can act as nuclei for bubbles to grow, which is termed homogeneous nucleation. Alternatively, if a liquid contains solid particles they can provide a discontinuity between the liquid and solid interface, that can also act as a nuclei and is termed heterogeneous nucleation (Brennen, 2011). If gas-liquid nuclei are present,

the addition of heat at constant pressure or decreasing pressure at constant temperature can cause a bubble to grow. A phase diagram of water can be used to illustrate this concept, fig. 3.6.

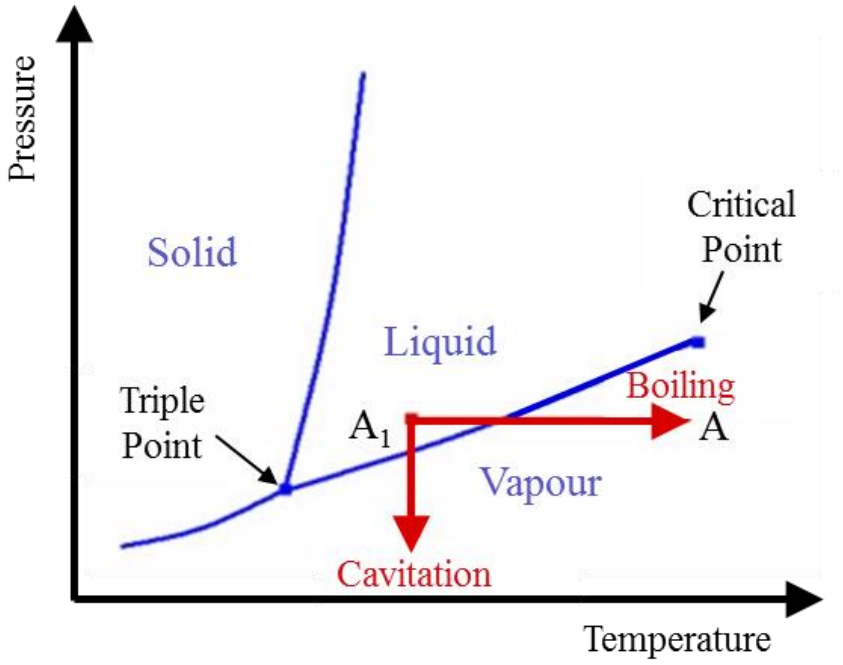

Figure 3.6. Phase diagram of water. The blue line represent the triple point, where all three phase exist and the critical point between the vapour / liquid line. A_1 relates to a liquid at a particular pressure and temperature, which is heated at constant pressure to state A, where A is a state of the liquid that is said to be superheated. Adapted from (Brennen, 2011).

Thermodynamically the two methods of creating a vapour bubble are equivalent, although in reality homogenous nucleation of cavitation is difficult during boiling, bubbles form at the solid / liquid boundary where heat is applied. Cavitation formed by decreasing pressure is typical for an ultrasound wave or a rotating propeller shaft, as opposed to bubbles formed during boiling, which may occur via boiling a kettle. The likelihood of cavitation occurring naturally is greatly reduced by filtering any natural

solid nuclei and removing dissolved gas in the liquid by boiling. The effect of boiling and using deionised water also increases the ability of water to withstand tension (Sedgewick and Trevena, 1976).

Cavitation nucleation may occur in tissue, when the HIFU field deposits enough energy to increase temperature sufficiently (at constant pressure) to cause exsolution, this is a phenomena that cannot arise in non-absorbing media such as degassed water. In this case, the temperate change is sufficiently high that the interstitial liquid can change into a vapour, resulting in bubble formation, and is sometimes referred to as superheating (Crum and Law, 1995). Superheating occurs when a liquid, at constant pressure, is heated to a point that would normally be considered a vapour, point A, fig 3.6. However, starting at A_1 and heating slowly at constant pressure past the liquid/vapour line and the substance can remain liquid, and the state of that liquid is said to be 'superheated'. For example, it is possible to heat water, free of impurities at atmospheric pressure (0.1 MPa) above the boiling point to 180˚C (Young, 1989). However, the addition of impurities would result in immediate vaporisation of the liquid. This effect is thought to occur in tissue and is more commonly referred to as 'boiling'.

3.3 Laser based techniques

Current understanding of cavitation has been limited by the difficulties in studying the phenomenon. A technique known as laser-induced cavitation (LIC) focuses a laser pulse into the medium to create a single laser-induced bubble (LIB), thus the exact timing and position of nucleation can be pre-determined. This facilitates the incorporation of a

high-speed camera (HSC) (see §5.1.2, §6.1.2) to record the bubble dynamics, and passive cavitation detectors (PCD) (see §5.1.3, §6.1.3, §7.1.1) to record acoustic data from the moment of nucleation. When a high powered laser pulse is focused into a liquid medium above the breakdown threshold, a plasma is formed and a 'optical breakdown shockwave' (OBSW) is emitted, fig. 3.7. (next page), followed by the rapid expansion and collapse of the bubble leading to the emission of a secondary 'bubble collapse shockwave' (BCSW) (Hentschel and Lauterborn, 1982). In 1952, Harrison was the first to obtain experimental evidence of shockwaves from a collapsing cavity using schlieren imaging and Guth made the first acoustic measurements of shockwaves in 1954 (As referenced by (Philipp and Lauterborn, 1998)). This technique has been extensively used to study the erosion and pitting effects on hydraulic machinery, caused by the collapse of a bubble in close proximity to a boundary (J R Blake and Gibson, 1987) or the plasma and subsequent shockwave interaction, in intraocular microsurgery (Vogel, 1997). In this thesis, the LIB technique is used to for the development of shockwave PCD (swPCD) for the result presented in Chapter 7.

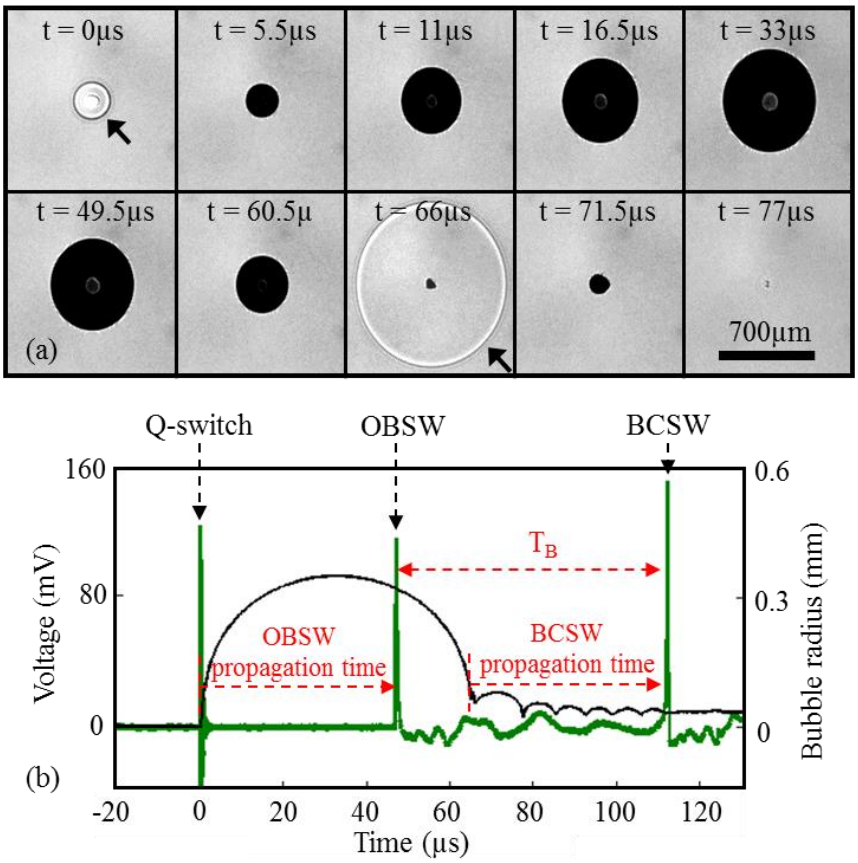

Figure 3.7. HSC images and PCD of shockwaves from a laser-induced bubble (LIB), nucleated with a laser pulse energy above the breakdown threshold (a) Imaging captured at 2×10^6 frames per second. The optical breakdown shockwave (OBSW) and bubble collapse shockwave (BCSW) are arrowed at t = 0 µs and 66 µs respectively (b) PCD voltage signal, positioned ~70 mm from laser focus, with notable features including the laser Q-switch from the pulsed laser, the OBSW and BCSW (arrowed). The bubble radius-time curve is also depicted.

The radial dynamics and shockwaves of a single vapour bubble formed by LIBs are very well understood, but a new technique has been developed for understanding the dynamics of an acoustic cavitation cloud, which is driven by an ultrasound wave. This technique focuses a laser pulse into a pre-established ultrasound field below the optical breakdown threshold, to nucleate a single cloud and the technique is known as laser-nucleated acoustic cavitation (LNAC) (Gerold et al., 2011). The low energy laser pulse

avoids plasma formation, and the large vapour bubble normally associated with this technique. To recap: LIC focuses a laser pulse above the breakdown threshold to nucleate a single LIB that grows, collapses and decays through rebounds. LNAC focuses a laser pulse below the breakdown threshold into a pre-established HIFU field; a single cloud is nucleated and is driven by the HIFU. LNAC technique was used to present the subharmonic results in Chapters 5-7.

3.4 Theories in relation to the subharmonic signal

In 1952, Esche was the first to relate the occurrence of the subharmonic as a feature originating from acoustic cavitation, with experiments recording cavitation emissions from different ultrasonic fields, ranging from 3 kHz to 3.3 MHz. The experimental results indicated that pressure-time waveforms were not very informative but the FFT revealed spectral lines at the fundamental f_0 and harmonics nf_0, but also the subharmonics f_0/n, where n = 2, 4, 8 and 16 were reported (As referenced by (Lauterborn and Mettin, 2015)). Similar experiments of note where carried out by De Santis in 1967 (De Santis et al., 1967) and Vaughan in 1968 (Vaughan, 1968). A number of mechanistic sources for the subharmonic signals have been suggested theoretically and somewhat corroborated experimentally, although the topic has remained the source of ongoing debate.

3.4.1 Acoustic signatures of stable and inertial cavitation

Cavitating bubbles act as secondary acoustic sources, and the spectrum of the signal generated is known to be strongly dependent on the frequency and pressure of the primary insonation, as well as characteristics of the bubble population itself (Lauterborn and Kurz, 2010). Broadly, for a given driving frequency f_0, cavitation can be classified as

‘stable’ at low-pressure amplitudes and non-stable, or ‘inertial’, at higher-pressure amplitudes. At very low pressures, linear bubble response produces emitted, or scattered, signal at f_0. Increasing the pressure amplitude, but remaining within the stable regime, will cause bubbles to oscillate non-linearly, which generates harmonics of the fundamental (nf_0), and weak, often intermittent subharmonic signal ($f_0/2$) and ultra-subharmonics ($(2n+1)f_0/2$). Above a threshold pressure value, inertial cavitation is associated with a marked and sudden increase in broadband white noise, although strong harmonics and subharmonics persist. In addition, higher-order subharmonics (nf_0/m, m > n) become apparent on increasing the pressure amplitude through the threshold value, along with a corresponding set of ultra-subharmonics, above the fundamental (Lauterborn and Cramer, 1981).

The subharmonic has been associated with a range of different ultrasound generated bioeffects, and these will be discussed in §3.5.

3.4.2 Faraday surface waves

It has been suggested the subharmonic may be generated from faradays wave oscillation of the bubble surface. This idea was originally developed by Strasberg and Benjamin in 1958, who compared the dancing motion of trapped bubbles, with the cavitation threshold, theoretically supported by (Eller and Crum, 1970) in 1970 and Hsieh in 1974 (Hsieh, 1974). A bubble can exhibit various shape oscillations when excited by an ultrasound wave (Versluis et al., 2010), fig. 3.8.

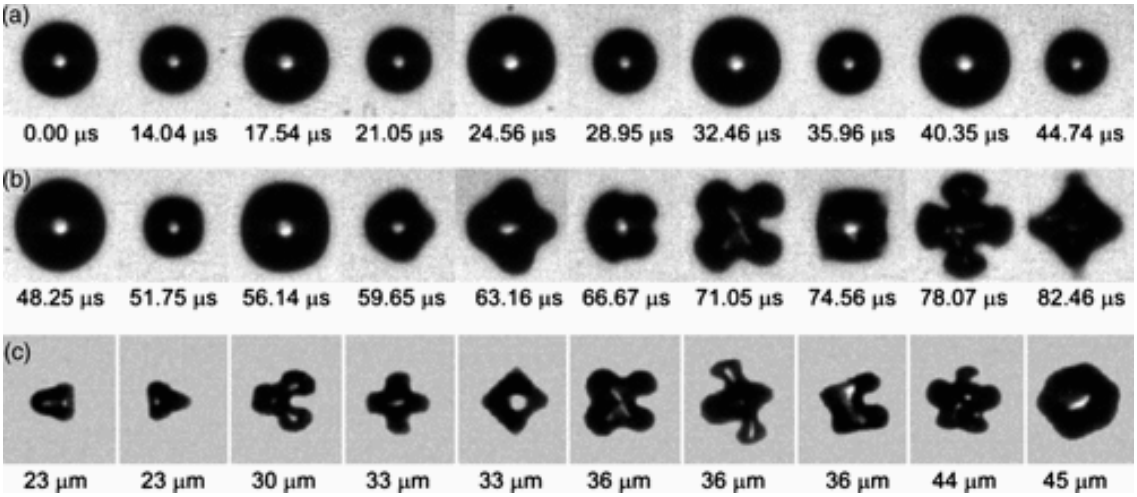

Figure 3.8. Surface oscillation modes of a bubble. (a) the bubble is oscillating in a purely volumetric radial mode (b) bubble becomes shape unstable and surface modes are formed (c) A selection of surface modes from different sized bubble radii (Versluis et al., 2010).

Microbubbles (MBs, see §2.1.7) can also exhibit a surface mode subharmonic oscillation (Yoshida et al., 2015). The major problem with this theory as a source of the subharmonic, is that shape oscillations involve little or no volume change, and the pressure of any surface wave decays rapidly with propagation distance from the bubble (Longuet-Higgins, 1989), but the subharmonic is detected at a range of distance far away from a bubble.

3.4.3 Large bubble theory

The large bubble theory suggests that subharmonic might result from an acoustic field that contains bubbles that have grown via rectified diffusion (Yang et al., 2004) or coalescence (Postema et al., 2004a) (see §3.2) for example to an equilibrium radius that is twice the resonant size (see §3.2.1) of the driving frequency (Leighton, 2012). These bubbles are known to be capable of oscillating at $f_0/2$ (Tervo et al., 2006). However, this is considered to be a less likely explanation for the higher-order subharmonics, owing to

instabilities disrupting a bubble of the required size (Neppiras, 1969). Furthermore, the subharmonic is detected from cavitation occurring in standing-wave fields (Khanna et al., 2003), where larger than resonant bubbles are expected to be forced away from the pressure antinodes, and so this does not provide a wholly satisfactory explanation (Neppiras, 1969).

3.4.4 Period doubling

In 1981, Lauterborn presented experimental evidence for the source of the subharmonic and higher-order subharmonics in a paper entities 'subharmonic route to acoustic chaos', whereby he applied method of chaos in physics to develop a theory relating to "period doubling" (Lauterborn and Cramer, 1981). When a bubble is driven at high amplitude, the volumetric pulsations of the bubble could lead to bifurcation, as the system becomes more chaotic. A bubble oscillator driven by a sound wave of period *T*, underdoes a radial oscillation with the same period *T*. As the threshold increases the subharmonic appears, as the period of oscillation becomes *2T*. The change in oscillation state is called "period doubling", with a further increase leading to a period of *4T*, and after a succession of doublings the bubble oscillations become chaotic, generating broadband noise, (Lauterborn and Parlitz, 1988, Parlitz et al., 1990). Although Lauterborn also stated that subharmonic lines appear in the experimental process that does not follow period doubling, such as the detachment from $f_0/2$ (and $3f_0/2$) to $f_0/3$ (and $2f_0/3$) (Lauterborn and Mettin, 2015).

Chaotic bubble oscillations, which generate $f_0/2$ via period-doubling, and higher-order subharmonics through successive bifurcations, has also received a significant level of theoretical attention. (Eller and Flynn, 1969, Prosperetti, 1975, Prosperetti, 2013).

Clearly, the subharmonic has remained the source of ongoing debate, with the main theories developed during the late 1950's to early 1980's. This thesis provides new experimental evidence for periodic shockwaves (PSWs) as a mechanistic source of the cavitation subharmonic signal, which will be discussed in Chapter 5.

3.5 Specific medical applications of relevance

Having introduced core concepts and terminology in the above reviews of therapeutic ultrasound and acoustic cavitation, two specific applications warrant particular attention, as having relevance to this thesis: blood-brain barrier (BBB) disruption §3.5.2 and extra corporeal shockwave lithotripsy (ESWL) §3.5.3. The former is a particularly exciting and recent application of cavitation-enhanced transcranial FUS, for which the subharmonic signal may play a key role. ESWL employs high peak-positive amplitude (PPA) shockwaves to fragment renal stones (calculi), as an established clinical approach of many decades. It is known that cavitation can occur during the propagation ESWL treatment, and indeed is thought to contribute to stone disintegration; however, the short review is primarily intended to introduce the reader to the concept, and key features, of shockwaves. First, a short discussion will be given of bio-effects that are commonly associated with the subharmonic in focused ultrasound surgery.

3.5.1 Cavitation-enhanced focused ultrasound surgery

From the 1950's many publications, refer to the mechanical effects of cavitation above a threshold level, for lower MHz ultrasonic frequencies. Whilst thermal effects are relatively well understood, the effects of cavitation in tissue have largely been empirical, due in some part to a lack of fundamental understanding of cavitation and cavitation-

mediated effects. The success of USgFUS has maintained some interest into the biological effects of high-powered ultrasound in tissue, as natural monitoring modality for cavitation.

The acoustic detection at the $f_0/2$ subharmonic is commonly used to determine the onset of cavitation in medical therapy, where it has been correlated to a range of associated bioeffects including enhanced heating (Sokka et al., 2003), mechanical tissue damage (Morton et al., 1983), blood-clot dissolution (Prokop et al., 2007), and blood-vessel haemorrhaging (Hynynen et al., 1996). The $f_0/2$ subharmonic is a convenient detection frequency, as the driving intensities typically employed will produce cavitation in the regime where subharmonic emissions are prominent. Moreover, higher harmonics of f_0 can occur in the absence of any cavitation activity, due to non-linear propagation (see §2.1.6) and are therefore may not represent attractive detection frequency options (Muir and Carstensen, 1980).

3.5.2 Blood brain barrier disruption

The blood-brain-barrier (BBB) is a semipermeable membrane that separates circulating blood from the brains extracellular fluid in the central nervous system. The barrier allows essential nutrients to pass but blocks foreign molecules, such as pathogens, which may cause infection or antibodies which are used for therapy (Pardridge, 2002). In 1995, it was shown that by controlling the exposure conditions, the subharmonic can be correlated to the presence of acoustic cavitation, and to the temporary and reversible opening of the BBB (Vykhodtseva et al., 1995). This also sparked a renewed interest in cavitation for therapeutic purposes. In 2001, Hynynen demonstrated that microbubbles (MBs) could be used as a non-invasive method for drug delivery across the BBB

(Hynynen et al., 2001a). Since then, the exact physical mechanism for opening the BBB has been the subject of much debate, and the role attributed to MBs and acoustic cavitation has remained intertwined in literature. There is some conjecture that the MB shell must rupture, crack or release the trapped gas before inertial cavitation can occur. The 'free' collapsing bubble may then cause BBB disruption via localised increases in temperature and pressure, or a high velocity jets and shockwaves. Alternatively, a stably oscillating MBs or cavitation bubbles, in close proximity to cells walls, may cause a localised shear stress and temporary opening of the BBB (As referenced by (Tung et al., 2010a)).

Whilst the exact role from stable or inertial cavitation is still under debate, the subharmonic (OReilly and Hynynen, 2010, Tsai et al., 2016), ultraharmonics (O'Reilly and Hynynen, 2012), harmonics (McDannold et al., 2006, Arvanitis et al., 2012) and broadband emissions (Tung et al., 2010a, Wu et al., 2014) have all been used as an indicator for BBB disruption.

The results in Chapter 5 demonstrate that a cavitation cloud (consisting of 10's of approximately resonant component bubbles) generates subharmonic signal mediated by cavitation cloud oscillations and periodic shockwaves (PSWs) emitted at moments of a strong collapse. It is not yet clear if the subharmonic from acoustically driven MBs is mediated by an equivalent mechanism, although there may be some circumstantial evidence to support the claim (Harput et al., 2011). This will be an important topic for Chapter 8 future work arising from this thesis.

3.6 Extra corporeal shockwave lithotripsy

During the 1980's extra corporeal shockwave lithotripsy (ESWL) was introduced for the treatment of urinary and kidney stones. A typical treatment consists of 1500-3000 shockwaves focused directed onto renal or kidney stones, with the shockwave characterised by steep nanosecond rise from ambient pressure to a peak positive pressure PPA ≈ 40 to 90 MPa, fig 3.9.

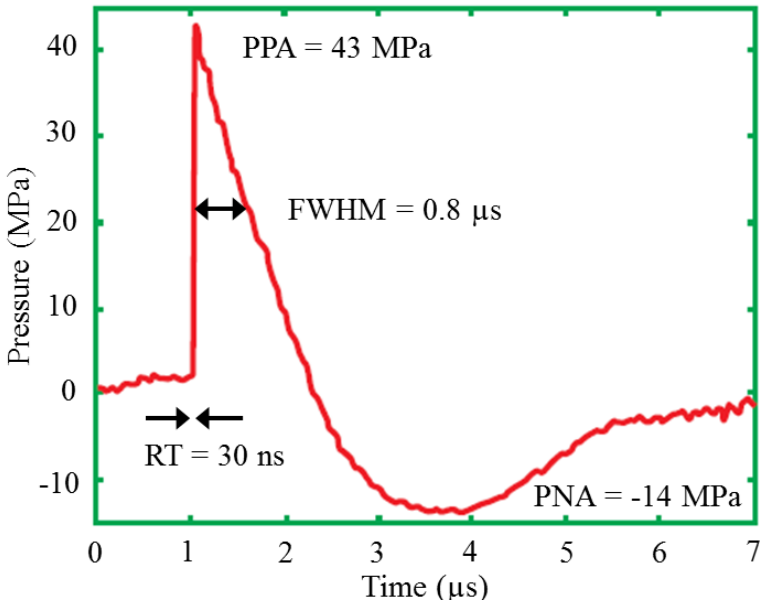

Figure 3.9. A shockwave pressure waveform measured at the focus of an electrohydraulic lithotripter. Depicting typical characteristics of a shockwave, including rise time (RT), full width half-maximum (FWHM), peak positive amplitude (PPA) and peak negative amplitude (PNA). Adapted from (Cleveland and McAteer, 2012).

Mechanical mechanisms such as spallation, shear stress and squeezing are thought to contribute to breaking up stones, but the role of cavitation has been investigated to control fragmentation and minimise potential tissue damage (As referenced by (Leighton and Cleveland, 2010)). Indeed, the non-invasive application of short µs focused ultrasound bursts with an intensity hundreds of times greater than used in diagnostic

imaging but similar to ‘lithotripsy’ is combined in technique called ‘histotripsy’, where acoustic cavitation is the primary mechanism to fragment and subdivide tissue resulting in cellar destruction. The feasibility of histotripsy to create a precise transcranial lesions in agarose tissue phantoms and *ex vivo* canine liver has been investigated (Kim et al., 2014). Acoustic cavitation is also the proposed dominant mechanism to break up kidney stones using HIFU for lithotripsy and a dual frequency control algorithms (Ikeda et al., 2006, Yoshizawa et al., 2009). Lithotripsy clinical treatment plans are developed based on precisely measuring the shockwave created by a Lithotripter using a hydrophone (see §4.1.3), in terms of peak positive, peak negative pressure, full width half maximum (FWHM) and rise time (RT). The RT is defined as the time taken to rise from 10 to 90% of the maximum voltage and FWHM is the time taken for the voltage to rise and fall to 50 % of the maximum.

The negative phase of a lithotripter-generated shockwave is well documented in literature, and could reasonably be interpreted as the detection of a tensile phase, generated by medium response to the propagation of a strong compressive pulse, although diffraction at the lithotripter aperture can also provide a significant contribution to the tensile phase (Zhou, 2012). Acoustic detection of bubble collapse shockwaves (BCSWs, see §3.5) also indicate an apparent negative phase (Krang et al., 2003, Asase and Watanabe, 2004) but it is often not discussed in much detail. Chapter 6 will demonstrate the removal of the BCSW negative phase through full waveform deconvolution, as detected using a needle hydrophone (see §6.1.3) and conclude that apparent negative phases of BCSW are generated by detector convolution artefacts.

4 Cavitation detection

In summary, the previous Chapters demonstrated a knowledge of both ultrasound and cavitation, including the primary, secondary characteristics of an ultrasound wave and how ultrasound has been used for therapy. A brief history of cavitation was reviewed, including the characteristic of acoustic cavitation, various nucleation techniques and specific theories in relation to the subharmonic signal.

The results that will be presented in Chapter 5 and 6 will demonstrate that periodic shockwaves (PSWs) are an important, and previously unreported, component of cavitation emissions, particularly the subharmonic signal and that the peak positive amplitude (PPA) of the shockwaves[2] are relatively low 10's of kPa (see §6.4).

In this Chapter, the implications that low PPA PSWs may have for the acoustic detection of cavitation is assessed, with a review of previous work and detection methods. First, however, it is informative to have some understanding of the sensing materials most commonly used, lead zirconium titanate (PZT) and Polyvinylidene Fluoride (PVdF), which is also necessary for Chapter 7, to aid the development of a shockwave passive cavitation detector (swPCD).

This chapter starts with a review of the history of piezoelectricity, §4.1. The manufacturing process and the principles of how each material generates a voltage response, from the perspective of both an acoustic wave and a shockwave, §4.1.1. This will be followed by a small subsection to compare and contrast PZT and PVdF material,

[2] Note: reported shockwave PPA measurements were undertaken ~70 mm from the cavitation cloud.

§4.1.2. A varied range of hydrophones are designed for free-field measurement of a HIFU field or characterisation of the lithotripsy shockwave, some have also been used to detect cavitation and these will be reviewed and discussed in §4.1.3.

Passive cavitation detection (PCD) is often undertaken using a single element detector; some of which are discussed in §4.2.1. A more sophisticated approach uses an array of elements to spatially and temporally map cavitation fields, §4.2.2. Although the most common methods of acoustic cavitation detection are passive, active cavitation detection (ACD) can also be achieved using a single element or ultrasonic imaging systems, this will be discussed in §4.2.3. A variety of other methods have been demonstrated for measuring cavitation-mediated effects, such as sonoluminescence and free radical production, which are discussed in §4.2.4.

Finally, the Chapter will finish with a review a number of algorithms have been developed for the purpose of quantifying the level or amount of cavitation occurring over time, §4.2.5.

4.1 Piezoelectricity historical overview

The Piezoelectric effect was first discovered by Jacques and Pierre Curie in 1880. The brothers' interest in the asymmetric structure of crystals led to a realisation that applying a mechanical stress to the material generates a proportional electric charge on the crystal surfaces. In 1881, Gabriel Lippman theoretically predicted the inverse piezoelectric effect, whereby the application of an electric field to the crystal causes the material to deform, which the Curies experimentally confirmed in the same year. Together these effects are known as **Piezoelectricity** (Katzir, 2003).

Rochelle salt was the first reported piezoelectric material, initially prescribed as a laxative by the pharmacist Elie Seignette in mid-1600's (Haertling, 1999) but used extensively by the Curie brothers, including other materials such as quartz, topaz, and toumalez. The onset of the first World war led to the development of "Fessenden's" transducers and the more powerful "Langevin quartz-steel sandwich" transducer used by submarines for echo ranging (Sherman and Butler, 2007). World War II increased research using piezoelectric materials in relation to radio communication and subsea acoustic applications, such as the development of acoustic homing torpedoes, acoustic mines and sonobuoys. During the mid-1940's, A.R. von Hippel discovered barium titanate ceramics and in 1954 an even stronger piezoelectric effect was found in PZT ceramics (Jaffe et al., 1954), fig. 4.1.

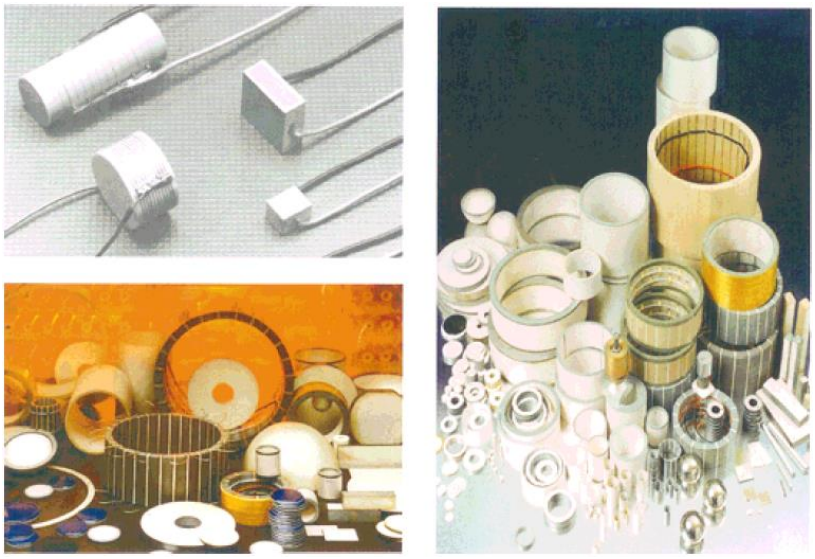

Figure 4.1. A variety of ceramics including PZT that are used in piezoelectric application, such as SONAR, accelerometers and sensors. Taken from (Haertling, 1999).

PZT is still extensively used for underwater transducer and hydrophone applications. Research into the addition of dopants or modifiers, used in combination with

the original PZT composition, continued during the 1950 - 60's. Dopants enhance specific material properties, such as to increase remnant polarisation or high dielectric constants, and reduce aging (Haertling, 1999, Busch, 1987). In 1997 the giant piezoelectric constants and high electro-mechanical properties of single crystal lead magnesium niobate and lead titanate (PMN-PT) were first reported, which has prompted a new generation of electromechanical devices, including transducers, and actuators, such as the ultrasonic imaging probe "Pure Wave" which may ultimately replace traditional PZT ceramics (Sun and Cao, 2014).

PVdF film was discovered before PZT, in 1948, and patented by Ford and Hanford and assigned to E. I. du Pont de Nemours Company, (Edward and Ford, 1948) for use as a flexible coating. The piezoelectricity of the film was discovered by Kawai in 1969, who observed that stretching the film to 5 to 6 times its original length and applying a static electric field, caused the film to exhibit a piezoelectric effect (Kawai, 1969). Researchers have reported a piezoelectric effect in a range of other polymers, including nylon, and also co-polymers of PVDF, such as tetraflouroethylene (P[VDF-TFE]), trifluooethylene (P[VDF-TrFE]), and poly methyl methacrylate (PMMA) (Legrand, 1989, Wada and Hayakawa, 1976, Furukawa, 1989).

4.1.1 Piezoelectricity in PZT and PVdF

A PZT ceramic is created by heating and mixing fine powders of the component oxides of lead, zirconium and titanate in specific proportions, to form a uniform powder. This powder is combined with an organic binder and pressed or moulded into a focused bowl, disk or plate. The PZT is sintered at a specific temperature, for a specific time, where the material develops a dense crystalline structure, connected together at grain

boundaries to form domains and randomly orientated dipole moments. Upon exposure to a strong direct current, the majority of domains align with the electric field, and the ceramic becomes polarised. Removal of the electric field locks the domains, leaving a residual polarisation. A mechanical compression of the surface changes the dipole moment, creating a potential difference (Haertling, 1999, Jaffe, 2012). PZT are characterised by their high impedance (*Z*), which is a product of the density and speed of sound in the ceramic. Typical *Z* values for PZT are between 20 – 40 MRayl, compared with water, which has an impedance of 1.5 MRayl. Due to the high impedance mismatch between the PZT and water, an acoustic wave (or shockwave) will be reflected (*R*) at the water / PZT boundary or transmitted (*T*) into the PZT, according to (Sayers and Tait, 1984):

$$R = \left(\frac{Z_W - Z_{PZT}}{Z_W + Z_{PZT}}\right)^2 \tag{4.1}$$

$$T = \frac{4Z_W Z_{PZT}}{(Z_{W+} Z_{PZT})^2} \tag{4.2}$$

Where Z_w is the impedance of water and Z_{PZT} is the impedance of the PZT. Normally it is desirable for a hydrophone to have the same output voltage per excitation pressure regardless of frequency, so the signal and frequency response can be compared over a frequency range. A typical characteristic of PZT is resonance modes, the lateral or thickness mode for a focused bowl for example. The thickness resonant frequency F_r can be determined by:

$$F_r = \frac{c}{t_{ck}} \tag{4.3}$$

Where c is the speed of sound and t_{ck} is the thickness of the material. If the frequency of a continuous or pulsed acoustic wave is close to the resonant frequency, the voltage output per excitation pressure will increase. However, a flat frequency response can be obtained over a small frequency range between resonant modes. A shockwave, incident to an unbacked PZT detector, may be considered as an impulse function excitation. The component of the shockwave transmitted into the ceramic undergoes a series of reflections inside the PZT at the ceramic / water boundaries that results in a "ringing", manifested as a decaying sinusoidal voltage response at the resonant frequency, fig. 4.2.

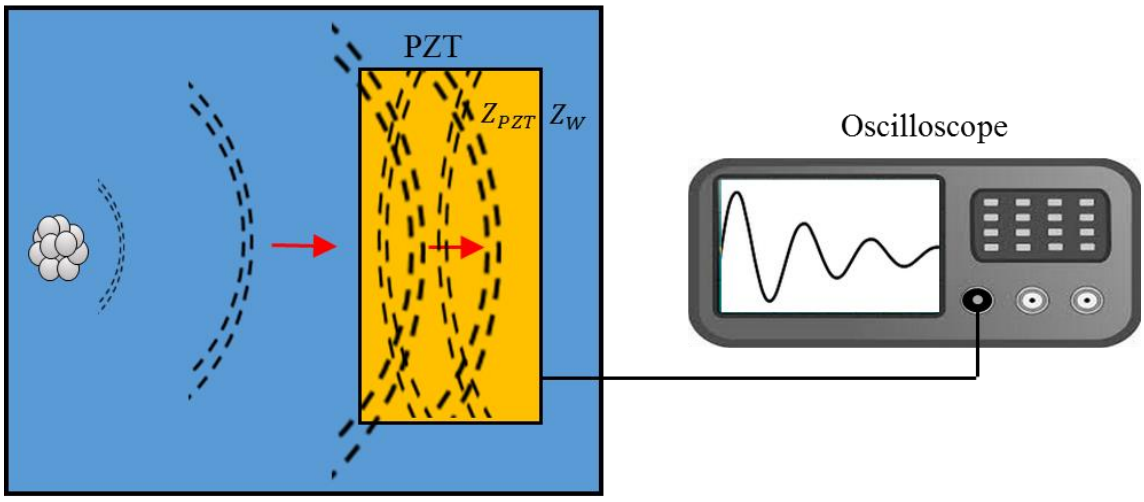

Figure 4.2. Periodic shockwaves from a single cloud interacting with a PZT detector. Shockwave are reflected at the PZT / water boundaries, and inside the PZT due to high impedance mismatch between water and PZT. This results in a decaying sine wave at the fundamental resonant frequencies.

A spectrum of the detected shockwave (without deconvolving the hydrophone response) will result in a large frequency response at the resonance, but limited broadband detection (Cleveland et al., 2000). The addition of a backing layer with an impedance that matches the ceramic, results in greater transmission at the ceramic / backing boundary, which minimises the "ringing" effect. The high impedance of PZT, however, can make it

quite difficult to impedance match ceramics using common backing materials, such as tungsten / epoxy or alumina / epoxy (Wang et al., 2001). Increasing the tungsten to epoxy ratio results in saturation of the mixture at ~10 – 12 MRayl.

PVdF film has an impedance of ~ 4 MRayl, which is closer to that of water and this minimises any ringing effect that is associated with PZT. PVdF has a chemical formulae, (CH_2CF_2), and contains 50% lameller crystals that are up to 100 nm long and a few tens of nm's thick, embedded in an amorphous matrix. PVdF is manufactured as a thin film or sheet with thickness ranging from 9 – 110 µm. The film is stretched or rolled to several times its original length at temperature ranging from 60 to 80°C, which forces the realignment of the carbon chain, i.e. a change in crystalline phase. Electrodes are deposited on the film by evaporation in a vacuum, then the film is exposed to a strong electric field and becomes polarised as it cools. Piezoelectricity is obtained by orientating the molecular diploes of polar polymers in the same direction. The film remains piezoelectric up to its Curie temperature, which is ~ 135°C (Sessler, 1981, Li et al., 2012). When PVdF is used to acoustically detect a pressure wave (sinusoidal or shockwave) a voltage response is generated that is proportional to the spatial averaging over its active area (Kharat et al., 2007).

4.1.1.1 Sensing principles of PVdF film: Thickness and active area

To develop a PCD with the primary aim of increasing sensitivity to low PPA shockwaves (Chapter 7) requires understanding of the effect thickness and active area regarding the output voltage. PVdF generates a voltage response under mechanical deformation. The amplitude of the signal response is directly proportional to the stress and strain applied to the film material. Deformation causes a change in the surface density

so a voltage appears at the electrodes surfaces. The open-circuit voltage V_0 can be determined by (Specialties, 2013):

$$V_0 = g_{3n} x_n t_{ck} \quad (n = 1,2,3) \tag{4.4}$$

Where g_{3n} is the piezoelectric voltage coefficient, x_n is the stress applied in the relevant direction *n*, and t_{ck} is the film thickness, fig. 4.3.

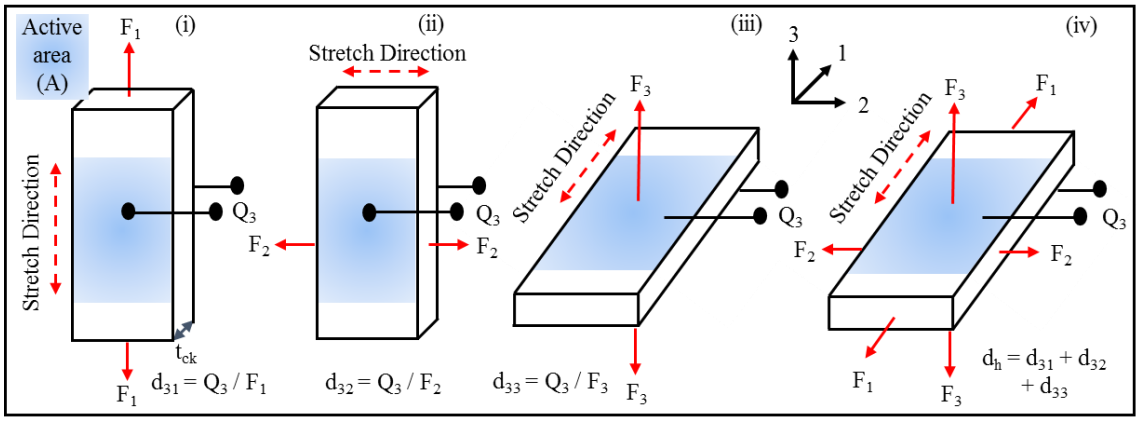

Figure 4.3. Schematic of PVdF piezoelectric coefficients for applied stress (d_{3n}). Orientated to display the three orthogonal directions of PVdF film, where 1 = Length (stretch), 2 = width (transverse) and 3 = thickness direction. Including conductive electrode area (A), thickness (t) and hydrostatic mode (d_h). d_{31}, d_{32} are positive and d_{33} is negative (Adapted from (Tancrell et al., 1985)).

To determining the PCD sensitivity it is more common to use the piezoelectric voltage constant g_{3n}, than the piezoelectric charge constant d_{3n}, which are related through the expression $d_{3n} = \varepsilon\varepsilon_0 g_{3n}$,where ε_0 is the dielectric constant for free space and ε is the dielectric constant relative to ε_0. PVdF has a relatively low dielectric permittivity ($\varepsilon/\varepsilon_0$) compared to PZT, which results in PVdF having a much greater piezoelectric voltage constant compared to PZT, which is essential for high conversion of the mechanical energy of a sound wave into voltage (Li et al., 2012). If a PVdF film is

connected directly to an oscilloscope to record the transient stress / strain response, the voltage on the oscilloscope V_L can be expressed as:

$$V_L = V_0 \frac{R_L}{R_L + Z_C} \tag{4.5}$$

Where R_L is the input resistance of the oscilloscope and Z_C is the resistance of the PVdF film. Z_C is determined by:

$$Z_C = \frac{1}{j\omega C_0} \tag{4.6}$$

Where ω is the angular velocity, measured in rad/s and C_0 is the equivalent capacitance of the film, and can be expressed as:

$$C_0 = \varepsilon \frac{A}{t_{ck}} \tag{4.7}$$

The electrode active area is determined by *A* (Chuang et al., 2012, Specialties, 2013). It is intuitive from Eq. (4.4 - 4.7) that increasing active area and film thickness of an element will result in a greater voltage response to a given pressure wave.

4.1.1.2 The sensing principles of PVdF film: Backing material

The piezoelectric voltage constant is (g_{3n}) is a sum of the uniaxial voltage constants in the 1-2-3 axes (Kharat et al., 2007):

$$g_{3n} = g_{31} + g_{32} + g_{33} \tag{4.8}$$

When an acoustic wave or shockwave propagates through a film that is unbacked or glued around the edges, the film is free to move and a stress is experience on 1-2-3 axes, g_{32} magnitude is negligible but g_{31} and g_{33} are similar in magnitude but opposite in direction. Thus if an equal stress is applied on all axes g_{31} and g_{33} will act to cancel each other out,

and the overall sum g_{3n} is lowered. The film is known to be operating in 'hydrostatic' (volume) mode. The open circuit voltage V_0 is proportional to g_{3n} therefore in this mode the overall output voltage on the oscilloscope is V_L is lowered.

If a backing material is added, an acoustic wave will still cause stress in all three axes but the film is now radially clamped in the 1- and 2-axes, which has the effect of compressing the film in the 3-axis, and voltage constant g_{33} is dominant. The film is now said to be operating in 'thickness mode'. The overall piezoelectric voltage constant is still the sum of all three; the difference being the g_{31}, g_{32} contribution is less, increasing V_0 and therefore the overall voltage output on the oscilloscope V_L.

4.1.1.3 Sensing principles of PVdF film: Matching material

To develop a PCD using PVdF, with the primary aim of detecting PSWs, a protective front layer should be incorporated, to protect the film and electrodes from erosion and prolong the lifetime of the PCD. Additionally, by selecting a matching layer with an impedance value between that of water and epoxy, will increase the efficiency of energy transmitted into the film and decrease the reflected component (Brown, 2000). The correct impedance can be determined by (Szabo, 2004) :

$$Z_{ml} = \sqrt{Z_W Z_P} \tag{4.9}$$

Where Z_{ml}, Z_W, Z_P are the impedances of the matching layer, water and PVdF, respectively. Another important factor in terms of device design is the thickness of the matching layer.

For an acoustic wave, ¼-wavelength thickness of the matching layer is normally selected, for the frequency (and wavelength) of interest, corresponding to maximum

transmission through the matching material. No theory could be found to guide the required thickness of a matching layer for a shockwave. However, an FFT of detected OBSW (see fig. 6.10) and BCSW (see fig. 6.12) indicated the majority of energy is contained within the low frequency part of the spectrum; as such ¼-wavelength thickness was selected for matching materials below 1 MHz using Finite Element (FE) simulations (see §7.2.2) to guide material selection.

4.1.2 Piezoelectric material comparison: PVdF vs PZT

A fundamental basic difference between PZT and PVdF is the material property differences between a ceramic and a polymer film, which has a direct effect on the voltage-time and frequency response. Compared to PZT, PVdF film is often used in hydrophones because it has a good hydrostatic piezoelectric voltage constant, and better acoustic impedance match to water or tissue. The film also has greater flexibility, broadband frequency response, high mechanical strength, linear stability and impact resistance. The material properties of PZT are changeable due to the manufacturing process creating slightly different crystal structures, not only within the same sample, but between different batches. PZTs are brittle and can fatigue leading to cracking over time. The main disadvantage for using a PZT as a PCD is their high acoustic impedance, which results in the ringing phenomena and limited broadband frequency response. Selecting a ceramic that has a resonance in close proximity to the driving or a harmonic, will mean a shockwave will cause a strong response at that frequency, which may then be assumed to be broadband emissions from inertial cavitation (McDannold et al., 2006). To build a PCD to detect PSWs, however, PVdF material is deemed a better material choice (Chapter 7).

4.1.3 Different hydrophone types

Commercially available PVdF needle, membrane type or fibre-optic hydrophones (FOH), are predominantly used for free-field measurement of an ultrasound wave, and membranes and FOHs can be used to characterise the lithotripter-generated shockwave in ESWL. Multi-layer PVdF stack type hydrophones can be used for PCD or SONAR applications, fig. 4.4.

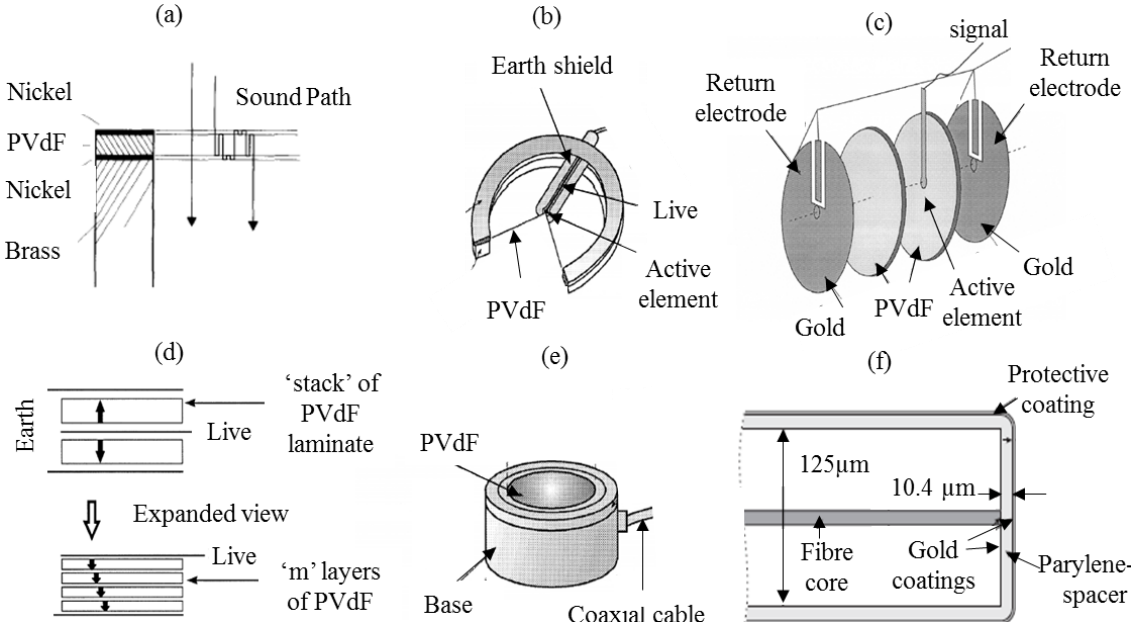

Figure 4.4. A variety of hydrophones used to calibrate a HIFU field, also variously as PCDs and measurement of an ESWL shockwave (a) Schematic of needle-type (Fay et al., 1994) (b) coplanar membrane (c) bilaminar membrane (Robinson et al., 2000) (d) Multilayer PVdF 'stack' (e) SONAR hydrophone (f) Fibre optic hydrophone tip (Morris et al., 2009).

A PVdF needle type hydrophone normally consists of an active area typically between 40 µm up to 4 mm, positioned at the tip of a brass needle casing, with nickel or gold electrodes and includes a backing material, fig. 4.4. (a) (Fay et al., 1994). During the 1980's, needles were used to resolve the lithotripter-generated shockwaves but were easily destroyed. This influenced a biopsy needle design with 'soft' backing material

(Schafer et al., 1990). The pros and cons of using a needle to detect low PPA PSWs will be discussed in §6.1.3

The membrane type consists of a thin film typically 100 mm in diameter stretched over a supporting hoop with no backing layer. A signal electrode (often gold) consists of a circle typically 0.5 mm or 1 mm in diameter, connected to a 0.2 mm track to the edge of the membrane. The signal electrode and the lead out track is surrounded by a broad hoop of gold, which is connected to the earth side of the circuit, hence the signal electrode is coplanar shielded and is known as a coplanar membrane, fig 4.4 (b). The coplanar type can only be used in deionised water, because both electrodes are exposed to the medium and this can leads to the degradation of the signal and interference when placed into a conductive medium (Harris et al., 2000). This problem was solved by laminating two layers of PVdF film together to create the bilaminar type, fig 4.4 (c). A disposable coplanar design was used to resolve the lithotripter-generated shockwave (Schafer et al., 1994) or the exposed electrode separated from the medium using an acoustically transparent polymer casing (Granz, 1989), or petroleum backing layer (Tavakkoli et al., 1996).

Free-field measurements of pressure amplitudes at the focus, or mapping of a HIFU field require a hydrophone with a small active area, to prevent spatial averaging. For acoustic scanning, the active area should be selected such that it is less than half the wavelength of the driving HIFU. The small active area and film thickness of the sound field hydrophones leads to low sensitivity, and they therefore require a wideband pre-amplifier to increase voltage output. A flat frequency response over a wide bandwidth, of 1 to 20 MHz for example, is required to accurately assess any non-linear harmonic

components in the HIFU field. These hydrophones can detect non-linear steep shock fronts but the bandwidth is limited by the film thickness or amplifier used (Robinson et al., 2000).

As PVdF film sensitivity is proportional to the film thickness (see §4.1.1.1), laminating a stack of PVdF film together can circumvent the need for a preamplifier, fig. 4.4. (d). Indeed, the Sonic Concepts PCD that features in Chapter 7, is an example of this design. Such devices are also used for low frequency SONAR devices, fig. 4.4 (e). The FOH uses an optical fibre to deliver light to an optical sensor at the end of the fibre fig. 4.4. (f), that detects changes in the refractive index of the medium caused by pressure fluctuations (Beard et al., 2000). The FOH can measure an ESWL shockwave (Staudenraus and Eisenmenger, 1993) but low sensitivity means it is unsuited to detecting the low PPA shockwaves (Kang 2014). The fibre is also fragile and the tip easily damaged. Moreover, the FOH has a relatively poor signal to noise ratio below 1 MHz.

4.2 Cavitation detection methods

4.2.1 Single element passive cavitation detection

A large variety of different PCDs are reported in literature; both PVdF and PZT PCDs are commonly used. If the PCD is focused then it is confocal and often coaxially aligned to the HIFU transducer axis to receive acoustic emission from the focal region. (Hockham et al., 2010, Zhou and Gao, 2013). Alternatively, the PCD can be positioned orthogonally (Hallow et al., 2006, Farny et al., 2010) or at some angle to the HIFU axis (Tung et al., 2010b). Many different design types are used as a PCD, such as a needle (Holt and Roy, 2001), focused (Hynynen, 1991) or weakly focused bowl (Prokop et al., 2007) or planar (Hoerig et al., 2014) devices, have been used to correlate enhanced

heating, thrombolysis and blood vessel occlusion bio-effects in HIFU, respectively. The diameter of the PCD active area is important regarding output voltage (see §4.1.1.1), but a large variety of different diameters are reported, often with no obvious rationale reported.

Commercial PCDs can be expensive and are normally manufactured to be sensitive over a particular frequency range or for a specific application. A range of commercial PCDs are available from companies such as Sonic Concepts (Wu et al., 2014), Panametrics (Farny et al., 2010), Olympus (Zhou and Gao, 2013) and the Cavimeter™ , from the National Physical Laboratory (NPL) (McLaughlan et al., 2006), which have been used to measure stable and inertial acoustic signatures in HIFU. The NPL Cavimeter™ , however was designed, and predominantly used, to detect high frequency emission from bubbles in ultrasonic cleaning systems (Felver et al., 2009), and both the Panametrics and Olympus are primarily used for non-destructive testing. The Sonic Concepts PCD (see §7.1.1) features a wide bandwidth 10 kHz to 15 MHz, this also allows the detection high frequency emissions much greater than f_0 (see §3.4.1).

Many in-house PCDs, such as a PVdF receiver element for use in a transcranial array for MRgFUS (OReilly and Hynynen, 2010), have also been reported. Leighton developed a planar PVdF PCD, with absorbing backing layer (Aptflex) and bio compatible matching layer, that was patented and successfully used in a clinical trials during ESWL (Leighton et al., 2008).

In some studies, the emphasis has been on detecting broadband emissions originating from inertial cavitation, thus the PCD was selected dependant on resonant frequency or for a bandwidth sensitive to frequencies higher than the driving (Hockham

et al., 2010, Farny et al., 2010). Alternatively, PCDs are selected such that the resonant frequency and bandwidth are most sensitive to the subharmonic frequency of the driving. (Husseini et al., 2005, McLaughlan et al., 2010, Schoellhammer et al., 2015, Tsai et al., 2016), under the assumption that the subharmonic signal is an acoustic wave.

4.2.2 Multi element cavitation detection

Active cavitation detection (ACD) refers to a transducer that transmits and receives a signal, backscattered from cavitation activity (Roy et al., 1990). A pulse-echo ultrasonic B-scan system was used to monitor bubbles activity in the hind leg of guinea pigs, exposed to a continuous-wave or pulsed-wave HIFU using 0.75 MHz driving frequency (Ter Harr et al., 1986), for example. The threshold for inertial cavitation to occur, and cause damage to rat lungs, was investigated using a 4 MHz diagnostic pulsed and color Doppler ultrasound system, used in combination with a 30 MHz ACD (Holland et al., 1996). Real time diagnostic ultrasound systems can be used for ACD but the radio frequencies (rf) from HIFU can interfere with the B-mode imaging, thus the HIFU treatment may have to be modulated to acquire an image (Vaezy et al., 2001). B-mode imaging has been used, in conjunction with a PCD, to identify the occurrence and location of inertial cavitation in mouse brain. The B-mode image was used to confirm the sensitivity of the PCD for detecting broadband emissions in BBB disruption (Tung et al., 2010b).

4.2.3 Multi element passive acoustic mapping

Although a PCD can detect an acoustic cavitation signal, a single element PCD cannot distinguish between individual bubbles in a cavitation cloud or multiple clouds contained within an ultrasound field. However, the use of a multi-element system, such

as a diagnostic array set to receive-only mode, can be used to identify cavitating regions (Gyöngy and Coussios, 2010b), in a technique known as passive acoustic mapping (PAM). The use of multi element arrays to act as a passive receiver can provide spatial and temporal resolution (Salgaonkar et al., 2009). PAM has been used for this purpose for a range of applications, such as monitoring HIFU treatment in *ex vivo* bovine tissue (Jensen et al., 2012), transcranial assessment and visualisation of acoustic cavitation (Arvanitis et al., 2015), and monitoring drug delivery (Choi et al., 2014).

In order to reconstruct the distribution of cavitation clouds, post beam forming of the acoustic data is necessary, which can be carried out in the time domain. Gyongy and Coussios produced an passive source power map from emissions from cavitating bubbles using a linear array (L10-5, Zonare Medical Systems, Mountain View CA) (Gyöngy and Coussios, 2010a), fig. 4.5.

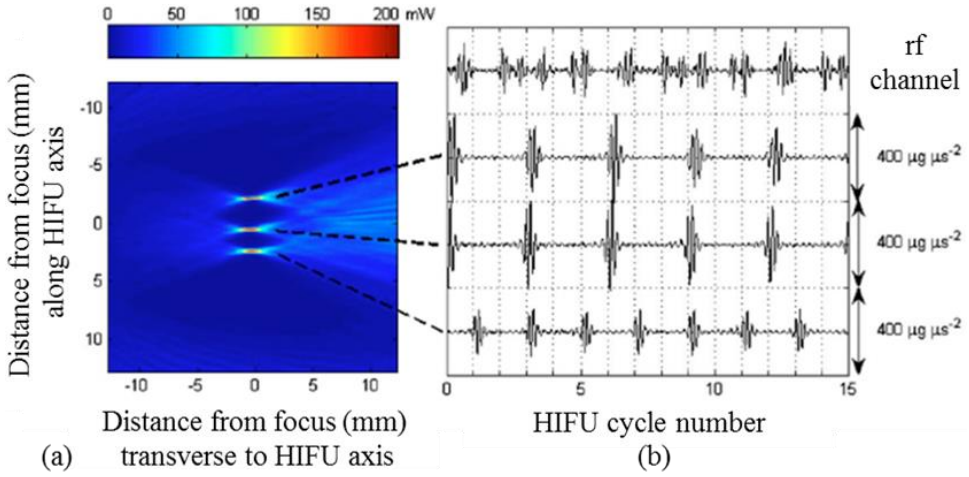

Figure 4.5. (a) Passive acoustic map (b) rf channel data (Gyöngy and Coussios, 2010a).

Fig. 4.5 (a) shows PAM reconstruction of three cavitation events during a 1.06 MHz HIFU exposure, from rf channel data depicted fig. 4.5 (b). The authors interpreted the top two bubble clusters as cavitating in phase on every third HIFU cycle and the distal cloud

does so every second cycle due to respective period tripling and doubling. The results from Chapter 5 offer an alternative explanation[3]; that PSWs are being emitted at $f_0/3$ for two clouds and at $f_0/2$ for the distal cloud. The waveforms within the rf data are reminiscent of the periodic decaying sine wave caused by the resonant ringing effect when a shockwave is incident to a high resonant frequency PZT element (see §4.1.1).

4.2.4 Alternative cavitation detection methods in HIFU

A number of studies exist that simultaneously detect sonoluminescence via a photon counter, and correlate the presence of free radicals using a spectrophotometer (Beckett and Hua, 2001). In a medium with chemical reagents such as Luminol present, the medium only luminesces when free radicals are produced. Sonochemiluminescence (SCL) has also been used, in combination with a high-speed camera, to map a 1.2 MHz HIFU field (Yin et al., 2014). Schlieren imaging and SCL can visualise bubble streaming in an ultrasonic bath (Nomura et al., 2005). Alternatively, a less common method measures the fluctuation in the drive power caused by acoustic backscattering from bubbles (Coakley, 1971). Significant fluctuations in the drive voltage were present only when boiling bubbles were detected, in a nonlinear HIFU field in tissue. It was noted that bubbles formed by boiling have a distinct large radius and strong acoustic spike in amplitude in the PCD data (Canney et al., 2010). McLaughlan combined several methods together to measure acoustic cavitation and boiling bubbles in *ex vivo* bovine liver simultaneously, fig 4.6.

---

[3] The author acknowledges Dr Jae Hee Song (The resident PAM expert) for the discussions that led to the alternative explanation presented for fig. 4.5 (b) rf channel data by Gyongy and Coussios.

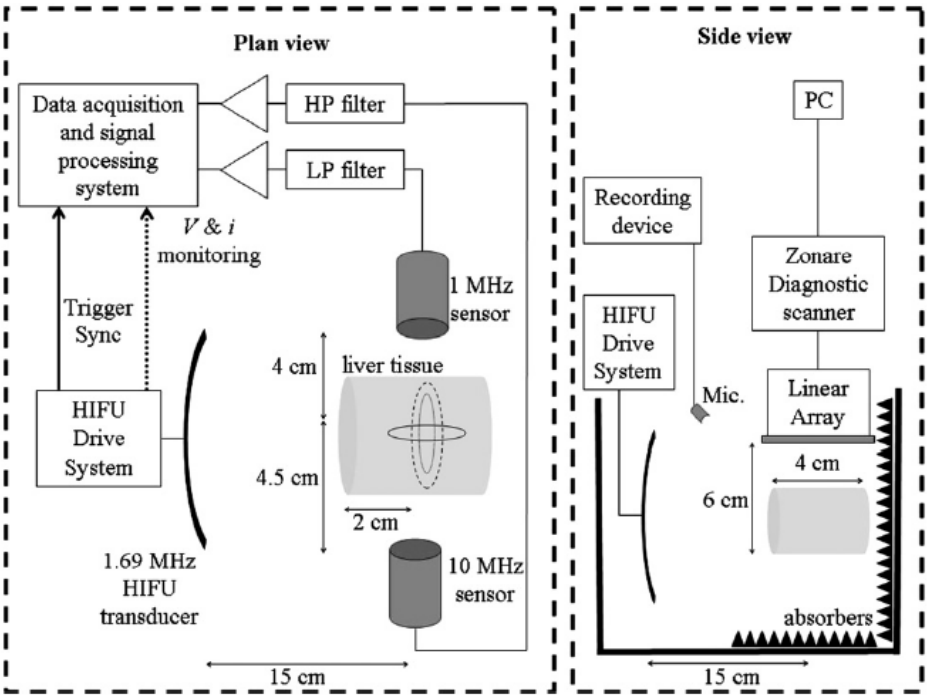

Figure 4.6. Experimental setup for detecting cavitation in *ex vivo* tissue. A suite of detection methods are combined, ACD using Zonare, PCD using two PCD, a microphone to record audible emissions and also power fluctuation in HIFU drive system were also measured. Taken from (McLaughlan et al., 2010).

The 'cavitation detection suite' incorporated both active and passive detection, measurements of power fluctuations, sonochemical reaction and including a microphone to record audible emissions (McLaughlan et al., 2010). Low frequency (10-30 kHz) audible emissions, were also reported from HIFU induced vessel rupture using PCD detection (Hoerig et al., 2014). Audible emissions have been correlated to sonochemical and luminescence indicators of inertial cavitation, in a aqueous solution (Birkin et al., 2003). A FOH was used to detect acoustic emissions in *ex vivo* bovine liver (Bull et al., 2013). A thorough review of cavitation detection methods for biological effects in HIFU is described by (Barnett, 1998).

4.2.5 Cavitation detection algorithms

Acoustic emissions collected by a PCD are normally post processed in the time domain, frequency domain or via time-frequency methods. Time domain analysis is based on the raw voltage signal to extract a value of interest, or post processing to reduce a fundamental or harmonic component by filtering. A frequency domain method uses a FFT to reveal the spectral components. The time-frequency analysis uses a short-time Fourier transform to visualise the emergence of a frequency component over time a 'spectrogram' was used to represent cavitation subharmonic emissions and to confirm BBB opening in mice(Tsai et al., 2016), fig 4.7.

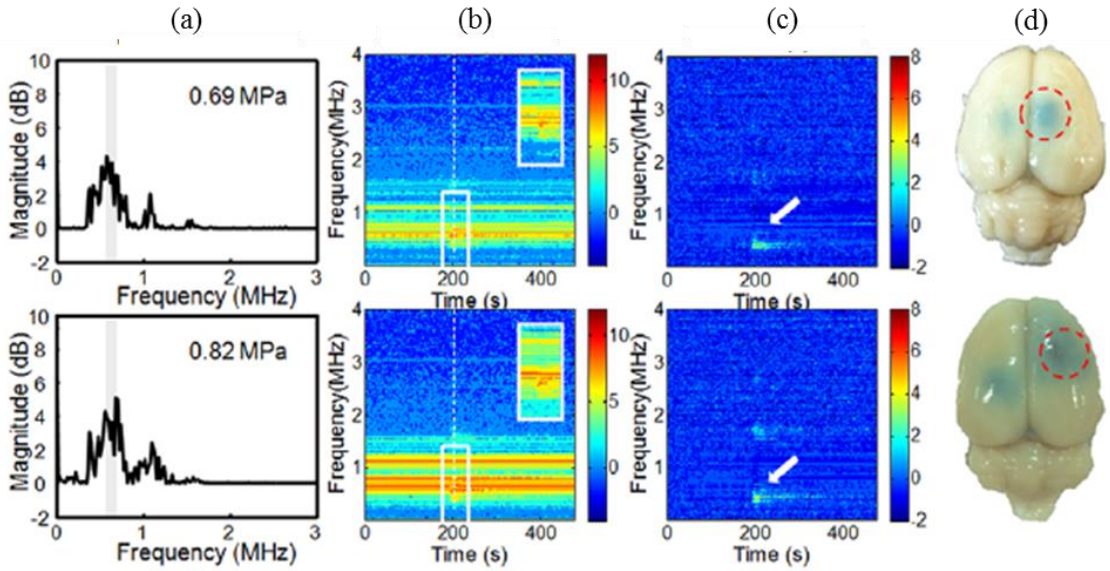

Figure 4.7. Representative acoustic emission analysis received by a PZT 0.55MHz transducer to confirm BBB opening in mice. (a) FFT spectrum (b) time frequency spectrogram (c) spectrogram difference (d) Mice brains stained with EB dyes to identify BBB opening locations. Taken from (Tsai et al., 2016).

Biomedical studies will often attempt to quantify the level or amount of cavitation that is occurring, using specific algorithms. The relationship between broadband emissions and inertial cavitation is often used to classify many bioeffects. A number of

researchers have chosen to use the ‘inertial cavitation dose’ (ICD) which is calculated by the root mean square of a frequency window between harmonic regions and integrating the area under the time trace. The ICD is associated with a broadband signal and was used as indicator for BBB disruption in mice (Tung et al., 2010a) primates (Wu et al., 2014), temperature elevation during lesion formation by HIFU (Zhou and Gao, 2013) and haemolysis (Chen et al., 2003).

PCD signal variance (V^2) over a broad frequency range 5-25 MHz was considered to be proportional to the power of acoustic emissions and was used to control temperature, by modulating the HIFU amplitude (Hockham et al., 2010). A similar variance method was used to measure broadband activity in adipose tissue at different HIFU frequencies (Kyriakou et al., 2011). A number of studies have chosen to use a ‘cavitation dose’ (CD) type measurement, where the total amount of cavitation signal received over time is measured. CD has been used to correlate haemolysis (Poliachik et al., 1999), platelet aggregation (Poliachik et al., 2004) cell viability (Hallow et al., 2006) and thrombolysis (Datta et al., 2008) bioeffects in HIFU, fig. 4.8. (next page)

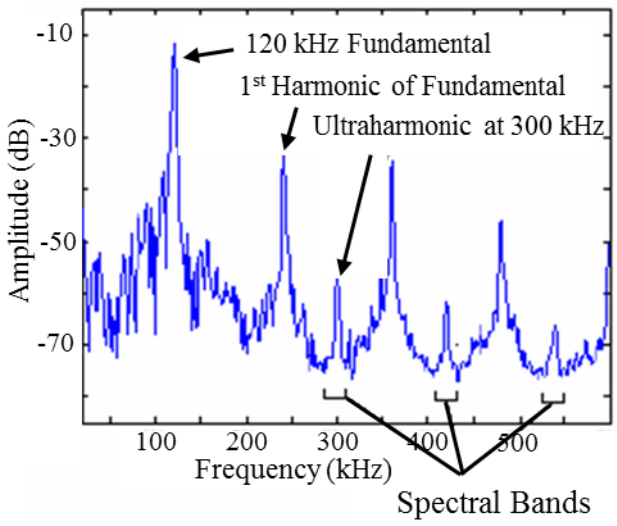

Figure 4.8. FFT detected using focused broadband Sonic Concepts PCD, illustrating the spectral bands that were used to calculate a cavitation dose measurement (Datta et al., 2008).

An algorithm similar to the variance method calculates the root mean square (RMS) over a wide frequency range higher than the driving, and is used to correlate a inertial cavitation threshold (Bull et al., 2013), shock induced heating in HIFU (Canney et al., 2010) and haemolysis (Everbach et al., 1997). Similarly a few algorithms exist to correlate the amount of stable cavitation occurring in relation to the subharmonic frequency, such as the relative subharmonic enhancement (RSE) for thrombolysis bioeffects (Prokop et al., 2007) or the cumulative harmonic index (CHI) to assess the subharmonic and damage to red blood cells using 0.75 MHz continuous wave ultrasound (Daniels et al., 1995).

This sub section demonstrates the vast array of different PCDs, detection frequencies and algorithms that are currently used to assess acoustic cavitation occurrence, and correlate bioeffects. Such a broad range makes it difficult for the cavitation community to undertake a meaningful comparative analysis, for consolidating results and planning experiments.

5 Periodic shockwaves: a mechanistic source of the subharmonic signal

Current understanding of acoustic cavitation, as an ultra-rapid and microscopic activity, has been limited by difficulties in predicting when and where the phenomenon will nucleate. Historically, the use of a pulsed laser has been fundamental to studying single, comparatively large vapour bubble dynamics, as the moment of pulse generation and point to which it is focused predetermines the bubble initiation. Previous research in the group developed a hybrid pulsed laser-high intensity focused ultrasound approach, termed laser-nucleated acoustic cavitation (LNAC), extending the benefit of the laser-induced cavity (LIC) techniques to the study of acoustic cavitation (Gerold, 2013).

The main hardware difference between that research and the work reported below, is that a second pulsed laser is incorporated to the set-up, providing illumination for the high-speed imaging. This laser pulses in synchronisation to the capture of each frame within a high-speed sequence, with the pulse duration thereby determining the effective exposure time, and temporal resolution. For the results below pulses of 20 ns (10 ns for chapters 6 and 7) were used, which confers a degree of shadowgraphic imaging, such that shockwaves and pressure fluctuations of the ultrasound become visible. This optical setup, combined with the pulsed laser for nucleation, has been fundamental to understanding the spatial and temporal dynamics of the cloud, and facilitated the comparison of passive cavitation detector (PCD) data, from the moment of nucleation. Imaging at rates around a million frames per second, relative to the several hundred of

kHz of the ultrasound driving frequencies (220, 254 kHz), means cloud behaviour is observed above Nyquist sampling rate, although bubbles are of course, inherently non-linear.

The experimental results presented in the following Chapters 5 to 7 were carried out using two different sonoptic chambers: V.1 and V.2. V.1 was used to make the first observations of periodic shockwaves (PSWs) and demonstrate their role in mediating the subharmonic signal. Ultimately, the constrained design of V.1 limited the placement of any sizable PCD without disturbing the HIFU field. An open-architecture V.2 was therefore developed, but this will be discussed in Chapter 6.

This chapter will give a description of the experimental setup, including the in-house fabricated transducer §5.1.1 and the sonoptic chamber version 1 (V.1), high-speed cameras §5.1.2 and the PCD used for initial experiments will be discussed in §5.1.3.

5.1 Material and Methods

5.1.1 In-house fabricated HIFU source

The HIFU transducer was constructed in-house from a 63.2 mm diameter bowl, that is spherically focused, thereby defining the focal distance, single element PZ 26 piezo ceramic (Meggit-Ferroperm, Kvistgard, Denmark) with an epoxy (Epofix) and K1 glass bead backing (3M^{TM}). The outer casing was made via rapid prototyping (uPrint SE, Stratasys, MN, USA), using acrylonitrile butadiene styrene (ABS) filament material and lacquered to make water proof. Impedance analysis (4395A, Agilent Technologies, CA, USA) revealed a fundamental resonance at f_0 = 254 kHz, and a lateral mode at 36 kHz. The device was driven with a sinusoidal signal from a waveform generator (DG4102, Rigol Technologies, Beijing, China) passed through an RF power amplifier (2100L, Electronics and Innovation, NY, USA). The acoustic pressure values reported[4] were calculated by scanning the HIFU field using a fibre optic hydrophone (FOH, Precision Acoustics), and then performing a spatial integration of the square of the acoustic pressure over the -6dB, which is proportional to intensity. This is equivalent to the power, measured by radiation force balance (RFB, Precision Acoustics, Dorchester, UK), divide by the -6 dB focal area. Thus, the acoustic pressure is a time and spatially averaged pressure amplitude (avPA) value over the -6 dB area.

[4] In Johnston *et al*, Ultrasonics (2014) the HIFU pressure amplitude values were reported as peak-peak. Under the principle of the Radiation Force Balance technique for calibration, this should be an averaged pressure amplitude. We informed the editor at the time of realising the mistake, who decided that no further action was required. It is further noted that Johnston *et al*, Ultrasonics (2014) achieved a maximum position of 5th most downloaded paper from Ultrasonics.

5.1.2 Sonoptic chamber Version 1 and high-speed imaging

A 'sonoptic' chamber[5] V.1 was designed using SolidWorks and constructed via rapid prototyping, to conduct cavitation studies in the focused ultrasound field generated by the in-house fabricated transducer previously described in §5.1.1. A distinctive 'square hour-glass' architecture, accommodates the field of the transducer which was fixed horizontally on the base (150 × 150 mm^2), to generate HIFU that propagates upwards through the chamber, without reflection or scatter, fig. 5.1.

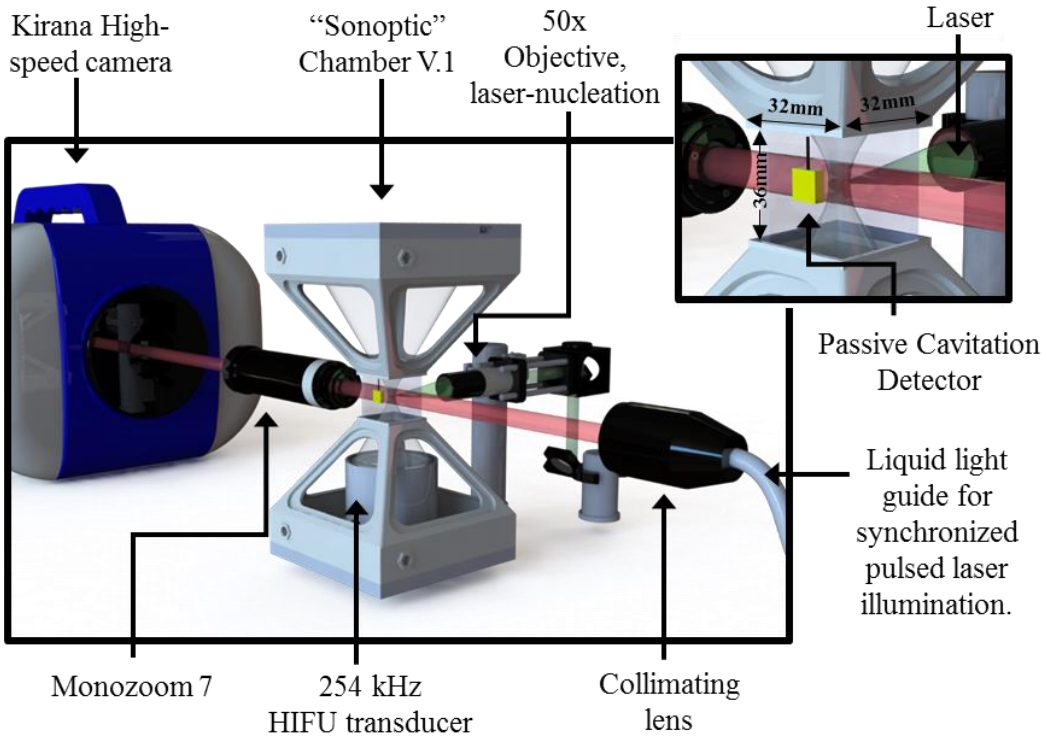

Figure 5.1. Sonoptic chamber V.1 experimental setup. Including high-speed camera, imaging optics and pulsed laser (red) for illumination. Inset top right is the position of the PCD and the pulsed laser (green) used for laser nucleated acoustic cavitation (LNAC).

[5] Sonoptic chamber V.1 is originally designed to be used for dual frequency cavitation control, using dual diametrical opposing transducers; a result from this experiment is discussed in Appendix A.

This was confirmed via comparison of field maps generated with a FOH through the focal zone and axially in both the sonoptic chamber and a free-field scanning tank (1 × 1 × 1 m^3) configuration, fig. 5.2.

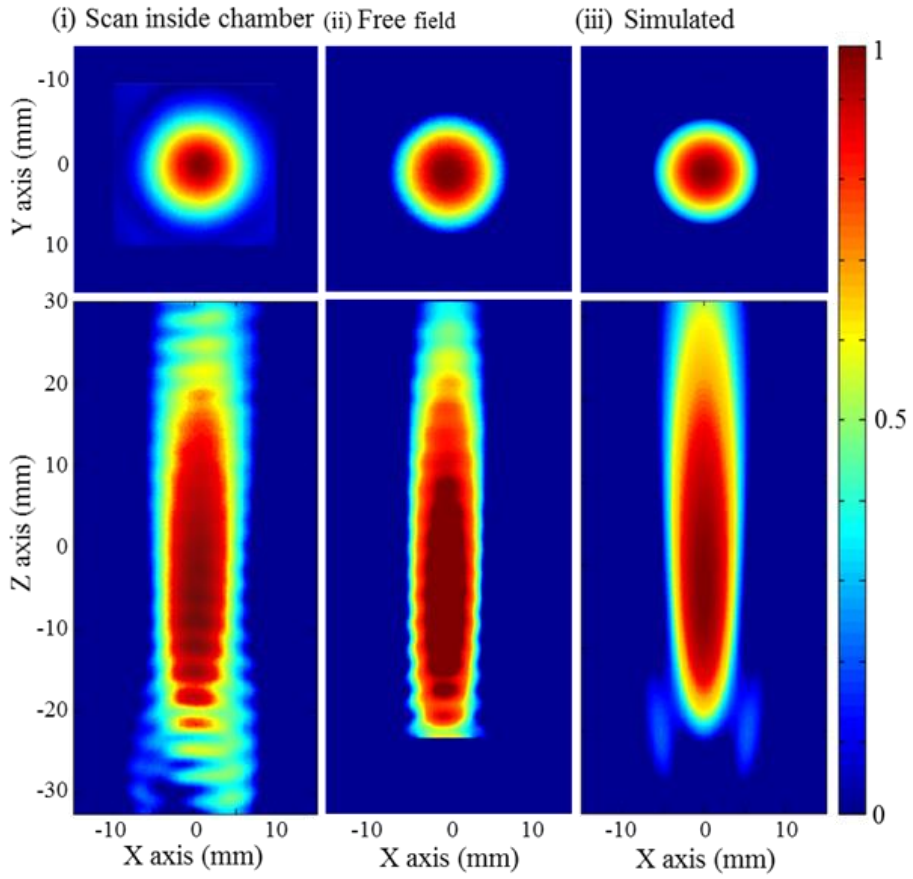

Figure 5.2. Sonoptic chamber V.1 field mapping carried out via fibre optic hydrophone, and simulation of HIFU field using field II simulator. The measured -6 dB focal width 8.2 mm and focal length 48.3mm in the axial direction.

The focal region of the HIFU field was contained within glass walls (32 × 32 × 36 mm^3) that formed the neck of the sonoptic chamber. This facilitated good optical access to that region of the field for observation. Imaging was undertaken through a Monozoom 7 lens system (Bausch & Lomb, Rochester, NY, USA) set to 3.5× magnification, with a Kirana-05M high-speed camera (Specialised Imaging, Tring) recording 180 frames of

(924 x 768 pixels) at 1 million frames per second (Mfps). Illumination was delivered via synchronous 20 ns laser pulses (CAVILUX smart, Cavitar Ltd., Finland) using a liquid light guide and a collimating lens. The spatial resolution was experimentally determined as 12.3 ± 0.2 μmpixel^{-1}, via the *in-situ* imaging of 400 μm polymer microspheres (standard deviation 1%, Duke Standards, Fisher Scientific, Loughborough, UK).

Acoustic cavitation was nucleated via a 6 – 8 ns 532 nm laser pulse (Nano S 130-10 frequency-doubled Q-switched Nd:YAG, Litron Lasers, Rugby, UK) of energy 0.9 ± 0.1 mJ respectively (instrument error, according to manufacturer), passed through a long working distance objective lens (50x 0.42 NA Mitutoyo, Kawasaki, Japan, 6mm back aperture diameter), incident to the focal region of a pre-established HIFU field (Gerold et al., 2011). The visible wavelength (532 nm = green) facilitates easily alignment of the optical setup. The laser pulse energy was below the optical breakdown threshold for the host medium of de-ionised water, de-gassed via boiling and cooling in a sealed vessel, to an O_2 content below 4 mgL^{-1}

The Kirana-05M software provided an electronic trigger to a signal delay generator (DG535, Stanford Research Systems, USA) which in turn sent coordinated trigger pulses to the nucleation laser, at t = 180 μs, determined by the Q-switch delay, oscilloscope, illumination laser and waveform generator, which sent a 54-cycle burst sinusoidal waveform at 254 kHz for power amplification. A 100 μs delay was applied to allow the transducer to ring up to the required pressure amplitude and for the ultrasound to reach the focus, generating ~ 20 μs pre-established HIFU field. The HSC operation was triggered to capture 5 frames (5 μs) prior to nucleation, such that cloud development was observed from inception, and to ensure no pre-existing cavitation activity had occurred.

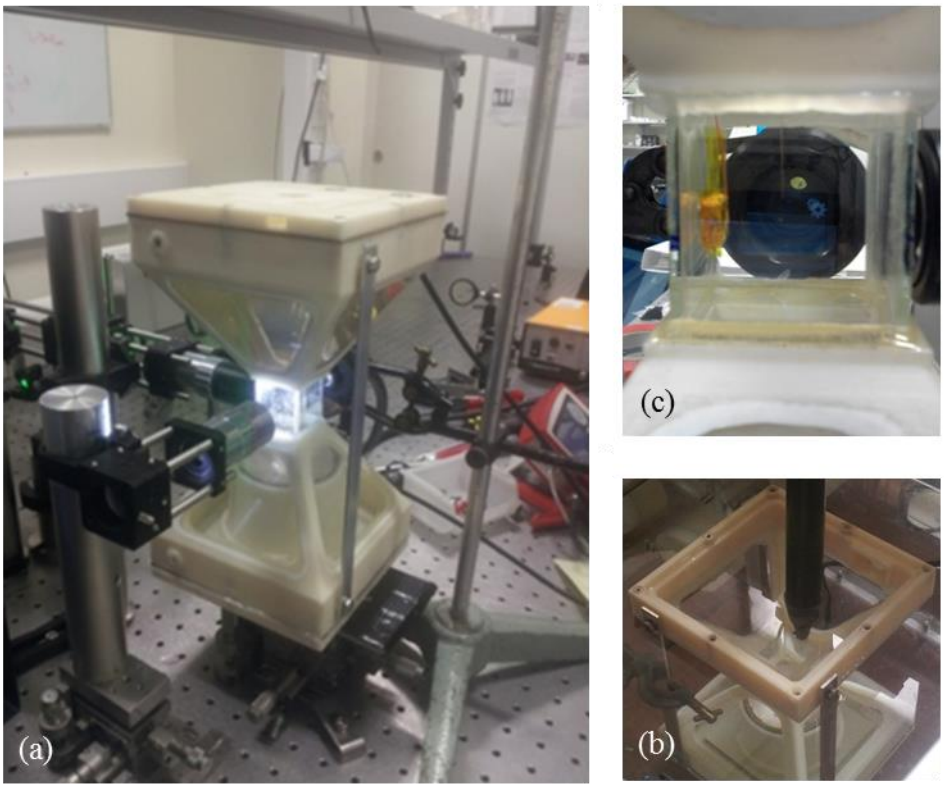

Figure 5.3. Photographs of the sonoptic chamber V.1. (a) V.1 was positioned onto a xyz translational stage for micro positioning of the field relative to the laser nucleation optics (back left). Also visible is the imaging optics, in this photo a long working distance Mitutoyo 10x objective (but all presented results were undertaking using a Monozoom 7) also mounted on an xyz translational stage for adjustment of the imaging focus. (b) Fibre-optic scanning of the HIFU field inside chamber V.1, to confirm the field is not disturbed by chamber design. (c) Position of the PCD used for experimental results, onto the middle of the glass walls with both the nucleation and imaging objective visible.

5.1.3 Passive cavitation detector

The PCD used for acoustic emission detection (sourced externally, from InSightec Ltd.), was constructed from piezo-ceramic composite of dimensions $6 \times 6 \times 2$ mm^3. The active element was diced to form nine distinct pillars, each ~1.5 mm^2, thereby reducing lateral mode vibrations. Silver epoxy provided the acoustic matching and acted as an electrode to the element. The device was wrapped with copper tape to provide ground and shielding, particularly from the Q-switch of the nucleating pulsed laser. A second

electrode was provided via a micro-coaxial cable soldered to the element, which was isolated from the shielding, fig. 5.4 (a, b).

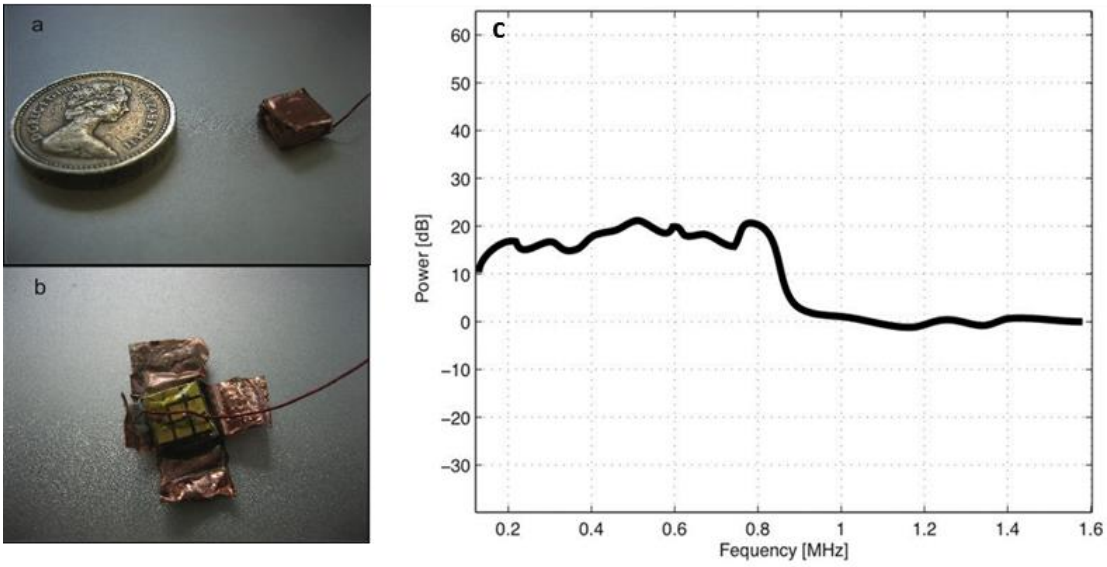

Figure 5.4. Passive cavitation detector. (a) This PCD was used to detect acoustic emissions from LNAC, in sonoptic chamber V.1. (b) The copper tape is peeled back to reveal the kerfed PZT structure (c) Sensitivity characteristic of the PCD in the frequency domain (Gerold et al., 2013).

The sensitivity of the device was previously assessed (Gerold et al., 2013) , via the recording of an established cavitation field, driven at very high power by a 1.17 MHz HIFU transducer (ExAblate 2000, InSightec Ltd.), under the assumption of 'broadband noise from inertial activity[6]'. The approach indicated a flat sensitivity centred around 500 kHz, over a bandwidth of ± 350 kHz, to -6dB. During an experiment, the PCD was mounted on the inside of one of the glass walls, which contained the HIFU focus, within the sonoptic chamber. In this position, the front face of the detector was 10 – 11 mm from

[6] The research presented in this thesis questions the validity of this assumption, and highlights the need for a PCD, for which the detection method is fully understood.

the nucleation-laser focus, where cavitation activity was generated. Acoustic data was collected via an oscilloscope (MS07104A, Agilent Technologies), 12-bit vertical resolution, sampling at a rate of 4 GSs^{-1} and transferred to a PC for subsequent analysis in MATLAB.

5.2 Results

5.2.1 High-speed camera observations

A series of preliminary experiments were initially undertaken, across the range of avPA available with the HIFU configuration described, at 0.1 V signal amplitude increments, limited by the maximum permissible input to the power amplifier of 1.0 V. This served to identify the avPA values, reported below, that generated temporally stable periodic shockwave formation from the acoustically driven clouds. At least six data sets (high-speed observation of single cavitation cloud nucleation and development, and parallel acoustic detection with the PCD) were used for analysis purposes, and the shockwave periodicity results are reported as average value ± standard deviation.

Fig. 5.5. (next page) depicts sample high-speed images, extracted from sequences recorded at 1 Mfps of cavitation clouds evolving under HIFU of avPA (a) 0.48 ± 0.08 MPa, (b) 0.64 ± 0.12 MPa, (c) 0.92 ± 0.17 MPa and (d) 1.22 ± 0.22 MPa.

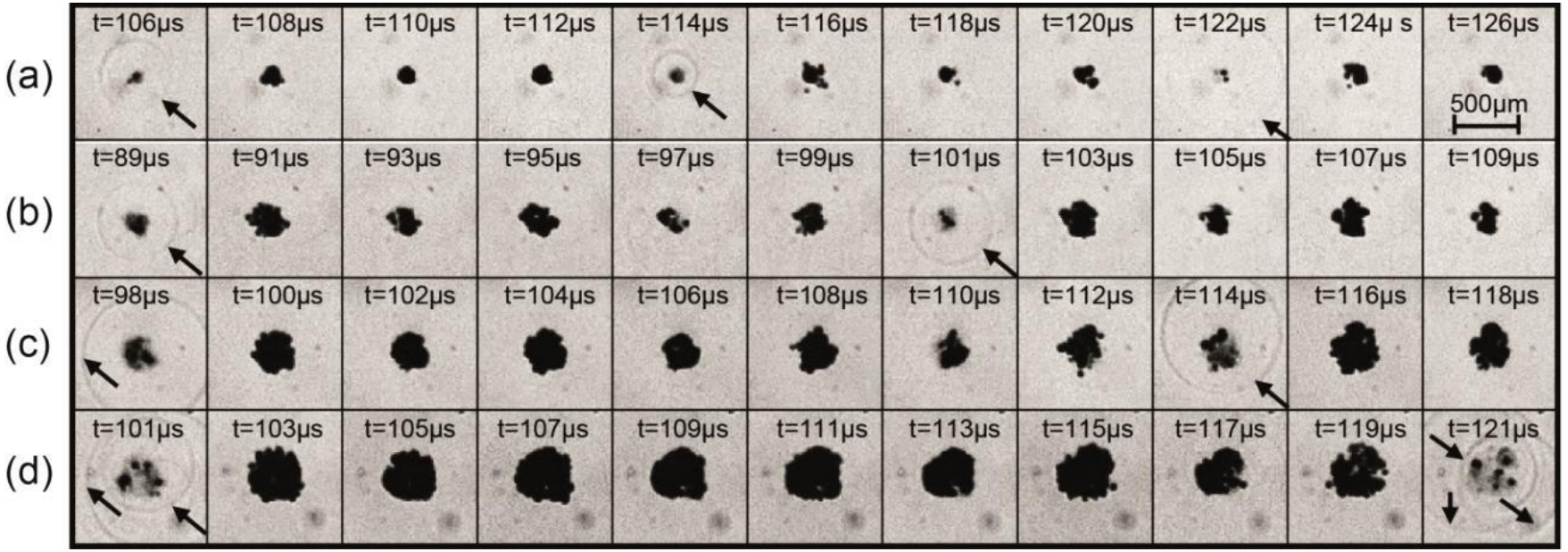

Figure 5.5. Representative high-speed images extracted from sequences recorded at 1 Mfps, of cavitation cloud development under HIFU exposures. avPA (a) 0.48 MPa, (b) 0.64 MPa, (c) 0.92 MPa, and (d) 1.22 MPa. Increasing the insonation pressure increased the size of the cloud that develops, and the period of recurring shockwave emission (arrowed black throughout), coincident to strong cloud collapse. Scale bar top-right.

Larger clouds developed at higher intensities, due to more energetically driven fragmentation events spawning an increased number of daughter bubbles (Postema et al., 2004b). Clouds were observed to undergo collective oscillatory behaviour as has been previously reported (Gerold et al., 2013, Lu et al., 2013). Periods of inflation, during which the cloud oscillated through a series of partial contractions, are interspersed with strong collapses, from which the cloud re-inflated to enter the next oscillation stage. This repeated behaviour will be referred to as being comprised of repeated growth, oscillation and collapse (GOC) cycles.

The shadowgraphic imaging facilitated the observation of periodic shockwave generation, coincident with the cloud collapse of each GOC cycle, arrowed at t = 106, 114 and 122 μs in fig 5.5 (a). The images of fig. 5.5 (c-d) were selected for equivalent collapse, and shock-emission (also arrowed), from clouds driven by higher HIFU avPA, at similar stages of cloud development, circa 100 μs following nucleation. The shockwaves arrowed at Fig. 5.5 (b) 101 μs, (c) 114 μs and (d) 121 μs were the first observed from each of the clouds subsequent to those emitted at (b) 89 μs, (c), 98 μs and (d) 101 μs. The time interval between the shock-emissions is representative of the shock-period throughout the image sequence acquired, at each avPA investigated.

These observations, recorded at 1 Mfps, only permitted an average value of ~1500 ms^{-1} to be estimated for the shockwave propagation, consistent with the speed of sound in water at room temperature. This value of propagation speed was used to infer the moment of shock-detection at the PCD, the correlation to the acoustic data, section §5.6.

A 7.9 ± 0.5 μs (average value over n ≥ 6 data sets ± standard deviation) period of shockwave emission from single clouds driven by avPA = 0.48 MPa, represented fig. 5.5 (a), corresponds to an emission frequency, f_{sw} = 127 ± 8 kHz ≈ $f_0/2$, half-harmonic to the driving frequency of the HIFU insonation. At 0.64 MPa, the cloud of fig. 5.5 (b) underwent two partial contractions, captured at t = 93 and 97 μs, during the oscillation phase of the GOC cycle, with strong collapse and coincident shockwave emission not observed until 101 μs. An 11.8 ± 0.3 μs shockwave period at this driving amplitude corresponds to f_{sw} = 84.6 ± 1.7 kHz ≈ $f_0/3$, the first higher-order subharmonic. Increasing the avPA of the primary insonation further, increased the period of the shockwave emission, such that f_{sw} = 63.3 ± 1.3 kHz ≈ $f_0/4$ and 50.5 ± 0.5 kHz ≈ $f_0/5$, at 0.92 and 1.22 MPa respectively.

5.3 Extraction of the acoustic subharmonic signal

The raw acoustic data collected by the PCD, from the clouds at each HIFU avPA represented in fig. 5.5, truncated to the duration of cloud observation are shown in fig. 5.6 (a, c, e and g), along with the corresponding power spectra from 0 – 600 kHz, fig. 5.6 (b, d, f and h), obtained via FFT.

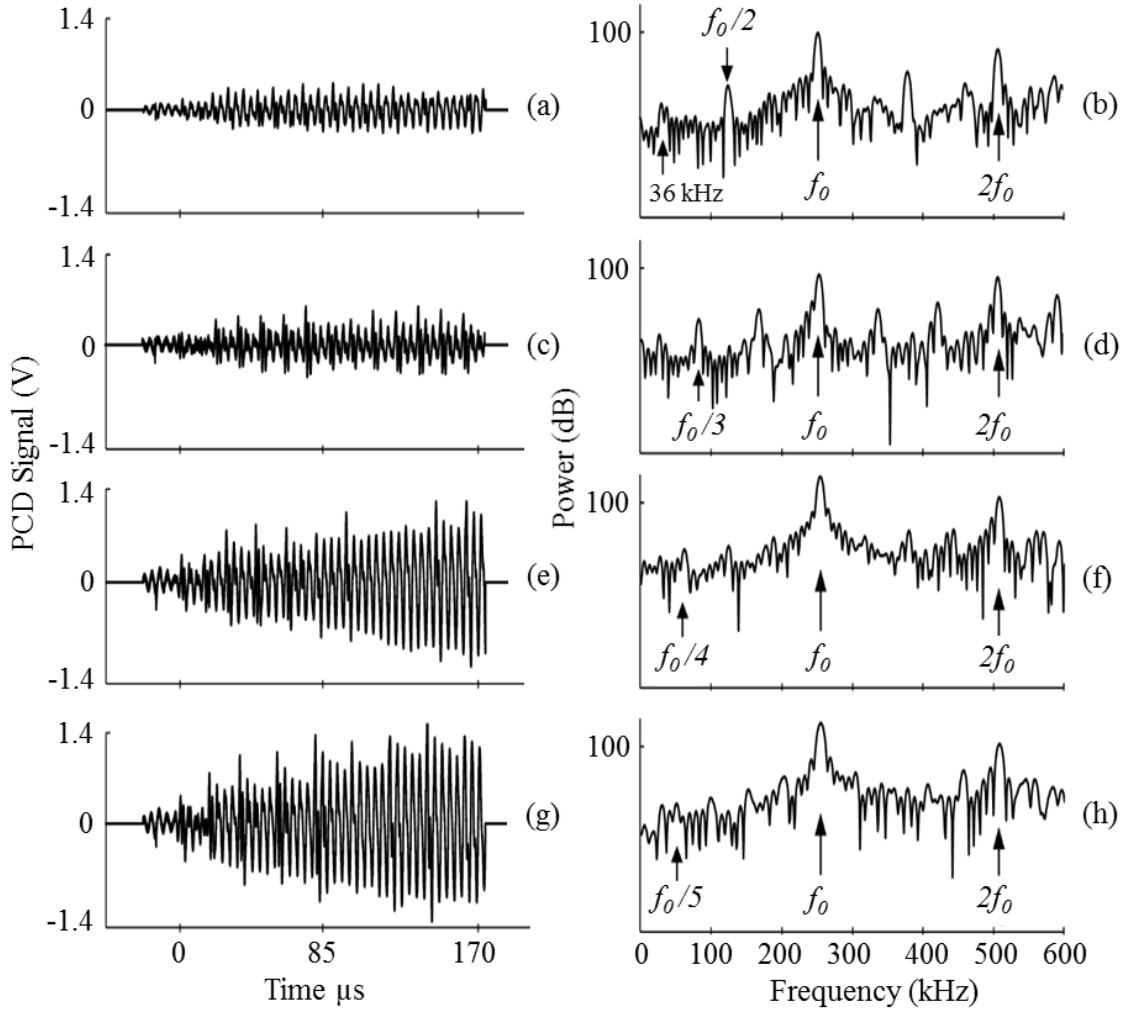

Figure 5.6. (a, c, e and g) The raw acoustic signals collected by the PCD, from each of the clouds of fig. 5.5, and the corresponding power spectra (b, d, f and h). The spectra are dominated by the fundamental driving at 254 kHz, and its 2nd harmonic. Also apparent are the subharmonics nf_0/m, depending on the avPA of the driving, as well as ultra-subharmonics between f_0 and $2f_0$. The lateral mode of the transducer at 36 kHz, common to all the spectra, is noted in (b).

The fundamental driving is arrowed throughout, and the lateral mode of the HIFU transducer noted in fig. 5.6 (b). From all spectra collected to the data set, 126.7 ± 1.2 kHz (average value from n ≥ 6 ± standard deviation), corresponds to the $f_0/2$ subharmonic for avPA = 0.48 MPa. At the higher avPA, spectral features at 83.8 ± 1.8, 62.8 ± 1.0 and 52.0 ± 1.6 kHz represent the higher-order subharmonics at $f_0/3$, $f_0/4$ and $f_0/5$, at driving

amplitudes of 0.64, 0.92 and 1.22 MPa, respectively. The ultra-subharmonics at frequencies > f_0 were also apparent, fig. 5.6.

In order to identify the specific acoustic signal responsible for the subharmonic features of the power spectra, the raw signals were subjected to a filtering protocol in MATLAB. This process is illustrated by fig. 5.7. (next page), using the acoustic emissions from the cloud driven at avPA = 0.92 MPa, fig. 5.6 (e). Applying a 4^{th} order low-pass Butterworth filter at 220 kHz produced the trace depicted in fig. 5.7 (a), which removed all signal > f_0, but left a significant component of the fundamental, and the subharmonics, fig. 5.7 (b). Further filtering with a high-pass 4^{th} order Butterworth at 48 kHz, removed the lateral mode, and a second low-pass filter at 150 kHz removed sufficient fundamental to reveal the signal responsible for subharmonic peaks, fig. 5.7 (c and d), as well as residual fundamental. Finally, to verify that the filtering procedure described delivered the signal responsible for the subharmonic, fig. 5.7 (c) was subtracted from (a), to produce (e). The FFT of that signal, fig. 5.7. (f), is effectively monochromatic at the fundamental, and thereby confirmed that the subharmonics had been removed. Similar treatment for the PCD data collected from the clouds at the other HIFU avPA, equivalently identified the acoustic data responsible for the respective subharmonics of fig. 5.6. (a, c and g).

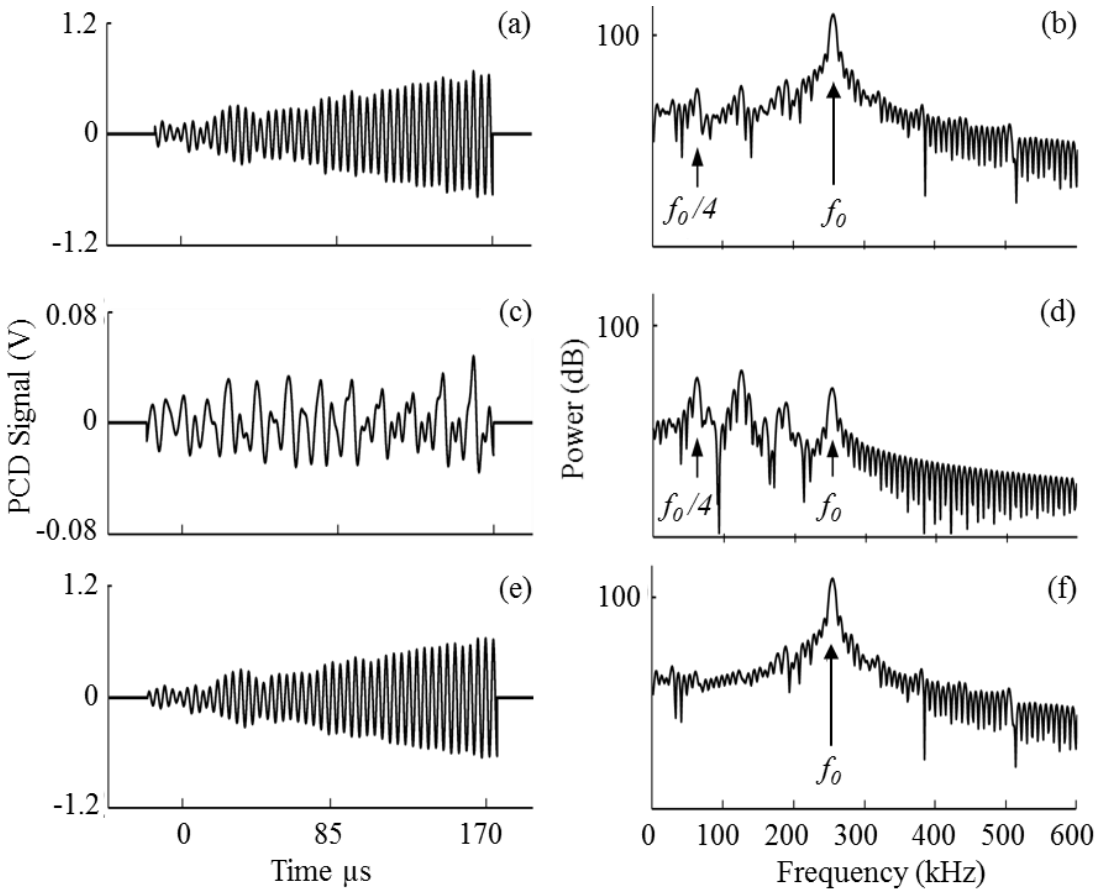

Figure 5.7. Voltage-time waveform of raw signal, filtered and subtracted and corresponding FFT. (a) The acoustic data of fig. 5.6 (e), filtered at 220 kHz. (b) The power spectrum of (a) reveals reduced fundamental and the $f_0/4$ subharmonic (arrowed) and higher order multiples of $f_0/4$. (c) The application of a second filter at 150 kHz, removes most of the fundamental, exposing the signal responsible for the subharmonics, which are now prominent in the spectrum, (d). Subtraction of signal (c) from signal (a) yields (e), the spectrum for which, (f), demonstrates the removal of the subharmonic peaks.

5.4 Comparison of high-speed images and acoustic data

For direct comparison of the filtered acoustic data to the observed cloud dynamics at each avPA, a dark-pixel counting algorithm was implemented to each of the high-speed image sequences, represented in fig. 5.5. The algorithm sums the dark-pixel number from each image sequentially, and outputs the variation with time over the observation duration, which can be taken to represent the cloud dynamics for a given experiment, fig.

5.8 (grey dash lines). Through this approach, it is evident that the clouds take 20 - 30 µs to become established and enter stable periodic GOC cycle behaviour. Progressively longer GOC periods, for the larger clouds at higher intensities, are also evident through this representation.

The specific cloud collapses that produced the shockwaves highlighted in fig. 5.5 are similarly arrowed in fig. 5.8, along with the corresponding features within the filtered acoustic data. For convenience, the PCD time trace is shifted by -7 µs to compensate for the shock-propagation time to the detector surface.

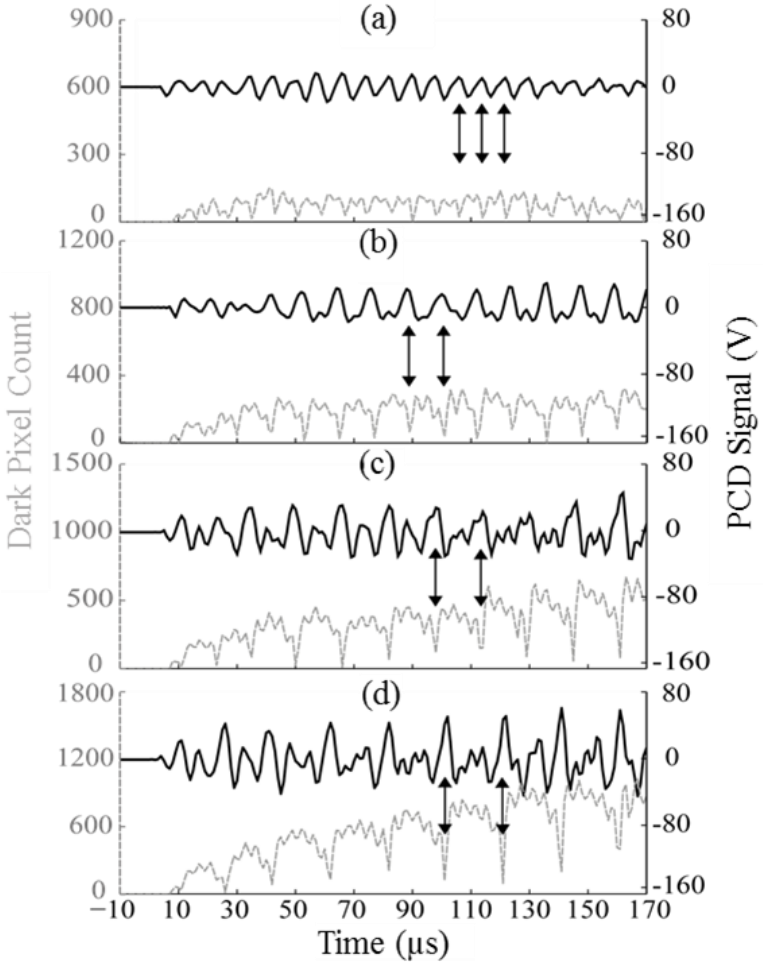

Figure 5.8. (a-d) Filtered PCD data (solid) of the acoustic emissions recorded from the clouds depicted in fig. 5.5. (a-d, respectively). (Figure caption on next page).Each

trace is shifted by -7 μs to account for shockwave propagation time to the detector. The dark-pixel count (grey dashed) for the entire image sequence correlates, p (two-tailed) < 0.01 (r = 0.996), over all data, acoustic features to the strong and periodic cloud collapses coincident with shock-emission (Note different dark-pixel scales selected for ease of viewing).

The number of collapses and shockwaves imaged via high-speed photography match the number of shockwaves detected by the PCD, for each HIFU avPA investigated. It is clear that the local minima of the dark-pixel curves, indicating the cloud collapse at the end of a GOC cycle, coincide with the peaks of the filtered PCD traces.

5.5 Summation of statistical analysis

High-speed imaging observations were compared to the filtered acoustic emissions collected by the PCD, via a two-tailed Pearson product-moment correlation coefficient, to determine the significance of the correlation of shockwave detection through each modality, for each experiment. A two-tailed test was chosen to assess for the possibility of a positive and negative correlation relationship. A p-value < 0.01 was taken as highly significant[7], and < 0.05 as significant. Statistical analysis indicated that for $f_0/2$, there was a highly significant positive correlation between the shocks observed via high-speed photography and those detected by the PCD (p(two tailed) < 0.01) , (r = 0.729, n = 17). Analysis of $f_0/3$, $f_0/4$ and $f_0/5$ data showed significant positive correlations between the two modalities (p(two tailed) < 0.05 for all three cases), (r = 0.790, n = 8) and (r = 0.816, n = 8) and (r = 0.887, n = 5), respectively.

5.6 Multiple front shock-emission from larger clouds

[7] The author acknowledges Dr Ceclia Tapia for her assistance in carrying out the statistical analysis for the data presented in §5.5.

In contrast to the smaller clouds at lower HIFU avPA, which collapsed to give well defined, radially symmetric single-front periodic shockwaves, fig. 5.5 (a, b), the larger clouds at higher pressure amplitude emit multiple shock-fronts during collapse, fig. 5.5 (d) at t = 101 and 121 µs. This observation suggests that, for larger clouds in this experimental configuration, collapses occurred within spatially separated sub-clusters, which each independently emitted a single shock-front. Assuming radial propagation for each front, the origin of the shockwave may be pinpointed, simply as the centre of the circle described by the component front. Moreover, the collapse time of the sub-cluster can be precisely resolved, if the propagation speed is well characterised. An illustrative example of this latter point is provided in fig. 5.9, which depict three sequential frames extracted from the sequence at avPA = 1.22 MPa, 41 µs after laser-nucleation (and later represented by fig. 5.5 (d)).

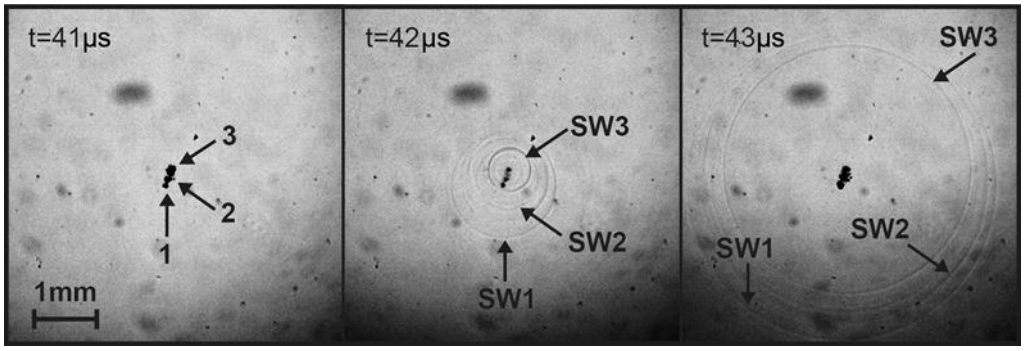

Figure 5.9. Earlier frames from the high-speed sequence recorded at HIFU avPA = 1.22 MPa. At 42 µs, three shockwaves (SW1-3) have emerged, each centred on a sub-cluster (1-3, at 41 µs). The distance propagated by each shock, relative to the others at any given instant, is indicative of the temporal order of collapse for the source sub-clusters. Scale bar bottom-left.

The dark shadow encroaching from the bottom of these images was the ensuing negative-pressure phase of the incident HIFU, visualised through the shadowgraphy described previously and apparent for this field of view. The extended focal region of the

HIFU field, led to poor optical focusing of the driving pressure fluctuations, however a propagation speed of ~1500 ms^{-1} is evident.

At this stage of the cloud development, a relatively simple structure of three distinct sub-clusters existed (labelled 1, 2 and 3). The image rate of 1 Mfps was insufficient to resolve the temporal order of collapse of the closely spaced sub-clusters. However, by 42 μs, shockwaves labelled SW1, SW2 and SW3, centred on sub-cluster 1, 2 and 3 respectively, were apparent. Assuming equivalent average propagation speeds for each shock, indicates that sub-cluster 1 collapsed first, followed by 2 approximately 110 ns later, with sub-cluster 3 collapsing last, some 80 ns after that. As such, dynamics that occurred on timescales much shorter than the imaging rate can be inferred.

In the context of PCD detection of the acoustic subharmonic from single cavitation clouds, the multiple front shockwaves will have had little bearing, as the time over which the multiple fronts of the shockwaves were spread (100's ns) was much smaller than the time between shock emission (10's μs), fig. 5.5 and 5.9. However, this time-period could have an influence on the broadband emission that are reported in literature, and will be discussed briefly in Chapter 8 Future work.

5.7 High-speed camera observation of switching clouds

Section 5.4 demonstrated that clouds underwent stable GOC cycles with the time between collapse ≈ 8, 12, 16 and 20 μs, respectively, at specific avPA values of 0.48, 0.64, 0.92 and 1.22 MPa. The shockwaves emitted at the moments of collapse are also of a stable period, and constitute the subharmonic signal, of order $f_0/2$, $f_0/3$, $f_0/4$ and $f_0/5$.

At avPA 0.52, 0.76, 1.04 MPa values intermediate to those that generate stable GOC cycles the clouds collapse with GOC cycles between the values associated with the stable avPA values above and below that intermediate value. For example, the cloud of fig. 5.10 (i) at 0.52 MPa exhibits concerted collapses at 25, 37 and 49 μs, and therefore GOC ≈ 12 μs associated with $f_0/3$ at 0.64 MPa, followed by a collapse at 57 and 65 μs, for which GOC ≈ 8 μs, associated with $f_0/2$ at 0.48 MPa. The switching time period is also demonstrated in the corresponding dark-pixel count, fig. 5.10 (ii) where the concerted collapse from fig. 5.10 (i) are arrowed.

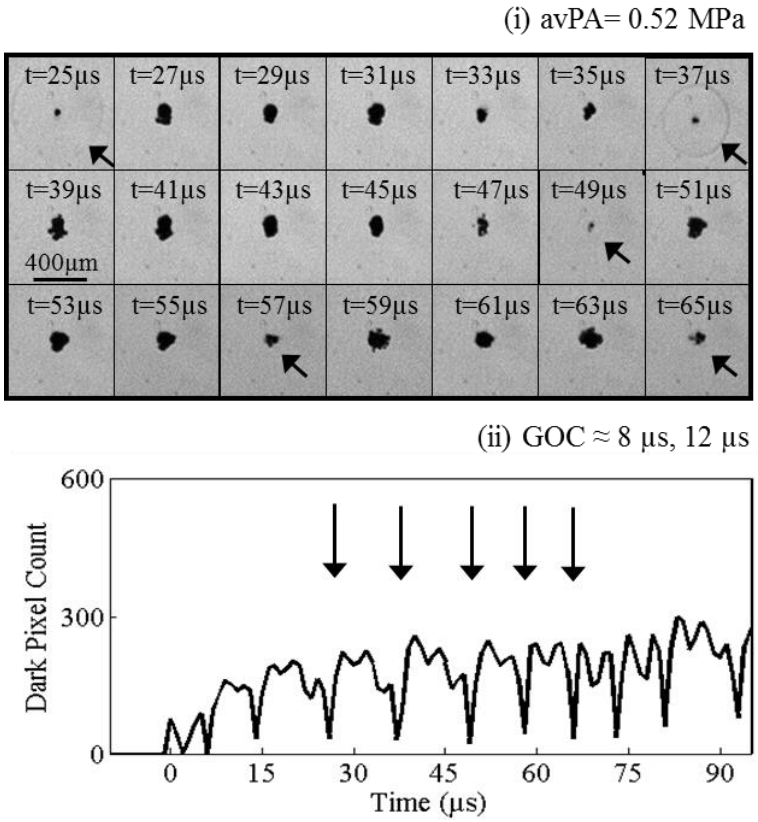

Figure 5.10. (i) High-speed image sequences illustrating cloud oscillation dynamics of switching cloud oscillation periods, 8 and 12 μs and cloud collapse (arrowed) (ii) dark-pixel counting algorithm and corresponding minimum (arrowed) from the image sequence arrowed in (i). Specifically GOC ≈ 8 and 12 μs ($f_0/2$ and $f_0/3$) at 0.52 MPa.

Cloud collapses at intermediate avPA are often not as pronounced as those at stable values of avPA, and do not always result in a clearly defined shockwave, or multi-fronted shockwaves. Fig. 5.11. (i) shows a cloud collapse at 34 and 46 µs, GOC ≈ 12 µs with a shockwave visible (arrowed) at 34 µs but no shockwave visible at 46 µs. This is followed by a collapses at 62 µs, GOC ≈ 16 µs, a shockwave is visible before a switching and collapsing at 74 µs, GOC ≈ 12 µs and no shockwave is visible.

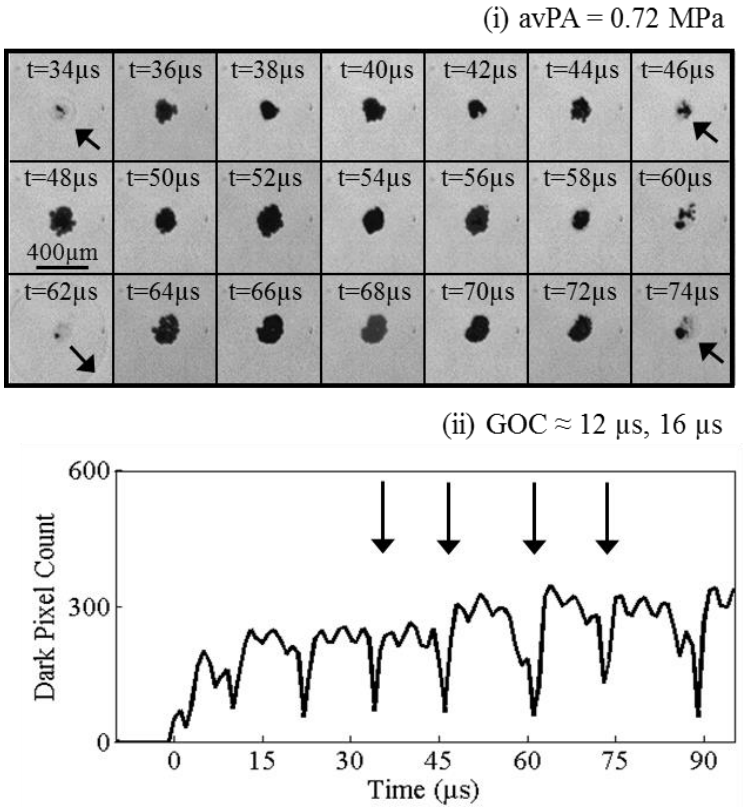

Figure 5.11. (i) High-speed image sequences illustrating cloud oscillation dynamics of switching cloud oscillation periods, 12 and 16 µs and (ii) dark-pixel counting algorithm Specifically GOC ≈ 12 and 16 µs ($f_0/3$ and $f_0/4$) at 0.72 MPa.

In-between the concerted collapses (arrowed black throughout), the clouds of all avPA undergo a series of partial inflation and deflations, at a frequency matching that of the fundamental HIFU driving (f_0 = 254 kHz), with a period of ≈ 4 µs. For example fig. 5.12 (i) the cloud collapsed at t = 38 µs, inflates at 40 µs and deflates at 42 µs, with the

period of inflation at 40, 44 and 48 and deflations at , 42 , 46 and 50 µs before collapse at 54 µs. In this example at 1.04 MPa, the cloud collapsed at 18, 38 and 54 µs, corresponding to a fundamental oscillation frequency of ~ 250 kHz.

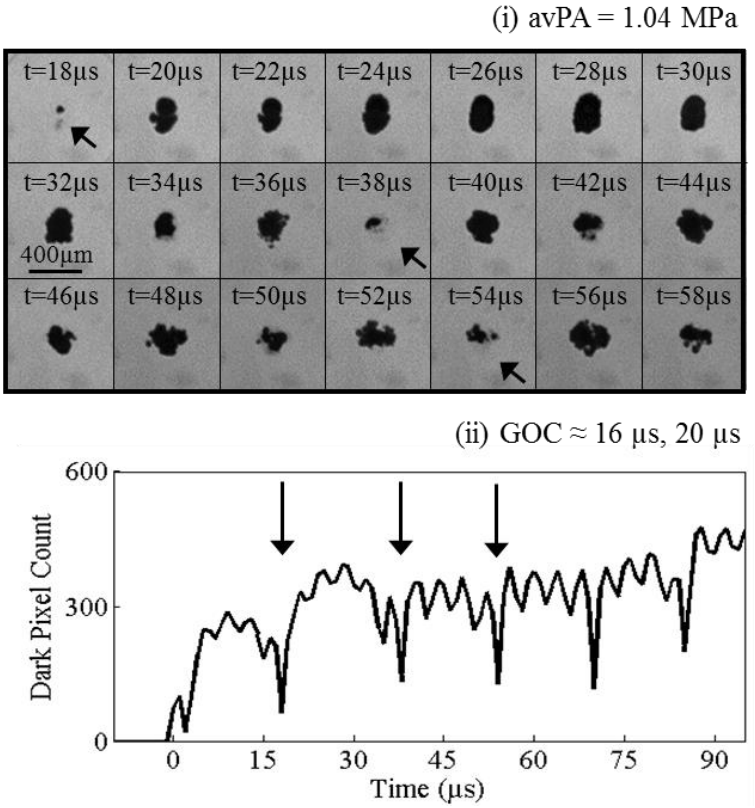

Figure 5.12. (i) High-speed image sequences illustrating cloud oscillation dynamics of switching cloud oscillation periods, 16 and 20 µs and (ii) dark-pixel counting algorithm Specifically GOC ≈ 16 and 20 µs ($f_0/4$ and $f_0/5$) at 1.04 MPa.

The inflation / deflation between collapse periods is also demonstrated in fig. 5.12. (ii) dark-pixel count over time, where it is represented by a saw tooth profile, between a minimum pixel count (arrowed), t = 38 and 54 µs respectively.

5.8 Discussion

The HSC used for this work provided 180 frames at the image-acquisition rates required to resolve cavitation dynamics, driven by HIFU in the 100's of kHz regime.

Moreover, sufficient PCD data can be collected over this time-scale for meaningful analysis, and direct correlation to the resolved cloud dynamics. The combination of imaging duration and temporal resolution, together with synchronous pulsed-laser illumination, facilitated the novel observation of a significant number of periodic shockwaves emitted from single clouds of cavitation bubbles over ~50 cycles of HIFU insonation, across a range of intensities. A relatively large field of view ensured that no shockwaves were missed during high-speed sequence acquisition, despite the 20 ns effective exposure time, per frame, provided by the pulsed laser illumination.

Systematically increasing the pressure amplitude of the HIFU increased the period of shockwave emission, in accordance with the growth, oscillation and collapse cycles observed for the clouds. The most significant finding of this research is that the shockwave emission occurred at frequencies subharmonic to the driving, and at higher orders for higher pressure amplitude, up to $f_0/5$. At HIFU avPA values intermediate to those reported, stable periodic shockwave emission was not observed. This was either manifested as a switching between the shock-periods of the stable emission avPA values above and below the intermediate value, or a failure to undergo the strong collapses required to generate observable shockwaves. In both cases, the associated acoustic data was ambivalent, with no clear spectral features apparent. Reconciling the acoustic profiles of the shockwaves to the repetitive collapses of the observed cavitation clouds and the power spectra of the PCD signals, fig. 5.8, confirmed that periodic shock-emission provides a previously unidentified source for the cavitation subharmonic signal. Subtraction of the acoustic profile of the shockwaves from the overall PCD recording of the cloud emissions, and consequent purging of the subharmonic peaks from the spectra,

fig. 5.7 (f), demonstrated conclusively the role of the periodic shockwaves. The shockwave nature underpinning this mechanism of subharmonic signal generation, has particular significance in terms of the optimisation of detection devices. It is worth noting that individual shockwaves are inherently broadband in the frequency domain (Lauterborn and Kurz, 2010, Leighton, 2012). Indeed, the PCD used for this work was made from PZT, thus the voltage spikes visible in fig. 5.6 (a, c, e and g) correspond to periodic shockwaves striking the PCD surface, which rise the voltage amplitude above the detected fundamental, and that the spectral features arise from the periodicity of shock-emission. It can also be noted that the amplitude of the raw signal increased over time, this is more evident in fig. 5.6 (e, g). At greater driving pressure amplitudes the number of daughter bubbles contained within the cloud increases, due to fragmentation, increasing the cloud diameter, this may have an effect of increasing the ultrasound scatter from the cloud surface area, which may cause an increase in signal amplitude over time. Ultimately, this PCD has demonstrated the detection of shockwaves and corresponding frequency spectrum, but the material PZT is not optimal for signal analysis, due to the ringing phenomena, previously discussed in chapter 4.

The generation of a single shockwave from a transient HIFU-generated hemispherical cavitation cloud, collapsing under static ambient pressure in proximity to a surface, has been observed before (Brujan et al., 2012). This study used high-speed imaging at 200 Mfps, over a shorter observation duration, and reported an initial shockwave propagation speed of ~ 2600 ms^{-1}. However, they also noted rapid deceleration of the shock within 20 ns of emission, to a velocity of 1500 ms^{-1} as observed in this study. Moreover, the critical role of cloud collapse in applications such as material

erosion has been demonstrated (Birkin et al., 2011). In this chapter, the link between periodic collapse from a continuously driven cloud, coincident shock-emission, and the cavitation subharmonic signal is established, potentially consolidating a growing volume of literature that links cavitation related effects to the onset of the subharmonics (see §3.5). This suggests that cloud dynamics, arising from a number of mutually interacting component bubbles in close proximity, could be a key factor to cavitation-mediated effects, rather than the activity of single bubbles responding to an insonation individually.

The period-doubled, half-harmonic response of the cloud at lower pressure HIFU driving at f_0, and the successive higher-order subharmonic cycles on increasing the pressure amplitude, indicates that the cloud system progresses through several regimes of non-linearity (Lauterborn and Kurz, 2010). Further work is certainly required to theoretically describe this response in terms of a bubble-ensemble responding to continuous acoustic driving. Understanding intra-cloud collapse dynamics at the component bubble scale is, however, a significant challenge, particularly for densely packed clouds of a large number of component bubbles, such as those observed here. One model of cloud collapse, proposed by Hansson and Mørch (Hansson and Mørch, 1980) in an attempt to explain material erosion effects, considered the collapse of cylindrical and hemispherical clouds of bubbles in the vicinity of surfaces, driven by an ultrasonic horn operating at 20 kHz. It was suggested that a series of inwardly collapsing shells, with the energy from the collapse of one shell amplifying the collapse of the next, was a plausible mechanism for reaching the conditions required to yield the observed erosion. The observations of multiple-front shockwaves of fig. 5.5 (d) and fig. 5.9 indicate that sub-clusters within a cloud under higher driving pressure amplitudes, and far from any

surfaces, indeed collapse at different times and at distinct locations within the cloud, but do not seem to conform to the sequential shell-model. Therefore, multiple front shockwave observation may provide a tool with which intra-cloud collapse may be probed for high void fraction systems, and at nanosecond temporal resolution.

5.9 Conclusion

This chapter presents conclusive experimental evidence for a source of the cavitation subharmonic (and higher-order subharmonics) signal, that applies to strongly driven bubble cloud systems. Via high-speed shadowgraphic imaging, clouds are observed to undergo growth, oscillation and collapse cycles, periodically emitting shockwaves coincident to the moment of collapse. The results have demonstrated that for oscillating cloud systems the subharmonic is a discretely, rather than continuously, emitted signal. The GOC cycles, frequency of shockwave emission, and therefore order of the subharmonic detected, are primarily determined by the pressure of the insonation.

The stable oscillation of some of the component daughter bubbles between the collapse of the cloud and emission of shockwaves form some component bubbles that do collapse, may suggest that subharmonic cloud behaviour has characteristics conventionally associated with both stable and inertial cavitation classification. This hints at a requirement for a broad stable-inertial category in line with recent speculation in the literature (Church and Carstensen, 2001), with $f_0/2$ marking the first transition from 'true-stable' and higher orders representing steps toward the inertial end of the scale.

6 Deconvolution of acoustic data

The previous chapter demonstrated periodic shockwaves (PSWs) as a source of the subharmonic signal using a passive cavitation detector (PCD) that was not optimal. The results presented in §6.4 at the end of this chapter are more recent experimental data, with cavitation acoustically monitored using a commercial PVdF needle hydrophone, for which phase and magnitude calibration was obtained from the National Physical Laboratory, NPL. This allows the detector response to be deconvolved[8] from the voltage data, such that the cavitation emissions, including PSWs, may be presented in terms of pressure amplitude. The relatively low peak positive amplitude (PPA) of PSWs are thus demonstrated, validating the requirement for a shockwave PCD (swPCD) designed to maximise sensitivity to a shockwave. This will form the basis of Chapter 7.

However, to assess the effects of detector deconvolution of shockwave data, a more reliable source of shockwaves is required. For this purpose, laser-induced bubbles (LIB), for which the optical breakdown shockwave (OBSW) and bubble collapse shockwave (BCSW) PPAs are known to be directly related to the R_{max} of the bubble that forms, are used (Noack et al., 1998, Philipp and Lauterborn, 1998). The results are analysed for an apparent negative phase within the shockwave profile, which is revealed as a hydrophone convolution artefact. Simulated shockwave profiles are generated via the Gilmore equation for bubble oscillation, which is solved according to the resolved LIB collapse

[8] The results presented in this chapter are from (Johansen, K. Song, J. Johnston, K. & Prentice, P. 2016. Deconvolution of acoustically detected bubble-collapse shockwaves. Ultrasonics). Which is currently under second stage review process.

(see §6.2.2). The simulated shockwave profiles are compared to the needle recordings at various distance from nucleation. A second model will be introduced to simulate the OBSW, and this will be discussed in §6.3. Both simulated profiles will form the input parameters of a PZFlex finite element model, to aid in the development of the swPCD, Chapter 7

To accommodate the needle hydrophone (and the other PCDs), a new open-architecture sonoptic chamber was required. This chapter starts with a description of the commercial HIFU source, sonoptic chamber Version 2 (V.2) and materials and methods used for experiments.

6.1 Material and Methods

6.1.1 The commercial HIFU source

The commercial transducer (H-149 Sonic Concepts, Bothell USA) has an outer diameter of 110 mm, operates at f_0 = 220 kHz and is a geometrically focused to a focal length of 70 mm. Moreover, it has a 20 mm through opening in the centre of the device, into which the Sonic Concepts PCD (or shockwave PCD can be inserted, see §7.1.2). The transducer is driven using a waveform generator (DG4102, Rigol Technologies, Beijing China) and a power amplifier (2100L, Electronic and innovation, NY, USA), via a matching network (Sonic Concepts).

6.1.2 Sonoptic chamber Version 2 and high-speed imaging

The sonoptic chamber V.2 has a rectangular open-architecture design, with dimensions of 420 × 438 × 220 mm^3. Two of the walls are recessed to allow the placement of imaging optics in proximity to the intended location of the cavitation activity. A laser pulse is brought to a focus through a long working distance microscope objective lens

(50× 0.42 NA Mitutoyo, Japan), submerged in a sealed unit, and mounted on a xyz manipulator (Velmex Motor, Bloomfield, NY, USA). This laser (green) is used to initiate the cavitation activity, fig. 6.1.

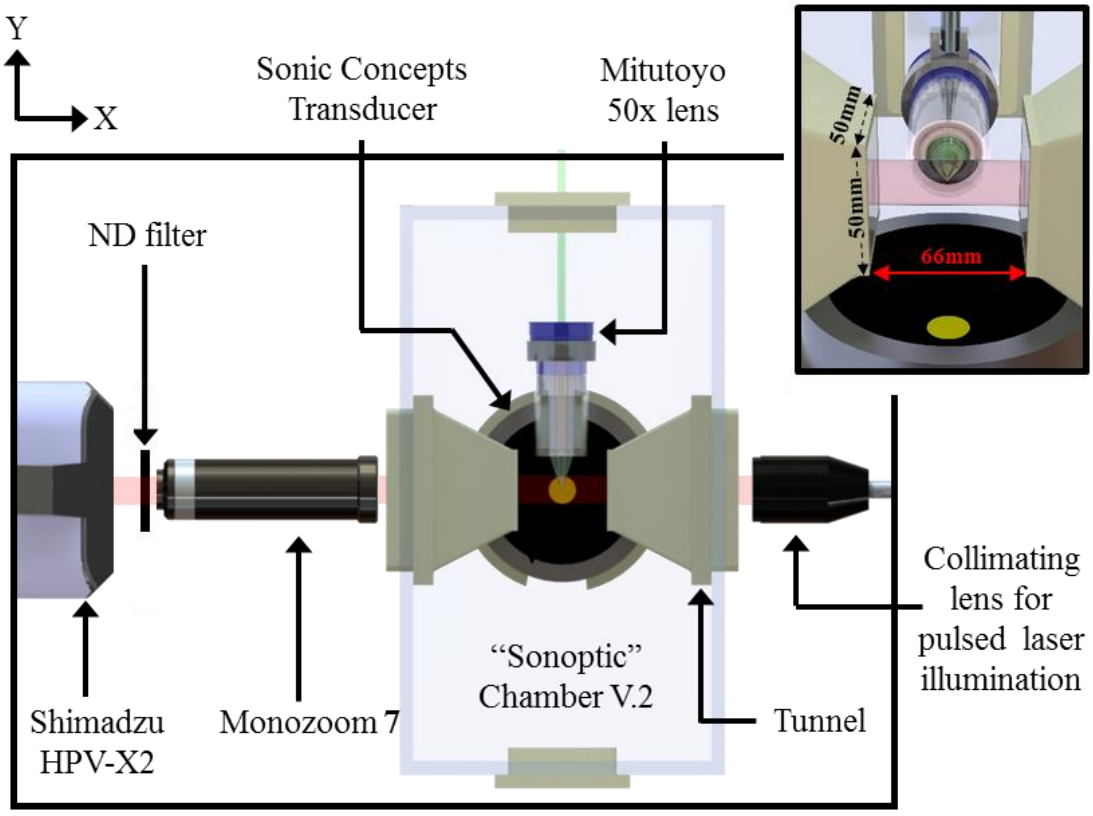

Figure 6.1. Top view of the sonoptic chamber V.2, including high-speed camera and pulsed laser illumination configuration .Inset top right is the commercial HIFU source and nucleation objective lens positioned inside a sealed unit. The approximate distance between the two tunnels (arrowed) is ~66 mm, which is large compared to the 4.87 mm measured focal width of HIFU source, measured by scanning the needle hydrophone through the focus (Precision Acoustics).

The V.2 chamber also accommodates a commercial transducer described above, positioned on a rapid prototyped base, designed to let the ultrasound propagates upward, without disturbance from the tunnels (arrowed), fig. 6.1. Free-field mapping using the 1 mm needle hydrophone (Precision Acoustics) revealed a -6 dB focal width, 4.87 mm and

axial focal length, 22.36 mm, fig. 6.2. The focal width is small compared to the distance between the two tunnels ~ 66 mm; this indicated that distortion of the HIFU field from the tunnels would be negligible.

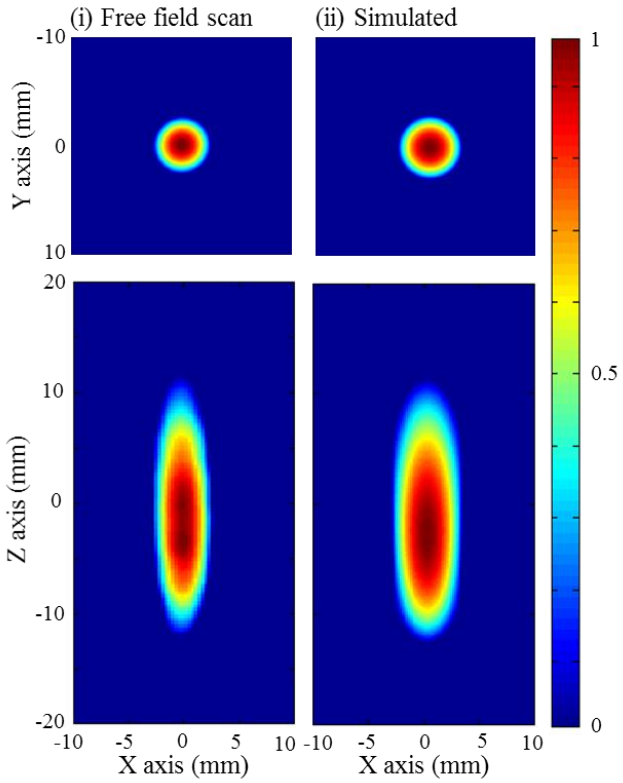

Figure 6.2 Sonoptic chamber V.2 field mapping carried out via needle hydrophone and simulation of HIFU field using field II simulator. Measure -6dB focal width, 4.87 mm and axial focal length, 22.36mm.

High-speed shadowgraphic imaging is undertaken with a Shimadzu HPV-X2 camera (Shimadzu, Kyoto, Japan), recording 256 frames (400 x 250 pixels) at up to 5 Mfps through a Monozoom 7 imaging lens, set to 4x magnification with a 2x outer lens attached. Illumination is achieved with synchronous 10 ns laser pulses (CAVILUX Smart, Cavitar, Finland). The spatial resolution was determined to be 7.1 ± 0.1 μmpixel^{-1}. A secondary xyz manipulator is used to the position the needle hydrophone vertically above the cavitation dynamics or orthogonally to the HIFU axis for detecting laser nucleated

acoustic cavitation LNAC (see §6.4). Acoustic absorber is positioned at the top of V.2 to minimise reflections of the ultrasound from the water surface, fig. 6.3.

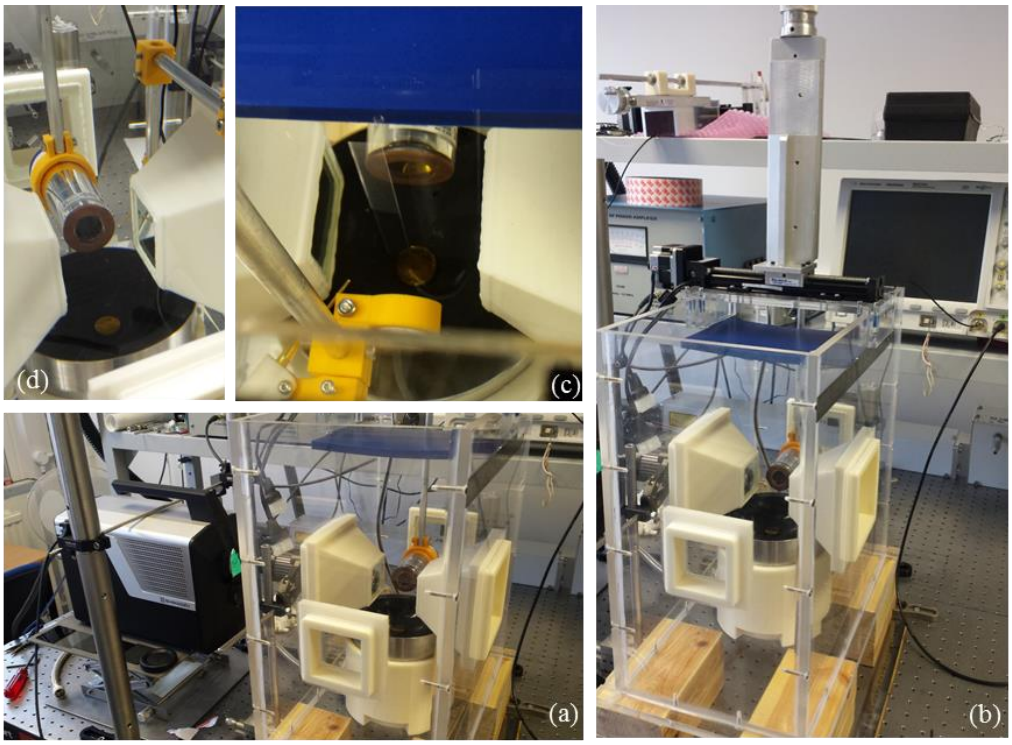

[9]

Figure 6.3. Photographs of sonoptic chamber V.2 (a) Shimadzu HPV-X2 HSC and sonoptic chamber V.2. (b) Visible in the top centre of the photo is the xyz manipulator that was used to micro position the laser nucleation optics relative to the transducer focus. Also visible on the first shelf is the power amplifier, oscilloscope and on the second shelf, (top left) a secondary xyz manipulator for adjustment of the needle / PCD (c) Experimental setup of Sonic Concepts PCD (gold circle), needle hydrophone and swPCD. Sonic concepts position inside the through opening of transducer and the swPCD and needle secured to a xyz manipulator via a holder designed using SolidWorks. Also visible is acoustic absorber to minimise reflections (d) Laser nucleation objective, enclosed in a sealed unit to prevent water damage and the commercial Sonic Concepts HIFU transducer, positioned so the focal region is between two tunnels.

Acoustic cavitation was nucleated using the method previously described in §5.1.2 and a LIB was nucleated by increasing the laser power above breakdown threshold, 4.0 ±

[9] The author acknowledges Miss Miriam Jimenez Garcia for designing and developing the sonoptic chamber V.2.

0.2 mJ (instrument error according to manufacturer) and without ultrasound. LNAC experiments were initiated using a manual trigger mode via the voltage waveform generator, which triggered the delay generator and a 60-cycle burst at 220 kHz for power amplification. The delay generator triggered the HSC, nucleation laser, oscilloscope and illumination laser. The auxiliary output of the HSC synchronised a square TTL pulse signal with the CAVILUX control box dependant on the selected frame rate. A schematic of the complete experimental setup for V.2 is given in fig. 6.4.

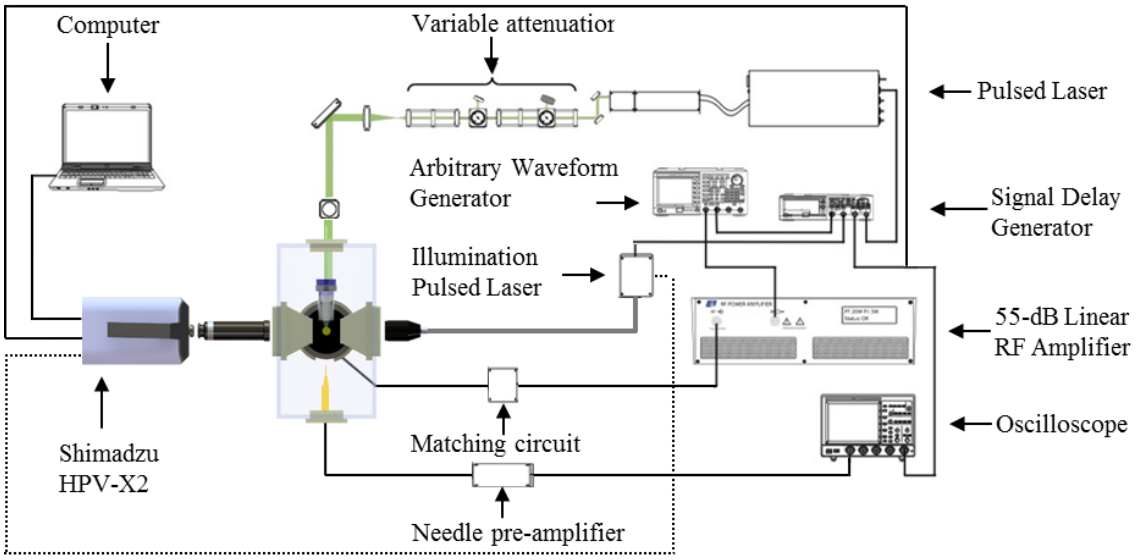

Figure 6.4. Schematic of complete experimental setup V.2 Schematic overview of the sonoptic chamber V.2, Shimadzu HPV-X2 and driving electronics. Solid lines refer to BNC trigger or signal lines, dashed line refers to the auxiliary output from HSC to synchronise with pulsed laser illumination. In this setup, the 1mm needle hydrophone was positioned orthogonally inside the chamber at ~ 70mm from HIFU focal region for LNAC.

6.1.3 Needle hydrophone

Shockwave detection was carried out using a commercial needle hydrophone (1.0 mm, 28 µm thick active element, Precision Acoustics, UK) supplied with pre-amplifier and End-of-cable calibration for magnitude and phase over a bandwidth of 125 kHz to 20 MHz provided by National Physics Laboratory (NPL), fig 6.5.

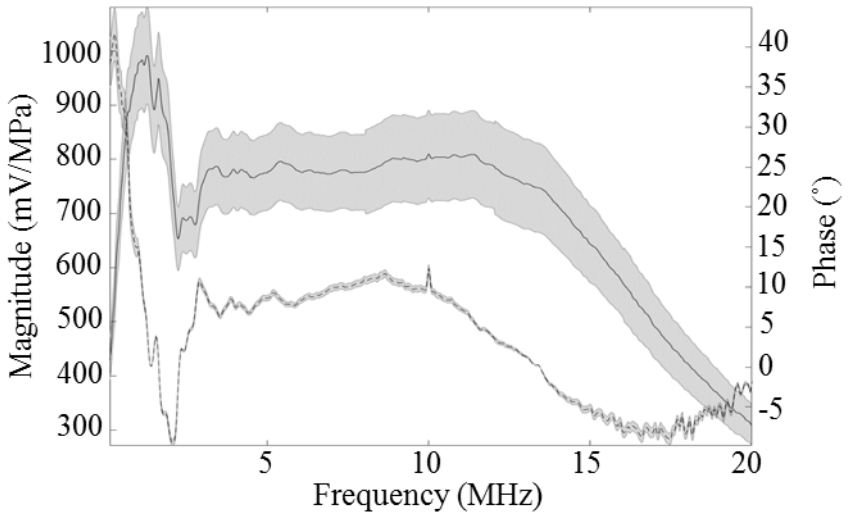

Figure 6.5. Phase and magnitude calibration of 1mm PVdF needle hydrophone End-of-cable magnitude (solid) and phase (dash) response for the needle hydrophone and pre-amplifier, over a bandwidth of 125 kHz to 20 MHz in 25 kHz increments. Uncertainties are represented by the grey shading at 9 – 12% for the sensitivity and 4 – 8 % for the phase, as provided by NPL. Note significant fluctuations <5MHz, which indicate full wave form deconvolution is necessary.

The needle type-hydrophone is used for bubble collapse shockwave detection (Vogel et al., 1996, Brujan and Vogel, 2006). However, the fluctuations in both magnitude and phase illustrate the non-flat response of the hydrophone and the need for detector deconvolution when measuring a broadband signal. Therefore, it is not ideal for making such a measurement of broadband signals (Harris et al., 2000), as it will distort the measurement, both with regards to the temporal shape and the relative magnitudes of

the different frequency components (Hurrell, 2004, Shaw and Hodnett, 2008). However by obtaining both phase and magnitude calibration and full through waveform deconvolution BCSW waveforms can be reconstructed, so measurement of the PPA can be obtained and also PPA from LNAC. Membrane detectors have been developed with a smooth and predictable frequency response, for such a detector single-frequency calibration is sufficient (Wilkens et al., 2016).

Nevertheless, the small diameter of the needle, compared to a membrane, was considered a better choice, as the needle can more easily be combined with other PCDs and be positioned at various locations in V.2, to measure OBSW, BSCW or PSWs from LNAC.

6.1.4 High-speed camera observations

Acoustic BCSW measurements were undertaken with the needle positioned vertically above the laser focus at distances of 30, 40 and 50 (±0.5) mm, in combination with HSC imaging at 5 Mfps, fig. 6.6. At these distances, the angle subtended by the 1 mm active area of the needle hydrophone is < 1°, and the shockwave may be assumed planar to a first approximation. At shorter distances, the curvature of the shockwave would have a more pronounced effect on the measured characteristics, including the full width half maximum (FWHM).

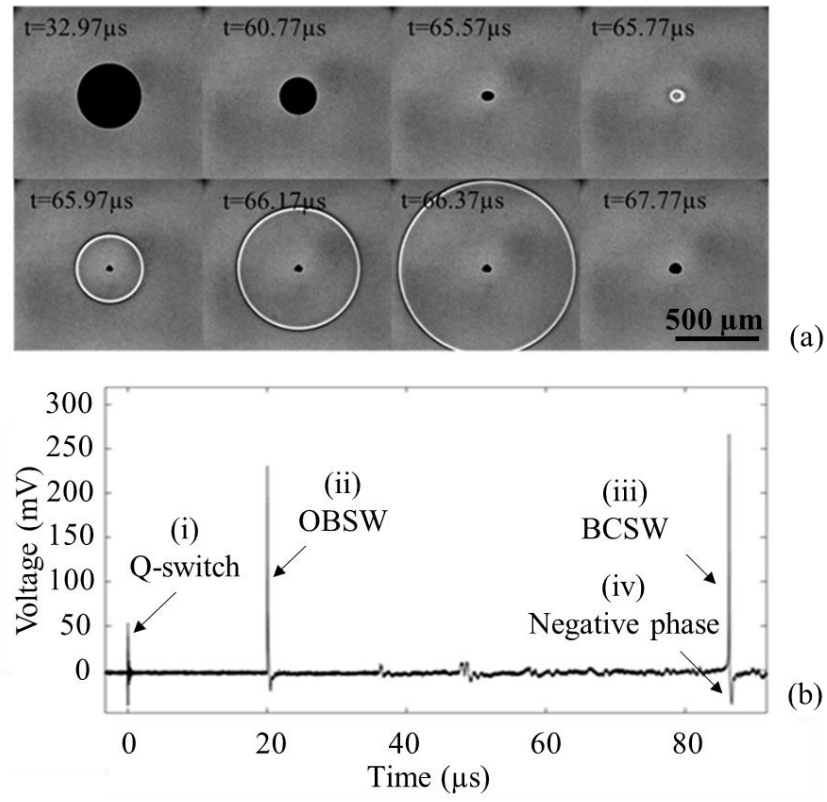

[10]

Figure 6.6. High-speed images of a LIB collapse, BCSW generation and rebound and needle hydrophone voltage trace (a) Representative high-speed images of an LIB collapse, BCSW generation and rebound, recorded at 5 Mfps. (b) A full needle hydrophone voltage trace, recorded at 30 mm, with key features described in the text, arrowed. Note, there is ~ 20 µs propagation time for the shockwaves between the high-speed imaging capture and hydrophone detection.

Fig. 6.6 (a) are representative frames extracted from a single high-speed image sequence, for the collapse of a LIB and emission of BCSW. The criteria for an LIB collapse and BCSW to be included in the dataset from which profiles is considered, are (i) an R_{max} = 365 ± 4 µm, fig. 6.6. (a) at 32.97 µs, (ii) single fronted BCSW generation,

[10] Many thanks to Kristoffer Johansen for the results depicted in section 6.2. Kristofer was instrumental for the development of the Gilmore model, post processing of the experimental data (collected by the author), preparation of figures and corresponding discussions, particularly the negative phase of a BCSW.

fig. 6.6 (a) from 65.97 – 66.37 μs, and (iii) a spherical post-collapse rebound, fig. 6.6 (a) at 67.77 μs. It is well known that the size of a bubble is critical in determining the amplitude of the BCSW generated when it collapses (Brujan et al., 2012). To make meaningful comparisons between BCSW profiles at different propagation distance, (i) is therefore critical. It is also well reported that due to spherical aberration, there is an extended focal region for a laser pulse passed through an objective lens. The plasma generated, and the LIB that forms, will therefore be slightly elliptical (Kröninger et al., 2010), which is seen at 65.57 μs, fig. 6.6 (a). A common observation made during the collection of this data was that in the event that the plasma generated on laser pulse absorption is too extended, the collapse could occur at two separate locations, generating a double-fronted shockwave. Moreover, for such cases, the rebounded bubble will have fragmented, and such data was not considered further.

Fig. 6.6 (b) is the voltage trace recorded by the needle hydrophone during the LIB collapse of fig. 6.6 (a). Notable features are arrowed, including (i) the Q-switch of the laser, indicating laser-pulse emission, which is taken as t = 0 μs for all data presented, (ii) the OBSW indicating laser absorption and plasma formation, (iii) the BCSW, and (iv) the apparent negative phase of the BCSW.

An important characteristic of any hydrophone used to measure a shockwave is the rise time (see §3.6), in response to a unit step function. The OBSW has an abrupt rise to maximum signal (Vogel et al., 1996), within a few ns – in contrast to that of the BCSW, which has a much smoother transition to PPA, due to the bubble emissions as it deflates into the collapse, fig. 6.6 (b) – which can be used to approximate an impulse response.

Accordingly, an upper bound of 22.5 ns was deduced as the rise time for the needle hydrophone used in this work. This suggests that the needle hydrophone has actual bandwidth beyond the 20 MHz calibration limit. All measured shockwave FWHMs stated in the results below are greater than this upper bound, and can therefore be taken as representative (Vogel et al., 1996).

6.1.5 Bubble collapse shockwave generation model

There are many Rayleigh-Plesset-like equations in the literature that account for liquid compressibility (Keller and Miksis, 1980, Herring, 1941, Gilmore, 1952, Flynn, 1975, Kreider et al., 2011). These equations become relevant when the Mach number $\frac{\dot{R}}{c_0}$ becomes 'small' during expansion (Prosperetti and Lezzi, 1986), where c_0 is the speed of sound far from the bubble, and $\dot{R}$ is the bubble wall velocity. Examples of first order formulations are the Keller-Miksis (Keller and Miksis, 1980) and Herring-Trilling (Herring, 1941) equations, whereas the Gilmore equation contains additional second order terms (Gilmore, 1952). As the Gilmore equation depends on the liquid enthalpy, *H*, at the bubble wall, it is well suited to study inertial collapses (Prosperetti and Lezzi, 1986). Hence, the Gilmore equation is used in this work. The formulation presented is taken from Kreider with some modifications (Kreider et al., 2011).

The Gilmore equation can be represented the following way:

$$\left(1-\frac{\dot{R}}{C}\right)R\ddot{R}+\frac{3}{2}\left(1-\frac{\dot{R}}{3C}\right)\dot{R}^2=\left(1+\frac{\dot{R}}{C}\right)H+\left(1-\frac{R}{C}\right)\frac{R}{C}\dot{H} \qquad (6.1)$$

where the overdot represents the time derivative, R is the instantaneous radius, and C the instantaneous speed of sound evaluated at the bubble wall, respectively. Using a

modified form of the Tait equation for the liquid state to express C and H explicitly (Macdonald, 1966).

$$p = p_0 + \frac{1}{b\Gamma}\left[\left(\frac{\rho}{\rho_0}\right)^{\Gamma} - 1\right], \tag{6.2}$$

where p_0 is the ambient pressure, b and Γ are empirically determined constants, ρ and ρ_0 are the instantaneous and ambient densities of the liquid, respectively. $\Gamma = 6.5$ was chosen from data for water (Macdonald, 1966), and b is defined the following way $b = (\rho_0 {c_0}^2)^{-1}$. The enthalpy H and the speed of sound C at the bubble wall is expressed as:

$$H = \frac{(b\Gamma)^{\frac{-1}{\Gamma}}}{\rho_0}\frac{\Gamma}{\Gamma-1}\left[(p_w - B)^{\frac{(\Gamma-1)}{\Gamma}} - (p_0 + B)^{\frac{(\Gamma-1)}{\Gamma}}\right], \tag{6.3}$$

And

$$C^2 = c_0^2 + (\Gamma - 1)H, \tag{6.4}$$

where $B \equiv ((b\Gamma - p_0))^{-1}$ and p_w is the pressure at the bubble wall, where p_w can be expressed as

$$p_w = p_i - \frac{4\mu\dot{R}}{R} - \frac{2\sigma}{R}, \tag{6.5}$$

where p_i is the internal pressure in the bubble, μ is the shear viscosity of the surrounding liquid and σ the surface tension at the gas-liquid interface. Assuming that the internal pressure is uniform, it can be represented as

$$p_i = \left(p_0 + \frac{2\sigma}{R_0}\right)\left(\frac{R_0^3 - mR_0^3}{R^3 - mR_0^3}\right)^{\kappa} \tag{6.6}$$

where R_0 is the equilibrium radius of the bubble, and m is the van der Waals core parameter, chosen as $m = 0.11$, κ is the polytropic exponent. Now, the speed of sound and the enthalpy at the bubble wall can be explicitly expressed for implementation in a numerical scheme.

The formulation of Eq. (6.1) assumes a constant gas content of the bubble with a uniform pressure inside.

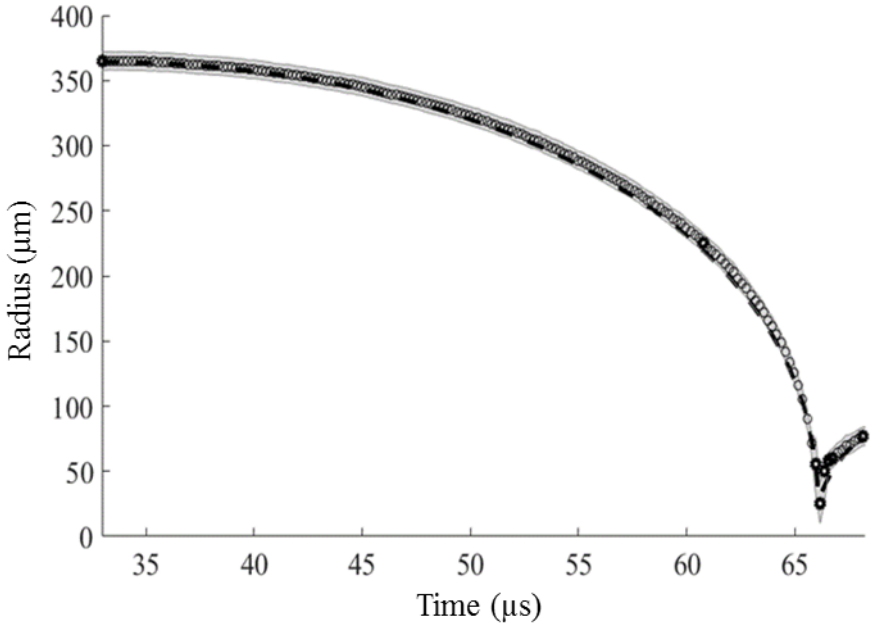

Figure 6.7. The experimental radius-time curve (circles), of the bubble collapse as depicted in fig. 6.6 (a) (bold circles are the data points of the images presented). The dashed line curve is the best fit solution of the Gilmore equation with the following parameters; $c_0 = 1484\, m\, s^{-1}$, $p_0 = 101\, kPa$, $R_0 = 61\, \mu m$, $R_{max} = 364\, \mu m$, $\rho_0 = 998\, kg\, m^{-3}$, $\sigma = 0.072\, N\, m^{-1}$and $\mu = 0.001\, Pa\, s$.

This has been shown to be an adequate assumption, even for inertial collapses. The temperate of the interior is assumed to remain uniform due to the rapid collapse of the bubble, whereby heat has insufficient time to transfer through the bubble wall (As referenced by (Lin et al., 2002)). A recent finite volume investigation of the collapse of a

laser bubble, demonstrated that there are differences in both the internal pressure of the bubble, and the maximum rebound radius, compared to that predicted by the Gilmore equation (Koch et al., 2016). Evaporation, condensation, gas diffusion through the bubble wall, and heat conduction are neglected.

The circle scatter plot of fig. 6.7 is the radius measured from each frame of the high-speed sequence of the single LIB collapse, represented in fig. 6.6. (a). Other LIB radius-time curves reported have been at higher frame rates, but these results rely on compiling the curve from multiple sequences of different LIBs, assuming identical bubble behaviour (Vogel et al., 1996, Kröninger et al., 2010).

Solving Eq. (6.1) for the bubble deflation, collapse and rebound, dashed curve of fig. 6.7, allows the dynamics around the simulated collapse to be probed in more detail. The acoustic emission as a spherical wave, P_{rad}, can be calculated the following way (Brennen, 2015) :

$$P_{rad} = \rho_0 \frac{R^2\ddot{R} + 2R\dot{R}^2}{r}, \tag{6.7}$$

where r is distance from the centre of the cavity. This approach is used to generate the simulated shockwave profiles, presented in dashed line, figs. 6.9 – 6.11. Simulated shockwave profiles at all propagation distances are computed with a bandwidth of 100 MHz.

6.1.6 Deconvolution of hydrophone data

Deconvolution of the needle hydrophone data, (Hurrell, 2004) is performed in the frequency domain, according to Eq. (6.8)

$$P(f) = V(f)/M(f) \times H_{bpf}(f)\,, \tag{6.8}$$

where $P(f)$ is the deconvolved signal, $V(f)$ the voltage signal, $M(f)$ the complex sensitivity, and $H_{bpf}(f)$ a bandpass filter, fig. 6.8 (a), implemented in the frequency domain and matching the calibration bandwidth of 125 kHz to 20 MHz.

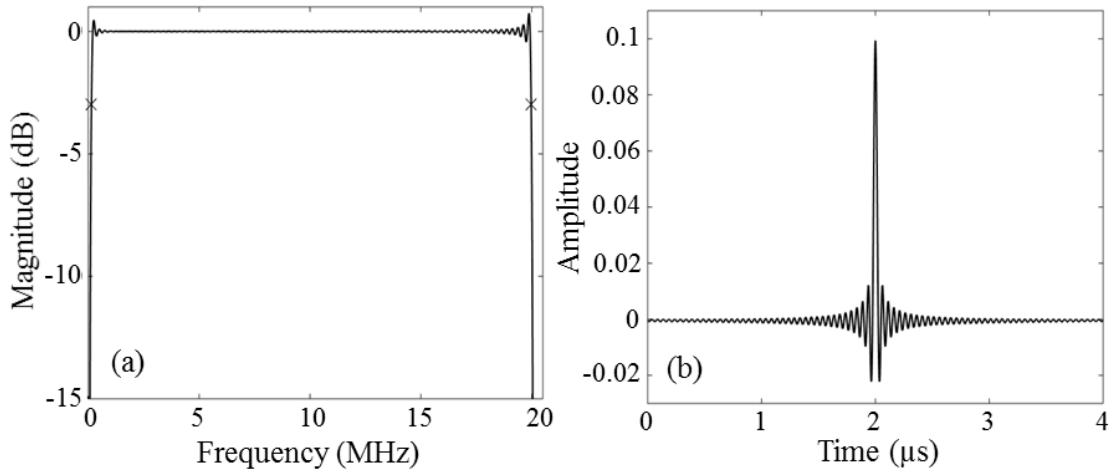

Figure 6.8. (a) Magnitude response of bandpass filter, $H_{bpf}(f)$, with the -3 dB corner points, at 145 kHz and 19.9 MHz marked ×, and (b) impulse response in the time domain.

Applying an inverse Fourier transform, the deconvolved signal is obtained in the time domain. Magnitude-only deconvolution follows an equivalent process, assuming the phase, $\varphi = 0^{\circ}$, for all frequencies. Uncertainties in the frequency domain are computed in accordance with (Eichstädt and Wilkens, 2016)

6.2 Results

6.2.1 Single-frequency calibration

Accordingly, and within experimental error of the high-speed imaging data, fig. 6.6 (a), the BCSWs presented may be considered as representative of the propagation of a single shockwave, such that propagation effects may also be assessed. Close to the

bubble location, it may be expected that the BCSW speed is supersonic, and that the PPA decays as ~ r^{-2}, (Vogel et al., 1996). At the measurement distances of 30 – 50 mm, it is expected that the pressure amplitude decays as ~ r^{-1} (Vogel et al., 1996, Brujan et al., 2012). As such, broken r^{-1} envelopes are included across the peak pressures in each shockwave representation, fig. 6.9. including for the simulated data, according to Eq. (6.7).

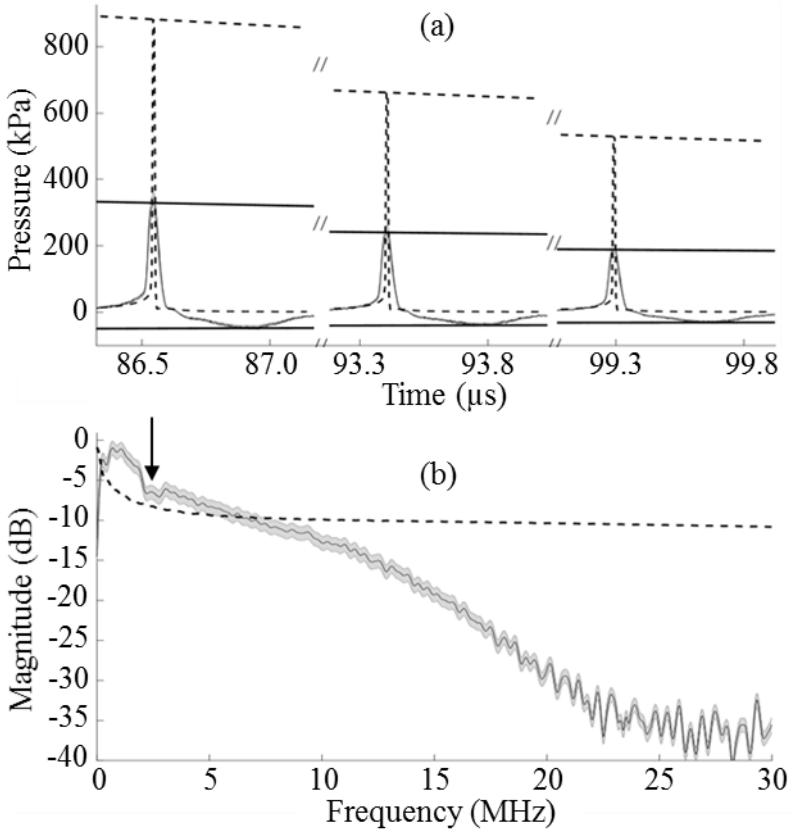

Figure 6.9. (a) Single-frequency calibrated hydrophone signal (black with grey shaded uncertainty), with the calibration value at 10 MHz, for BCSWs measured at propagation distances of 30, 40 and 50 mm, and the simulated shockwave profile prediction (black dash). (b) Frequency spectra of the single-frequency calibrated signal (black with grey envelope) and simulated shock (black dash) at r = 30 mm, normalised to the experimental data.

	Single frequency calibration			Simulated shock profile		
Prop distance (mm)	RT (ns)	FWHM (ns)	PPA (kPa)	RT (ns)	FWHM (ns)	PPA (kPa)
30	71	46	329 ± 36	5	10	883
40	53	47	240 ± 26	5	10	662
50	57	46	188 ± 21	5	10	529

Table 6.1. Shockwave properties from fig. 6.9. (a), including rise time (RT), full width half maximum (FWHM) and peak positive pressure amplitude (PPA), for single-frequency calibration and simulated shockwave profile, at each of the propagation distances.

The shock profiles of fig. 6.9 (a), solid black line, are single-frequency calibrated BCSWs, converted from voltage to pressure using the magnitude sensitivity at 10.0 MHz, which is 810.0 ± 8.1 mV/MPa. This frequency was selected as typical of how bubble shockwave literature is reported, and it is within the flat bandwidth of the needle hydrophone, fig. 6.5, making it an adequate choice for demonstrating the assumption and implications of a flat frequency response. The time waveform shape of the profile is otherwise identical to the voltage signal detected by the hydrophone. The black-dash profiles of fig. 6.9 (a) are the BCSWs predicted by the acoustic emissions computed by Eq. (6.7), from the solution of the Gilmore equation, with notable differences to those measured. In particular, the pressure amplitudes of the model profiles are around 2.5× measured values, and the FWHM less than 25% of those measured, Table 6.1. Furthermore, the experimental profiles all exhibit an apparent negative phase, lasting ~ 0.5 μs and propagation independent, trailing the compressive phase of the shockwave. The amplitude of the apparent negative phase also follows the r^{-1} decay, exhibited by its positive pressure counterpart.

Fig. 6.9 (b) are the frequency spectra of the experimental and simulated BCSW, at r = 30 mm. The shape of the spectrum, convolved with the hydrophone response, is best considered relative to the calibration data of fig. 6.5. The steeper fall-off in the magnitude of frequency components > 12 MHz corresponds to the marked decrease in magnitude sensitivity exhibited > 12 MHz. Moreover, the dip (arrowed, fig. 6.9. (b)) in the magnitude of the experimental BCSW spectrum, from 2 to 3 MHz, is likely due to the structure in the magnitude calibration data over the same frequency range, fig. 6.5. The unfiltered simulated shockwave with its 100 MHz bandwidth and greater magnitude at higher frequencies, compared to the measured shockwave, predictably has a narrower FWHM in the time domain, fig. 6.9 (a).

6.2.2 Magnitude-only deconvolution

The frequency content of the experimental single-frequency calibrated BCSW falls to -30 dB above 20 MHz, which gives some confidence that treating the BCSW profile within the calibration bandwidth is reasonable, *i.e.*, for an assessment of order of magnitude for PPA. For subsequent comparisons between simulated and experimental measurements, $H_{bpf}(f)$ is therefore applied to the simulated shockwave profiles and spectra, such that the bandwidths considered are equivalent.

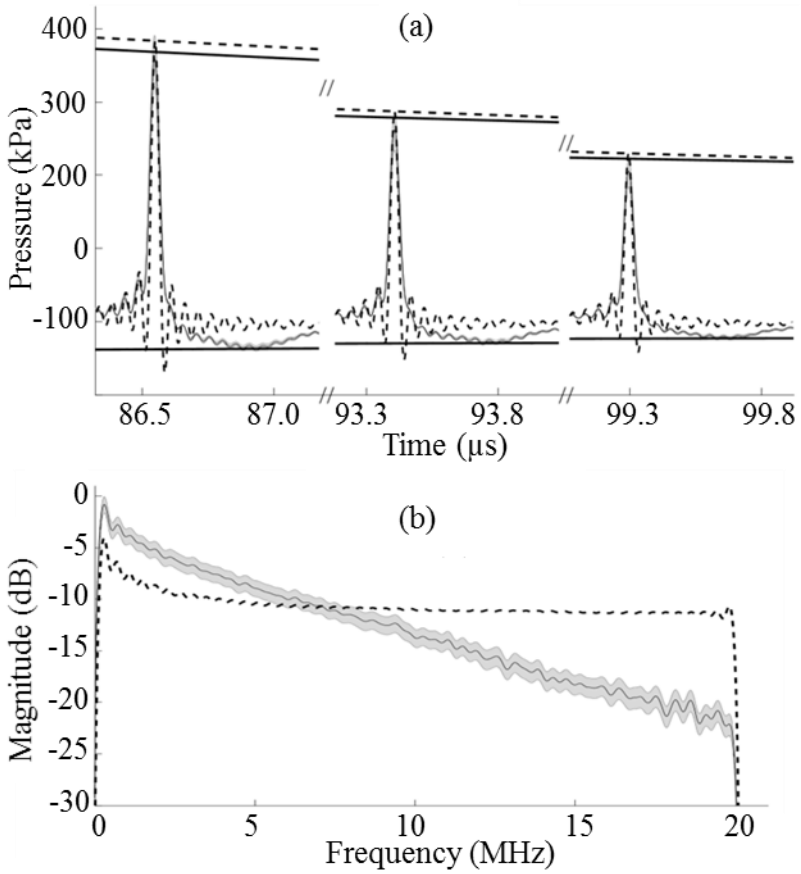

Figure 6.10. (a) Magnitude-only deconvolved hydrophone signal (black with grey shaded uncertainty), at propagation distances of 30, 40 and 50 mm, and filtered simulated shockwave profile (black dash). (b) Frequency spectra of the magnitude-only deconvolved signal (black with grey envelope) and simulated shock (black dash) at r = 30 mm, normalised to the experimental data.

Magnitude-only deconvolution			Simulated shock profile	
Prop distance (mm)	FWHM (ns)	PPA (kPa)	FWHM (ns)	PPA (kPa)
30	44	359 ± 38	31	383
40	44	261 ± 27	31	287
50	45	205 ± 21	31	230

Table 6.2. Shockwave properties from fig. 6.10. (a) including full width half maximum (FWHM) and peak positive pressure amplitude (PPA), for magnitude-only and filtered simulated shockwave profile, at each of the propagation distances.

The experimental BCSW profiles of fig. 6.10 (a) are magnitude-only deconvolved according to Eq. (6.8), with $\varphi = 0$ for $M(f)$. Direct comparison with the single-frequency calibrated data, Table 6.1, indicates that magnitude-only deconvolution, Table 6.2, has increased the peak positive pressure amplitudes by ~ 9 %. At rapid pressure variations within the BCSW profile, a rippling artefact is introduced due the bandpass filter $H_{bpf}(f)$ suppressing frequency content outside the calibration bandwidth, as a manifestation of the Gibbs' effect, also apparent in fig. 6.8. This rippling prevents meaningful measurement of the RT of the experimentally measured shockwaves. An equivalent filter is applied to the simulated shockwave profiles of fig. 6.10 (a), black-dash, for comparison to magnitude-only deconvolved hydrophone data, which also generates the Gibbs' effect. The filtering also reduces the pressure amplitude of the simulated shockwave profiles. Note, however, that the apparent negative phase has been preserved through the magnitude-only deconvolution, in accordance with assuming $\varphi = 0^{\circ}$ for all frequencies, fig. 6.10 (a).

Fig. 6.10 (b) are the spectra of the shocks at 30 mm with the effect of $H_{bpf}(f)$ clearly evident. As expected for a shockwave generally, the experimental spectrum now decays with a better approximation to linearity in the dB scale, at increasing frequency. For all frequencies with a sensitivity lower than that at 10 MHz, fig. 6.5, the magnitude at the respective frequency components are increased according the Eq. (6.8), most notably > 12 MHz. In addition, the dip (arrowed fig. 6.9 (a)) in the spectrum of the single-frequency calibration BCSW has been removed by magnitude-only deconvolution. Comparison to fig. 6.9 (b) indicates that the pressure amplitudes for the different

frequency components are therefore better estimated in the frequency domain, compared to the single frequency calibration, as the whole bandwidth of calibration is utilised.

The Gibbs' effect is manifested in the spectrum of the simulated shockwave, fig. 6.10 (b), at the limits of the bandpass filter, and is also apparent toward the low frequency limit of the filter in the experimental spectrum.

6.2.3 Full waveform deconvolution

Fig. 6.11. depicts the full waveform deconvolution of the BCSW hydrophone data, incorporating the phase calibration data. It is observed that the apparent negative phase of the experimental BCSW profiles have been removed.

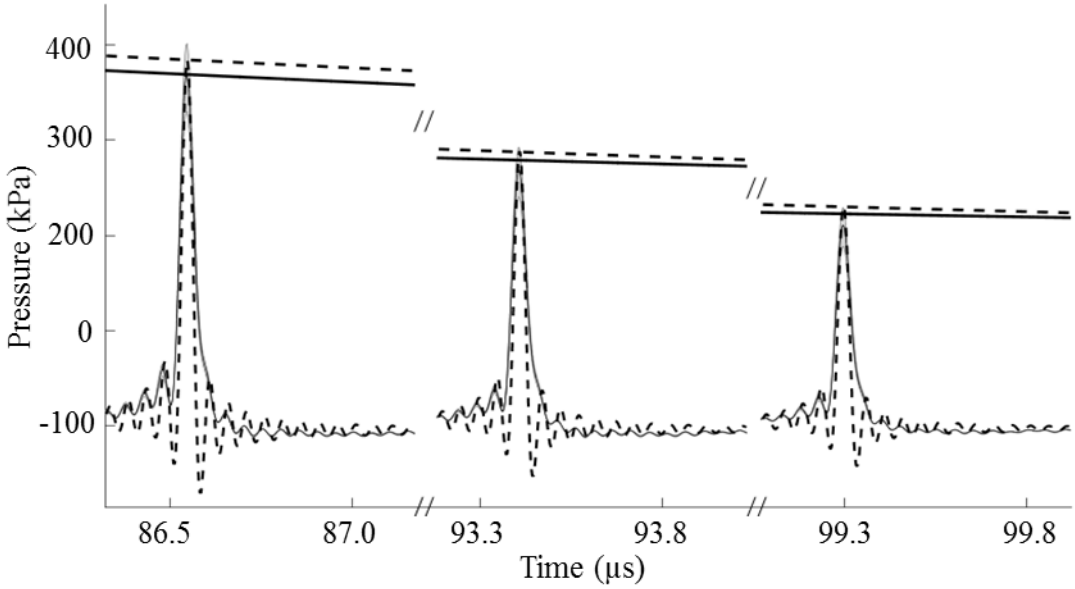

Figure. 6.11. Full waveform deconvolved hydrophone signal (black with grey shaded uncertainty), at propagation distances of 30, 40 and 50 mm, and filtered simulated shockwave profile (black dash).

	Full waveform deconvolution		Simulated shock profile	
Prop distance (mm)	FWHM (ns)	PPA (kPa)	FWHM (ns)	PPA (kPa)
30	45	368 ± 38	31	383
40	46	268 ± 28	31	287
50	47	210 ± 23	31	230

Table 6.3. Shockwave properties from fig. 6.11, including full width half maximum (FWHM) and peak positive pressure amplitude (PPA), for full waveform deconvolved and filtered simulated shockwave profile, at each of the propagation distances.

The peak positive pressure amplitude of the full waveform deconvolved profile is ~ 3 % higher at each propagation distance, than those of the magnitude-only deconvolved profiles. The peak pressure amplitudes of the filtered simulated profiles are now within the calibration error provided by NPL, of the full waveform deconvolved BCSW amplitudes, in the time domain.

The frequency spectrum of the full waveform deconvolution is equivalent to that of the magnitude-only deconvolution, fig 6.10 (b), as the magnitude in the frequency domain does not depend on the phase.

The FWHM for the experimental profiles, Table 6.3, are ~ 30 % longer than those of the filtered simulated profiles. This is due to the filtered simulated profiles having higher magnitude than the experimental profiles from ~ 10 MHz, and lower magnitude for frequencies below, fig. 6.10 (b). Nonetheless, the ratio of the underestimated low frequency content and the overestimated high frequency content still predicts the PPA within the measurement uncertainty of the needle hydrophone for all propagation distances.

6.2.4 Discussion

Chapter 5 results demonstrated the role of periodic shockwaves in the emissions generated by a cloud of acoustic cavitation bubbles, and their contribution to the detected subharmonic frequency. The results presented in §6.2 were taken to study detector deconvolution and, quantification of the characteristics of a shockwave emitted. The Gilmore equation was applied to LIB collapse to simulate the pressure waveform.

The results demonstrate that magnitude-only deconvolution has a significant influence on the spectrum of a single BCSW. To perform a quantitative analysis on the subharmonic spectral peak and those of its over harmonics, from cavitation spectra with periodic shockwave content, it is necessary to use a detecting device that is calibrated for magnitude response, over an appropriate bandwidth. This extends to the use of passive cavitation devices, particularly broadband PVdF-based detectors, where shockwave detection may be expected to constitute a significant proportion of the signal collected. This would go some way to facilitating direct comparison of the cavitation spectra presented during different studies from different research groups, which is an issue in current literature. Moreover, quantitative analysis of cavitation emissions that contains shockwave components, in the time domain, can only be meaningfully implemented with full waveform deconvolution, with magnitude and phase calibration data over an appropriate bandwidth.

This extends to techniques being developed for real time and spatial monitoring of cavitation activity, such as passive acoustic mapping (Gyöngy and Coussios, 2010b, Jones et al., 2013) during the application of therapeutic ultrasound. Appropriate

calibration of the array elements used would allow more meaningful interpretation of cavitation activity.

All bubble collapse shockwave generation models (Shaw and Spelt, 2010) in the literature predict purely compressive shockwave profiles. BCSW propagation, however, is not so well studied and many reports present measurements, taken with a range of detecting devices, which include an apparent trailing negative phase. Shockwaves generally, such as those resulting from a detonation or used for lithotripsy, are known to develop a tensile phase following the initial impulsive compression, attributed at least in part to medium response to the propagating compression. The results presented in this section confirm that this is not the case, at least for BCSWs from a collapsing laser-induced bubble formed in water, and that the reported apparent negative phases are detector convolution artefacts, such as those in fig. 6.9 (a).

The spectrum of the magnitude-only, and consequently the full waveform deconvolved BCSW hydrophone data, in fig. 6.10 (b), indicate that the power decreases linearly with increasing frequency. It is possible that higher frequencies may be under represented in the spectrum due to the directivity of the needle hydrophone, which will be narrower for higher frequencies. This complex function (Radulescu et al., 2003) indicates that the higher frequencies in a shockwave will be more sensitive to any misalignments in the hydrophone orientation, with respect to the bubble location. This may shift the shape of the deconvolved BCSW spectrum into closer alignment to the simulated shockwave spectrum, by a few dB. Moreover, it may be expected that experimental attenuation of higher frequencies, particularly during early propagation of

the BCSW from the bubble, would shift the shape of the simulated BCSW spectrum closer to that of the measured one, across the higher frequencies.

However, it is clear that the majority of the BCSW power is contained in the lower frequency region of the spectrum, with the magnitude falling below -10 dB at 5 MHz, fig 6.10 (b). This suggests that designing detectors to maximise sensitivity at lower frequencies is a valid concept, if detecting PSWs and subharmonic signals from acoustic cavitation is desired.

Possible improvements to this work include extending the calibration bandwidth of the needle hydrophone, currently limited to what is commercially available, and more rigorous simulation of the BCSW generation and propagation. Accounting for factors such as gas content, heat and mass transfer in the bubble oscillation model would influence the collapse dynamic. Moreover there are advanced shockwave generation models (Shaw and Spelt, 2010), which account for compressibility of the medium through which the shockwave is propagating, for example. Implementing a more refined BCSW simulation may deliver better spectral matches to those measured experimentally with a wider calibration bandwidth. However, for the purposes of investigating the effects of deconvolution on cavitation bubble shockwaves, and providing insight into how they may be treated with the appropriate hydrophone calibration, the results presented suggest the approaches adopted are adequate.

6.2.5 Conclusion

Single-frequency calibration of experimentally detected BCSWs delivers profiles with notable differences to simulation predictions, generated via a bubble collapse and

simple acoustic emission model. Magnitude-only deconvolution, in comparison to appropriately filtered simulation profiles, improves the PPA estimate of the experimental measurement, but the waveform in the time domain retains phase distortion. Full waveform deconvolution provides the best match between the experimentally measured and filtered simulation data, removing the non-flat detector response within the calibration bandwidth; most notably the apparent negative phase.

6.3 Optical breakdown shockwave generation model

The previous results section introduced full waveform deconvolution as the method to reconstruct the BCSW, the following discussion will introduce the Church equation to simulate the OBSW, which will be compared to needle data positioned ~ 70 mm from nucleation.

To approximate the principle characteristics of an OBSW, for inputting to the Finite Element (FE) model PZFlex, described in §7.1.5, Eq. (6.9) was used. This follows a formulation presented by (Church, 1989) commonly used to model lithotripsy shockwaves (Leighton et al., 2013).

$$P_{SW} = \left(1 - e^{-\beta t}\right) P_A e^{-\alpha t} \quad , t \geq 0 \tag{6.9}$$

Where P_A is the peak positive pressure amplitude, α and β are constants controlling the RT and the FWHM of the shockwave. The constants α and β, were chosen using the following considerations. The RT of an OBSW, generated with similar pulsed-laser parameters to those used here, is in the order of ~ 6 ns (Vogel et al., 1996), and the FWHM measured by the needle at ~ 70 mm, was ~ 48 ns. Hence, α = 16.198 $\times 10^6$ and β = 921 ×

10^6 were chosen to satisfy respective considerations. This simulated shockwave was bandpass filtered according to the needle calibration, 125 kHz to 20 MHz. The resulting shockwave (red dashed) is shown in fig. 6.12. (a) which is normalised to the full waveform deconvolved needle signal (blue line) for comparison. The frequency spectra of the full waveform deconvolved OBSW and simulated shockwave, fig. 6.12 (b).

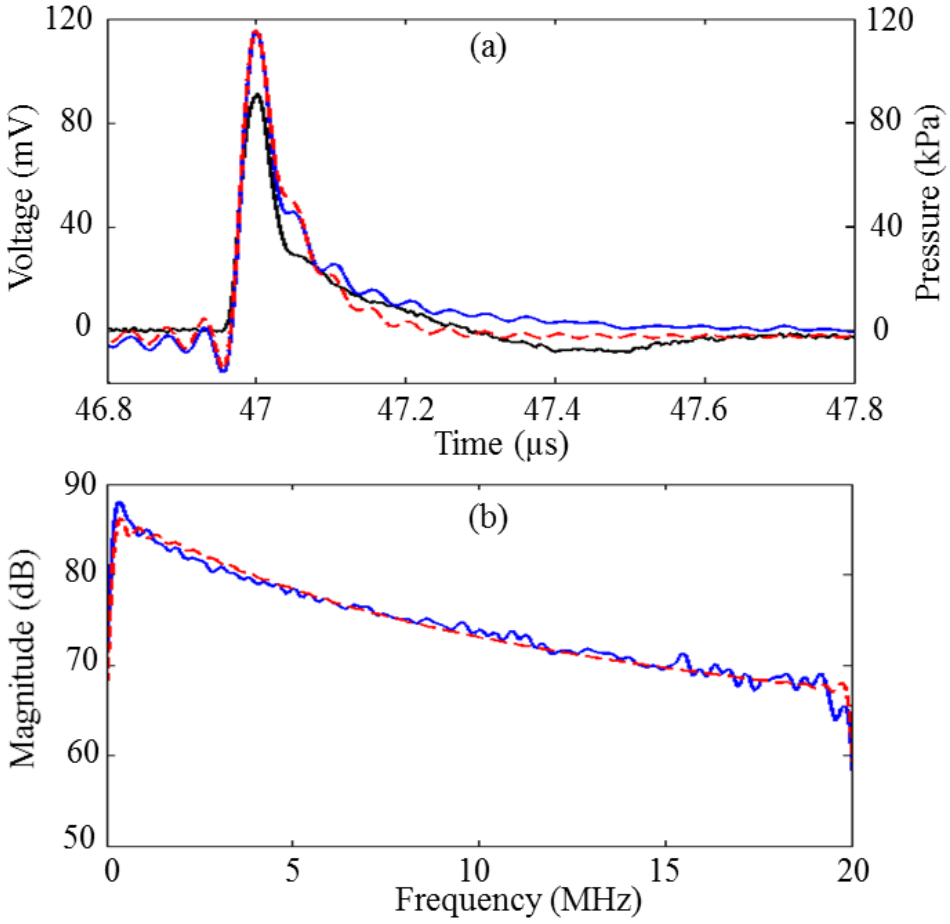

Figure 6.12. Full waveform deconvolution of needle signal from OBSW, simulated shockwave and corresponding frequency spectra. (a) Needle voltage signal (black line) and corresponding full waveform deconvolved pressure (blue line) over the calibrated bandwidth 125 kHz – 20 MHz. Also the simulated OBSW using Church equation (red dashed), band pass filtered from 125 kHz - 20 MHz (b) FFT of deconvolved needle data and simulated OBSW at 70 mm.

In the case of finite element modelling using PZFlex, it is important to setup the model to support all frequencies that are contained within the simulated input function. A shockwave contains energy over a broadband frequency range, therefore low pass filtering the simulated input, limits the requirement for a high spec computer and decreases simulation time without decreasing the accuracy of the simulation (see §7.1.5)

6.4 Deconvolution of periodic shockwaves using needle hydrophone

The real motivation for the investigation into detector deconvolution described above, was the assessment of the effects of detecting PSWs from acoustically driven clouds. Laser nucleated acoustic cavitation measurements were therefore subsequently undertaken by positioning the needle orthogonally to the HIFU axis, ~ 70 mm from nucleation[11] site, and imaged at 1 Mfps. Fig. 6.13 (a) are sample high-speed images of a single LNAC cloud, driven by the Sonic Concepts transducer, and parallel needle hydrophone detection of the activity, fig. 6.13 (b) (next page).

[11] Note: 70 mm is the focal length of Sonic Concepts PCD. Therefore, all LNAC data were positioned at ~ 70 mm for comparison of shockwaves detected by needle, Sonic Concepts and shockwave PCD. This will be discussed in Chapter 7.

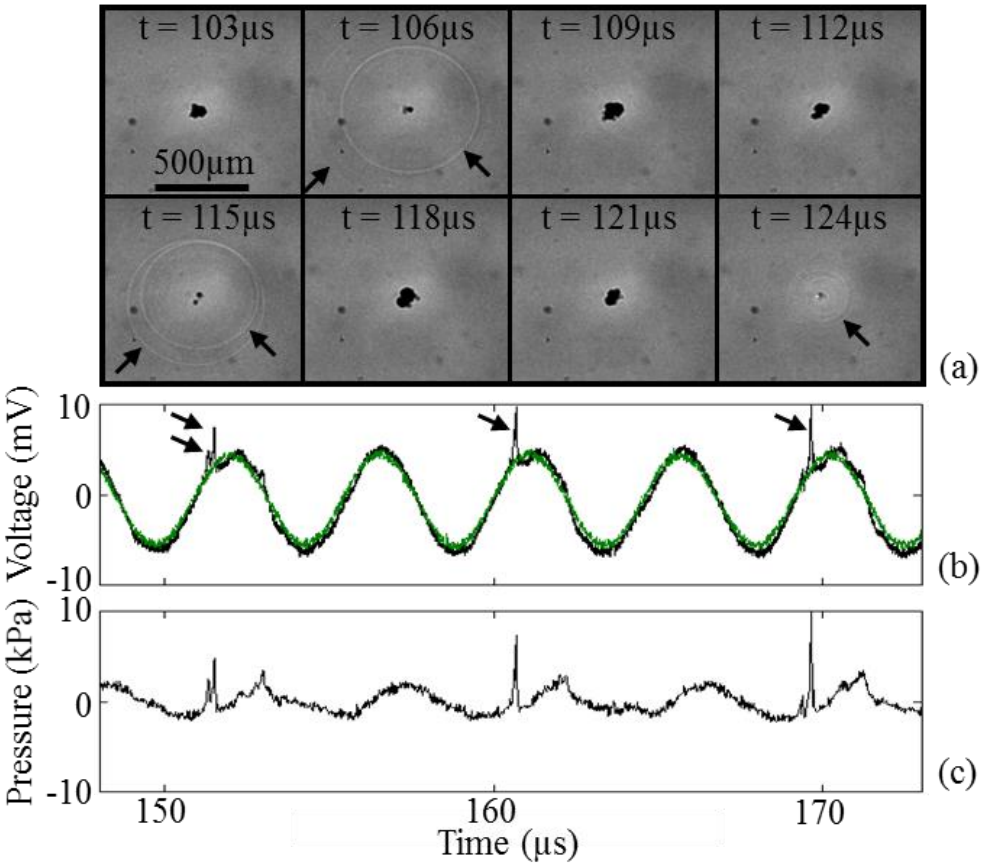

Figure 6.13. LNAC periodic shockwaves detected using needle hydrophone. (a) Images extracted from a high-speed sequence, captured at 1 Mfps, revealing periodic shock-emission at the subharmonic, $f_0/2$. **(b)** Needle hydrophone voltage output (black) recorded from the cavitation activity represented by (a), ~ 70 mm from laser focus, corresponding to a propagation delay of ~ 47 µs, from when a shockwave is emitted by the cloud, and detected by the needle hydrophone. A control exposure, for which the HIFU burst is generated but the nucleating laser-pulse is blocked is also presented (green). (c) Needle hydrophone control (green) is subtracted from experimental (black) and this voltage signal is fully deconvolved over calibrated bandwidth 125 kHz – 20 MHz to reveal low PPA PSWs.

Fig. 6.13 (a) demonstrates a cloud of bubbles collapsing, coincidentally emitting shockwaves at 106, 115 and 124 µs, at a shock-period of ~ 9 µs, consistent with PSW-emission at $f_0/2$, the half-harmonic, driven at 1.05 MPa peak negative pressure (PNP) (calibrated using needle at the focus of HIFU transducer, using full waveform deconvolution). The needle hydrophone data features the acoustic detection of the

shockwaves captured by the imaging (arrowed black for both data representations), with a propagation delay of ~ 47 µs, consistent with the speed of sound in water, although a short duration of supersonic propagation may be assumed (Brujan et al., 2012).

Full waveform deconvolution of the needle voltage signal (black), following the process outlined in §6.2.6 over the calibration bandwidth of 125 kHz – 20 MHz, and subtracting the control (green) fig 6.13 (b), indicates that the PSWs emitted by the cloud have PPA's in the range of ~ 3 – 10 kPa, at 70mm, fig. 6.13 (c). The high-speed imaging of fig. 6.13 (a) further reveals multi-fronted shockwaves emitted by acoustic cavitation clouds, as they tend to collapse non-uniformly. The acoustically detected shockwave at ~ 152 µs, fig. 6.13 (b), indicates that in this case, the needle hydrophone has resolved two peaks, according to the two shock-fronts emitted at 106 µs (arrowed). The features at ~ 161 and 169.5 µs are less clearly resolved, consistent with the closer spacing between the fronts, captured by the high-speed imaging at 115 and 124 µs, respectively. These low PPA's, relative to the HIFU driving or other types of shockwaves, such as those generated for lithotripsy therapy of kidney stones (Leighton and Cleveland, 2010) for example, justifies the development and optimisation of a PCD with the intention of detecting cavitation cloud shockwaves with as high a sensitivity as possible. This is the goal of the work described in Chapter 7.

7 Optimisation of a single element passive cavitation detector for the subharmonic signal

Deconvolution of the needle hydrophone data in the previous Chapter indicated that periodic shockwaves (PSWs) emitted by acoustic cavitation, measured at 70 mm are relatively low 10's of kPa. As previously demonstrated in Chapter 5, the subharmonic is a shockwave-mediated signal, which is exclusive to cavitation activity and commonly used to indicate the presence of cavitation in HIFU. Therefore, it would seems progressive to design a passive cavitation device (PCD), sensitive to shockwaves, in the aim of increasing detection of the subharmonic signal.

This Chapter is focused on giving a detailed account of the design, build and testing of a simple and economical single element PCD, primarily optimised for detection of low frequency components in shockwaves. Finite element software, PZFlex, is used to guide the selection of backing and matching layers, at each stage of PCD construction. Moreover, the sensitivity of the PCD at low frequency components is shown to far exceed that of two commonly used commercial detectors, also tested *in-situ* and this result is supported by a magnitude calibration of PCD. The final results[12] will demonstrate the

[12] The results presented in this chapter are currently under preparation for submission to Sensors (Johnston, K. Song, J. Johansen, K. Prentice, P. 2016. Optimisation of a Single Element Passive Cavitation Detector for the Subharmonic Signal, Sensors).

detection of PSWs from a cavitation cloud, such as those featured in Chapter 5, by the shockwave PCD (swPCD) versus the commercial detectors.

However, first a description of the Sonic Concepts PCD and swPCD will be given along with some materials and methods relating to the experimental setup.

7.1 Material and Methods

7.1.1 The commercial acoustic detectors

All experiments were conducted using sonoptic chamber V.2, as described in §6.1.2 using two commercial detectors for comparison during the development of the swPCD; the needle hydrophone (Precision Acoustics, magnitude and phase calibrated by NPL, as described in §6.1.3) and a spherically focused hydrophone (Sonic Concepts, Y107) which has a stated application as a PCD.

The Sonic Concepts PCD was designed to fit into the central 20 mm opening of the HIFU source (see §6.1.1, fig. 6.3.) using a rubber o-ring retainer. The Sonic Concepts PCD has a 17.5 mm active diameter and is confocal to the focus of the HIFU field for heightened sensitivity, with a stated bandwidth of 10 kHz – 15 MHz. Its construction, provided by Sonic Concepts, Inc. on request, is described as a "*0.2 mm thick piezo-polymer stack, with high acoustic impedance backing material > 4 MRayl and an EMI shielded plastic outer casing (20 mm OD x 40 mm length) to optimize the operating bandwidth and signal-to-noise ratios".*

7.1.2 Description of shockwave PCD design

The swPCD is designed to be interchangeable with the Sonic Concepts PCD, within the HIFU transducer for testing purposes and has a 15 mm diameter active area, which was stamped using a punch from a sheet of 110 μm PVdF film, with silver ink electrode

metallization (measurement Specialties™). The ground electrode of an 80cm RG174-U coaxial cable (rs-online) was bonded to the positively poled front face of the film using silver conductive epoxy (Agar Scientific) and the outer casing (20mm OD x 16 mm length) was rapid prototyped (MakerBot™ Replicator 2X) using acrylonitrile butadiene styrene (ABS) filament material, fig. 7.1.

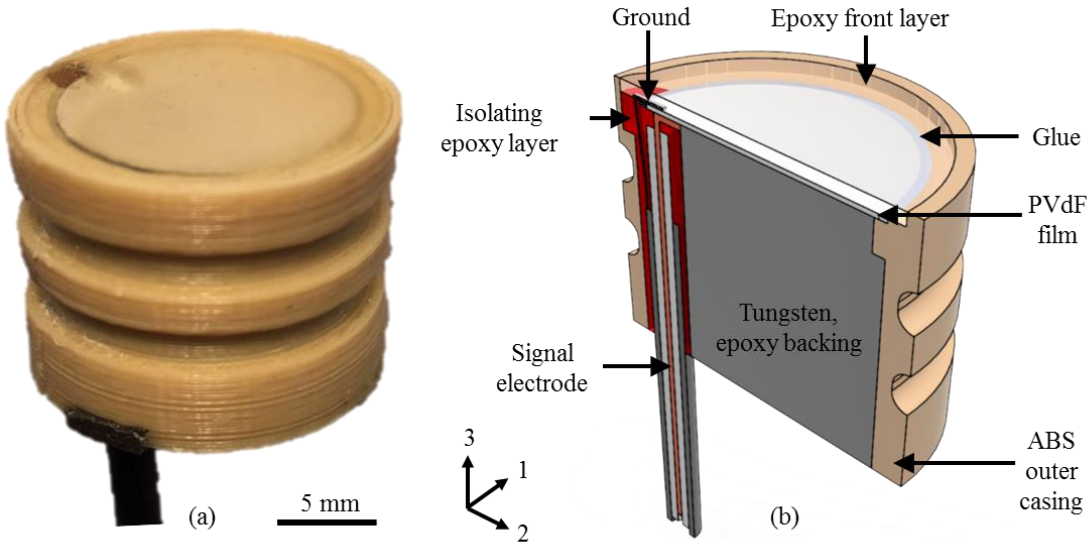

Figure 7.1. (a) Photograph of the final stage swPCD device, and (b) section-view schematic illustrating the component structure.

The casing included a *c* shaped channel, which secured the coaxial cable using epoxy (Araldite), which also isolated the signal and ground electrodes to prevent a short circuit. A bead of glue (Loctite 401) was applied around the circumference of the PVdF film to bond it to the casing and a tungsten (12µm Sigma-Aldrich) / epoxy (CY221 / HY956 resins-online) backing material (§7.1.6) was added. The outer casing design ensured the correct amount of backing material (15 mm) and front ~ 0.9 mm epoxy matching layer (§7.1.6, CY221 / HY956 resins-online) was added, thus enclosing the

PVdF film and protecting the active area. After curing, the front surface was wet sanded using 1000 grit wet and dry paper, to ensure a flat planar surface of the correct thickness.

7.1.3 Experimental setup

Both commercial detectors and the swPCD were present, in one of two configurations as depicted in Fig. 7.2 (b) or (c) (next page) depending on the measurement being undertaken. Fig. 7.2 (b) is the experimental setup for detecting PSWs from laser nucleated acoustic cavitation (LNAC, see §3.3). All PCDs are positioned ~ 70 mm from the pulsed-laser focus, because this was the focal length of the Sonic Concepts PCD. The variability of PPA from LNAC clouds PSWs (see fig. 6.13) meant the more reliable and reproducible shockwaves generated during the formation of a laser-induced bubble (LIB) were used to compare swPCD performance against the commercial detectors. The swPCD performance is primarily evaluated against the Sonic Concepts device, because it has a stated application as a PCD and has been used for cavitation experiments (Hallow et al., 2006, Prokop et al., 2007).

Fig 7.2 (c) is the experimental setup for all the testing of the swPCD from the optical breakdown shockwave (OBSW) and bubble collapse shockwave (BCSW) emitted from the collapse of a LIB.

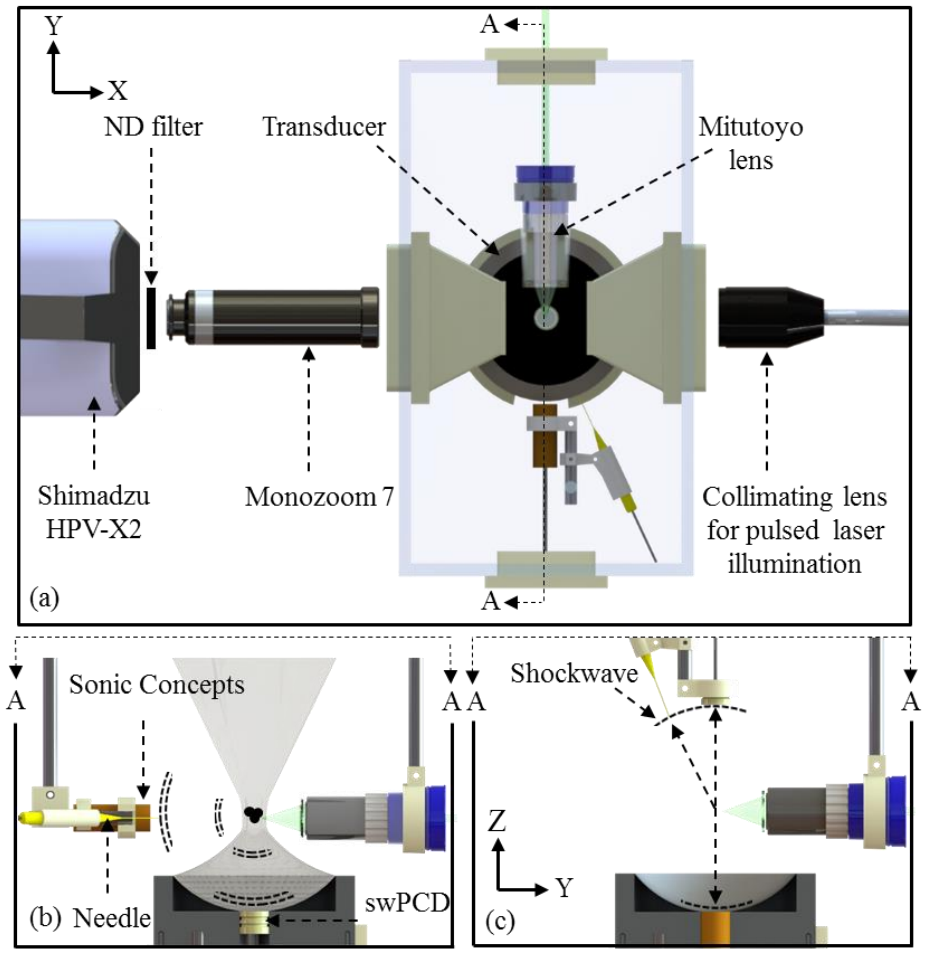

Figure 7.2. (a) Top view of the sonoptic test chamber, including high-speed camera and pulsed laser illumination configuration; (b, c) Section views of the hybrid pulsed laser-HIFU arrangement. (b) laser-nucleation of acoustic cavitation, with the swPCD located inside the central hole of the HIFU transducer, the Sonic Concepts PCD and needle hydrophone located perpendicular to the HIFU propagation axis, at 70mm from confocal point; and for **(c)** the OBSW-based testing of the swPCD, throughout the various stages of development. The needle hydrophone and Sonic Concepts PCD positions, during OBSW testing are also depicted.

The swPCD was tested in three sequential stages of construction 1) PVdF film only, 2) adding a backing material and 3) adding a matching layer (subsequently referred to as stages 1, 2 and 3). The role of the needle hydrophone was primarily used as a reference hydrophone to characterize the properties, including full width half maximum (FWHM) of the various shockwaves used, and to ensure that the swPCD was tested against shockwaves of comparable PPA. The needle was also used to perform a magnitude

calibration of both the swPCD and the Sonic Concepts PCD, within the calibration bandwidth. All data is, however, presented in voltage convolved with the respective detecting device sensitivity. This is to facilitate a direct comparison between each of the swPCD developmental stages, and to distinguish the differences between the needle hydrophone and Sonic Concepts PCD measurements. Moreover, representation of the detected signals in the voltage-time domain will be of more use to anyone seeking to construct a similar PCD, following the design outlined in this chapter.

7.1.4 High-speed camera imaging

Fig. 7.3 (a) depicts the high-speed imaging of a LIB and corresponding acoustic detection of the OBSW and BCSW (arrowed) by the swPCD, fig. 7.3 (b).

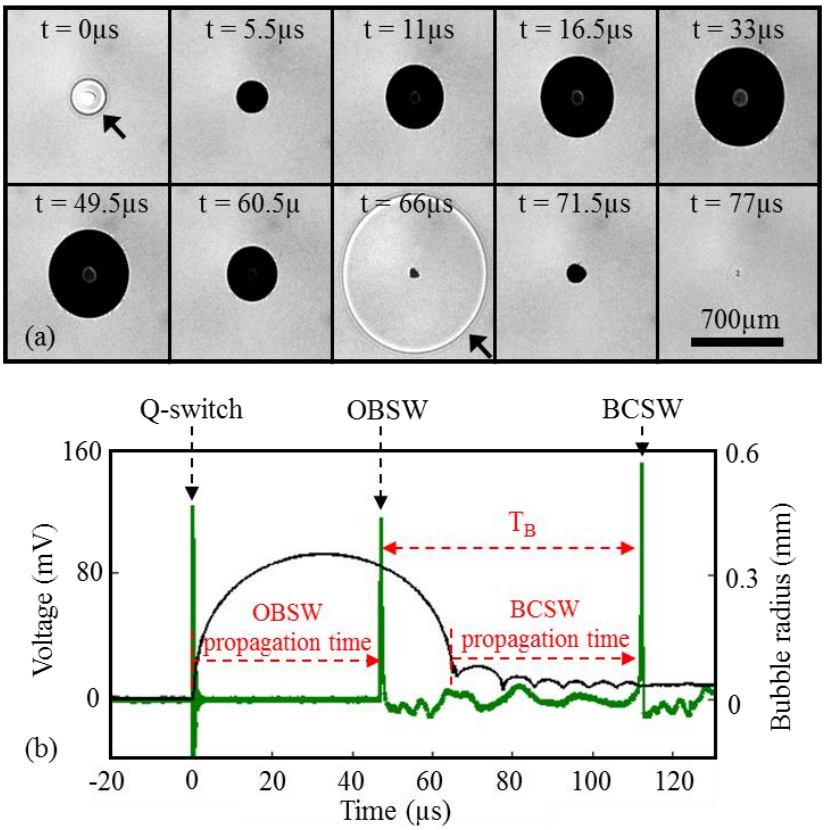

Figure 7.3. (a) Images extracted from a high-speed sequence of a laser-induced bubble (LIB), and corresponding stage 1 swPCD response. (Caption on next page).(a)

High-speed imaging is captured at 2 Mfps, with the optical breakdown shockwave (OBSW) and bubble collapse shockwave (BCSW) arrowed at 0 µs and 66 µs, respectively. (b) Corresponding acoustic data detected by the swPCD at ~70 mm from laser focus, with a ~ 47 µs delay for shockwave propagation, with notable features including the laser Q-switch from the pulsed laser, the OBSW and BCSW. The bubble radius-time curve is also depicted.

The time between the OBSW and BCSW shockwaves can be taken to represent the oscillation period T_B of the primary LIB. It may be observed from fig. 7.3 (b) that the PVdF film of the swPCD (at stage 1 of the construction) vibrates erratically for an extended period of time, following detection of the OBSW. The BCSW detection, ~ 65 µs later, is influenced by those vibrations such that the actual voltage amplitude is difficult to ascertain. Accordingly, the OBSW was used to assess the swPCD sensitivity, as this shockwave is always detected from ambient conditions, or 0 mV. However, the BCSW detection was also simulated in PZFlex and included in the results for completeness of the experimental data.

For swPCD testing against OBSWs the detectors are arranged according to the configuration depicted in fig. 7.2 (c). In this orientation, the swPCD and needle hydrophone detect a significant reflected shockwave, from the HIFU transducer located below the pulsed-laser focus. These reflection signals are easily identifiable in the voltage recordings, and are subsequently disregarded.

7.1.5 Finite element model (PZFlex) for swPCD optimisation

PZFlex is a high fidelity Finite Element (FE) Analysis software that specializes in wave propagation and piezoelectric problems for virtual prototyping. A FE-model was generated to guide the development of the swPCD, using the backing and matching materials listed in the database (see §7.1.6), with the aim of optimising the PCD for

maximum sensitivity to low frequencies components from an incident shockwave. A 2D axisymmetric representation of the FE-model is seen in fig. 7.4.

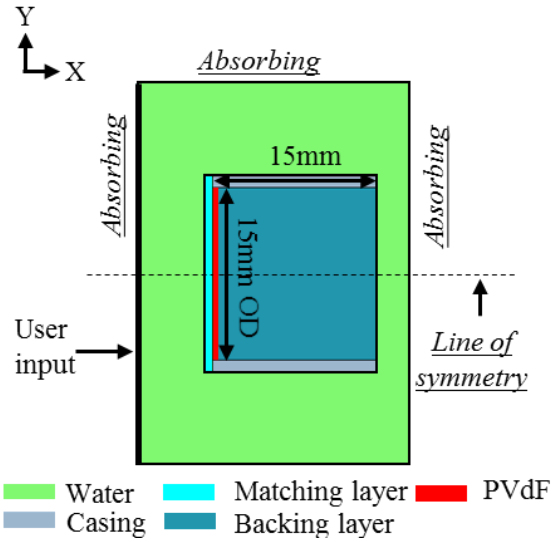

Figure 7.4. Shockwave FE-model setup for a swPCD stage 3 simulation. including line of symmetry, boundary conditions and piezoelectric poling directions. A user-defined input may be applied to y-plane, as indicated.

Rotational symmetry was applied around the line of symmetry to achieve a 3D representation of the problem. To approximate an input to simulate the OBSW, the Church equation Eq. (6.9) was used, previously described in §6.3 and the Gilmore equation Eq. (6.1) to model a bubble collapse and emission, described in §6.2.2. Chapter 6 also demonstrated the majority of energy for a BCSW, fig. 6.10 and OBSW, fig.6.12 is contained within the low frequency part of the spectrum for both shockwaves, consequently, the inputs to the FE-model were low pass filtered at 40 MHz, also limiting the computational demands required for a simulation. The low pass filtering can be further justified as the primary interest is in the response to the low frequency components. To ensure the low pass filtering did not distort the FE-modeling of the detector, a series of simulations were carried out increasing the mesh size, at 40 MHz, 50 MHz, and 60 MHz

using 15 elements per wavelength, which demonstrated convergence at 40 MHz. Fig. 7.5. Illustrates the FE-model in action, and the voltage response from a stage 3 swPCD that has both a matching and backing layer.

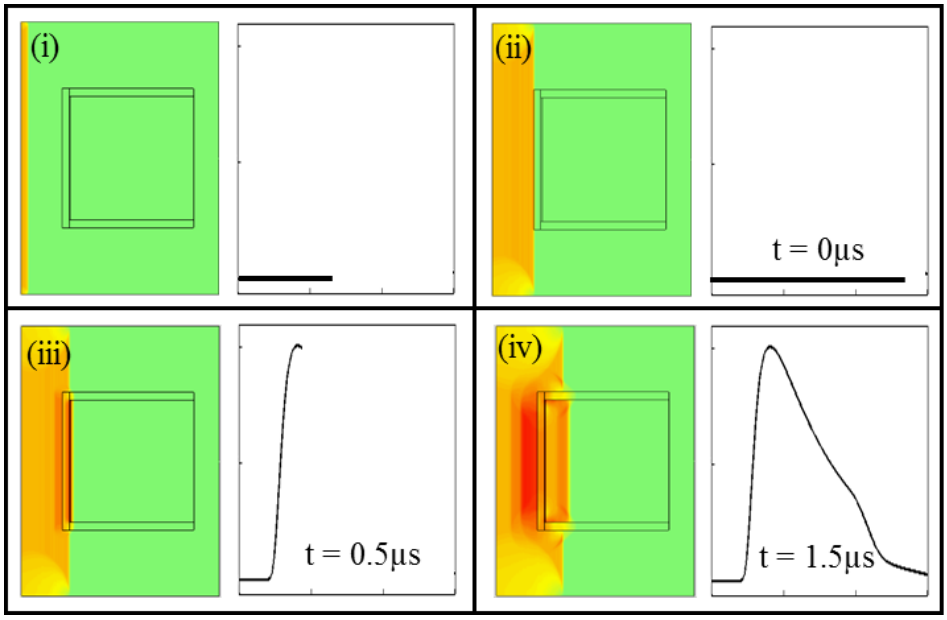

Figure 7.5. Stage 3 swPCD FE-simulation of and corresponding voltage response. (i) User defined shockwave propagating as a plane wave toward the PCD active area (ii) Leading edge of shockwave impacts front epoxy layer and (iii) shockwave propagates into matching material, causing an initial voltage response (iv) Complete sensor response: All of shockwave moved into backing material and or has been reflected back into the matching layer.

7.1.6 Backing and matching materials

The backing and matching materials listed in Table 7.1 and 7.2 are taken from the PZFlex database, which have been previously characterised by the Centre for Ultrasonic Engineering, University of Strathclyde. All material properties stated in the following sections were measured at 1 MHz. As stated previously, shockwaves are broadband signals, with magnitude components across a wide range of frequencies. However, characterisation at 1 MHz was assumed satisfactory, for the purposes of validating the swPCD performance. The primary role of FE-simulation is to allow a relative comparison

of the performance of various backing and matching materials and to guide the construction of the swPCD. However, when comparing FE-simulation results to experimental results, the absolute voltage were not useful, therefore all data is normalised to material that had the best magnitude response.

Table 7.1. Potential backing materials listed in PZFlex database and PVdF film. The reflection co-efficient (*R*) as a percentage, was calculated according to Eq. (4.1) using the impedance of PVdF film and the different backing materials listed.

No	Material Name	Density (Kgm^{-3})	longitudinal Velocity (ms^{-1})	Impedance (MRayl)	*R %*
1	Air	1.24	343	0.000425	99
2	Water	1000	1496	1.496	25
3	PVdF	1780	2560	4.56	0
4	Vantico HY956EN/CY221	1134	2452	2.78	9
5	5%vf tungsten/epoxy	2063	2250	4.641	2
6	25%vf tungsten/epoxy	5710	1750	9.99	14

Table 7.2. Potential matching materials selected from PZFlex material database. The transmission coefficient (*T*) was calculated as a percentage according to Eq. (4.2) at the boundary between the matching layer and PVdF film.

No	Material Name	Density (Kgm^{-3})	longitudinal Velocity (ms^{-1})	Impedance (MRayl)	*T %*
1	Water	1000	1496	1.496	64
2	Vantico HY956EN/CY208	1165	1989	2.31	89
3	Vantico HY956EN/CY221	1134	2452	2.78	94
4	Stycast 1269A	1190	2416	2.87	94

7.2 Results

7.2.1 FE-backing layer simulations

The backing materials selected in Table 7.1, §7.16 are used for comparison to a stage 1 PVdF film only, the results for the FE-simulation for both OBSW and BCSW are displayed in fig. 7.6 (a, b).

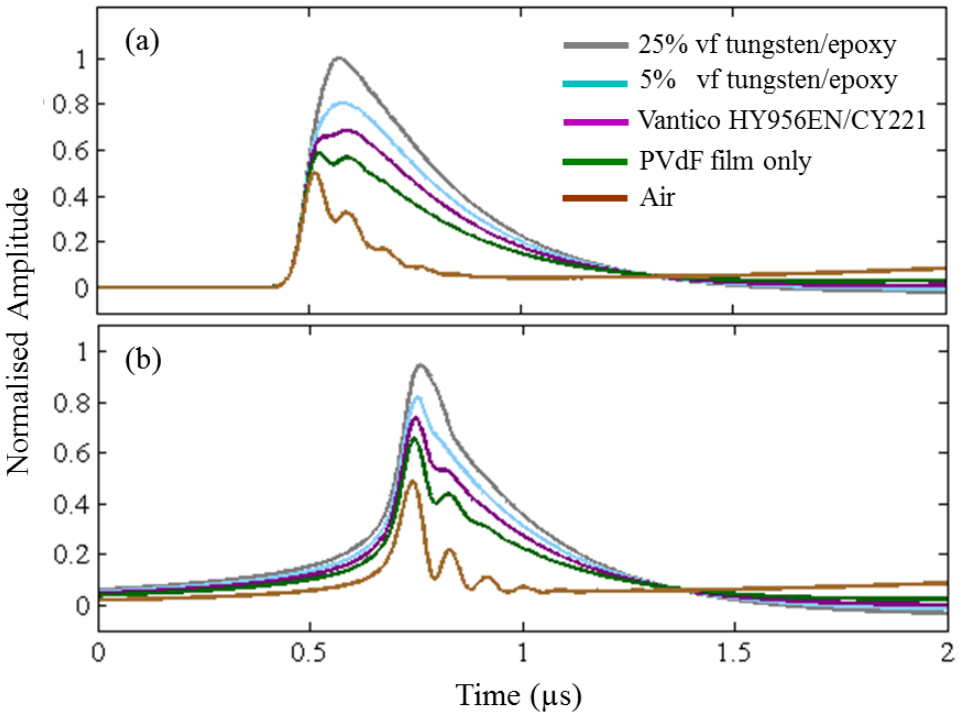

Figure 7.6. FE-simulations of swPCD response from an OBSW (a) and BCSW (b) for various backing materials. All FE-simulations are carried out using a backing thickness of 15 mm.

Fig. 7.6. indicates that the addition of backing materials Vantico HY956EN/CY221, 5%vf tungsten/epoxy and 25% tungsten/epoxy increased sensitivity, when compared to stage 1, PVdF film only. An air backing decreased sensitivity, possibly due to the large impedance difference, which resulted in a reflected component of 99% of that incident, calculated using Eq. (4.1), from the PVdF film-air interface. Comparing fig 7.6 (a) and (b) further indicates that the influence of the backing material on the voltage output is

equivalent for both shockwave types (OBSW and BCSW). The impedance of the 5%vf tungsten/epoxy which has the closest match to PVdF film, 4.65, and 4.56 MRayl respectively, results in a 2 % reflected component, but FE-simulations indicate 25%vf tungsten/epoxy had the maximum sensitivity, although the impedance difference is greater, 9.9 compared to 4.56 MRayl and the reflected component increased to 14%. As previously discussed in §4.1.1.2 the addition of a backing layer effectively changes a PVdF film hydrophone response from hydrostatic to thickness mode, which increases voltage output. However, the relative increase of 1.18x, from 5% to 25% vf, cannot readily be explained. It is suggested the addition of a more dense backing layer, of 5710 Kgm^{-3} compared to 2063 Kgm^{-3} for 5% vf tungsten/epoxy acts a firmer surface to a shockwave incident to the active area, which further activates the thickness mode, creating a greater voltage output, but this is purely conjecture. The greatest sensitivity was achieved by 25% vf tungsten/epoxy backing layer, thus it was selected for device construction and testing.

7.2.2 FE-matching layer simulation

Although the difference in acoustic impedance between water and PVdF is relatively small (3 MRayl), introducing a matching layer may further improve the performance of the swPCD, specifically targeting an increased transmission coefficient for the low frequency content in the shockwave. The matching layer also provides protection to the PVdF film and electrodes, which is as important a role for the layer as any enhancement of sensitivity. Potential matching material are stated in Table 7.2, §7.16 were selected by using Eq. (4.9), which indicated selecting a matching material with an

impedance of 2.59 MRayl. The FE-simulation of various matching layers in comparison to no matching layer, for both OBSW and BCSW is shown in fig. 7.7 (a, b).

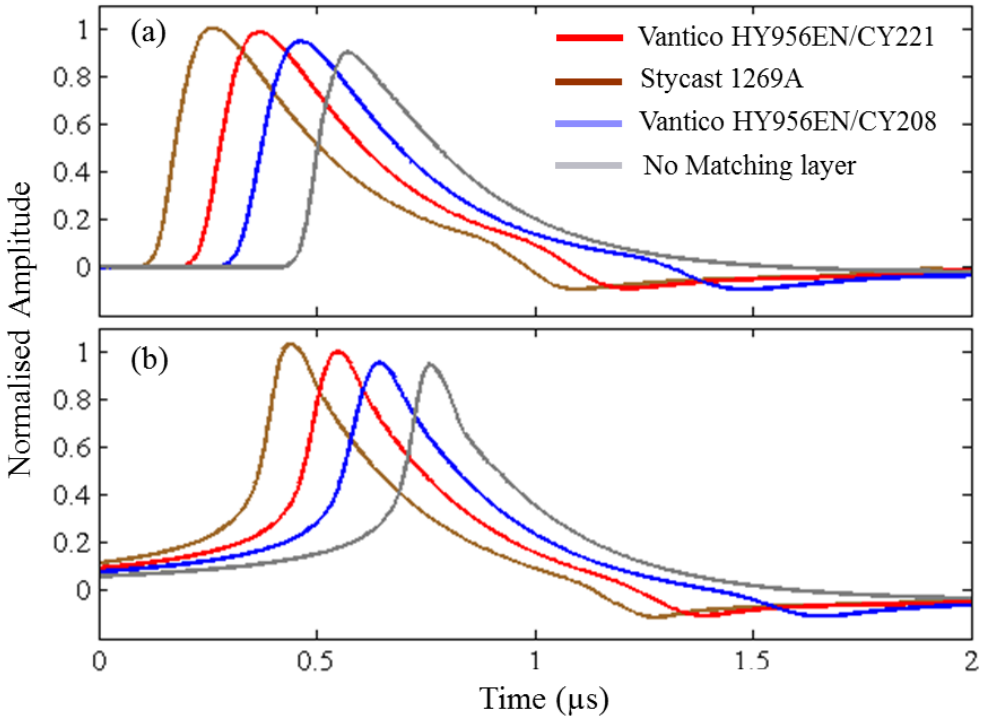

Figure 7.7. FE-simulations of (a) OBSW and (b) BCSW response using different matching materials. listed in Table 7.2. All potential matching materials are simulated using a matching thickness of 0.9 mm.

Fig. 7.7 (a) indicates that by adding a matching materials increased sensitivity by ~5% for Vantico HY596EN/CY208 and ~10% for both, Stycast 1269A, Vantico HY956/CY221 when compared to no matching layer. The addition of a matching layer increased the transmission coefficient calculated using Eq.(4.2) at the matching layer / PVdF film boundaries from 65% for no matching layer (water) to 89% for Vantico HY596EN/CY208 and 94% for both Stycast 1269A and Vantico HY956/CY221. As the swPCD is being optimised to maximise sensitivity to the low frequency component of a shockwave, and an optimal thickness of the matching layer cannot be determined

antically, FE-simulations suggest a thickness of 0.9 mm, limiting the effect from attenuation and selecting a material, whose impedance is close to perfect matching, maximises peak voltage for both OSBW and BCSW. Therefore, Vantico HY56EN/CY221 was selected for experimental testing because it has the closest impedance to the required 2.59 MRayl, but FE-simulations suggest Stycast 1269A, could also be used as a matching material.

7.2.3 swPCD construction stages

Experimental testing from stage 1-3 swPCD from an OBSW, BCSW and PZFlex simulations are compared in fig. 7.8 (a, b).

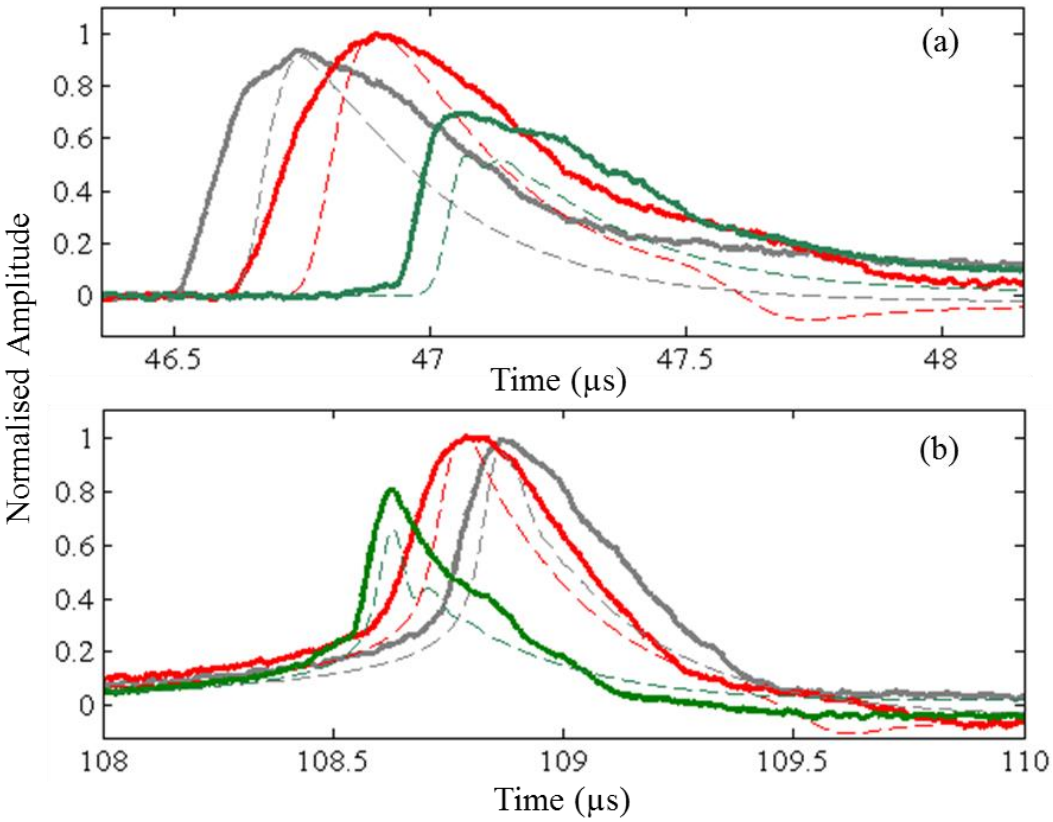

Figure 7.8. Experimental (a) OBSW and (b) BCSW stage 1-3 swPCD comparison and corresponding FE-simulations (dashed line). (a) OBSW comparison for stage 1, PVdF film only (green), stage 2, backing layer (grey) and stage 3, matching layer (red). (b) BCSW comparison. Both experimental and FE-simulation are normalised for comparison to stage 3 matching layer.

Table 7.3. Experimental and FE-simulation comparison for stage 1-3 PCD.

Stage no	swPCD	Normalised Amplitude Exp / FE-sim	FWHM (ns) Exp / FE-sim
1	PVdF film only	0.69 / 0.53	510 / 332
2	Backing	0.94 / 0.91	541 / 346
3	Matching	1	545 / 344

The maximum voltage and full width half maximum (FWHM) for the OBSW data presented in fig. 7.8 (a) is extracted for comparison in Table 7.3. The addition of a backing layer in comparison to PVdF film only increased[13] the experimental / FE-simulation ratio amplitudes by 1.36x and 1.71x respectively. The ratio increase of the addition of a matching layer, compared to no matching layer for experimental / FE-simulated amplitudes is 1.06 / 1.09. The temporal shape of the experimental waveforms for both OBSW and BSCW to FE-simulations for stage 1-3 is comparable but a notable difference in FWHM, the FE-simulated is less by 178, 195 and 201 ns for stage 1, 2 and 3, compared to experimental data, Table. 7.3. At 70 mm, the curvature of the shockwave may not be assumed planar to a 15 mm active area, thus the relative differences may be explained by spreading of the shockwave across the element, as it propagates into PCD.

The BCSW, fig. 7.7 (b), indicated the amplitude increase from adding a backing layer for experiment / FE-simulation is 1.23 / 1.46 in comparison to PVdF film only and a 1.01 / 1.05 increase for adding a matching layer when compared to no matching layer. The small 1% difference between experimental matching layer and no matching layer

[13] Note: The data presented in this section is a representative of the experimental increase in comparison to FE-simulation, please see §7.2.4.2 for an overview of all experimental data.

may be explained by the fluctuation in the maximum voltage after OBSW impact, which influenced a true voltage measurement.

7.2.4 Evaluation of the swPCD versus commercial detectors

7.2.4.1 Magnitude calibration

Fig 7.9. demonstrates the frequency response of the sensitivity of stage 3 swPCD, compared to the commercial detectors.

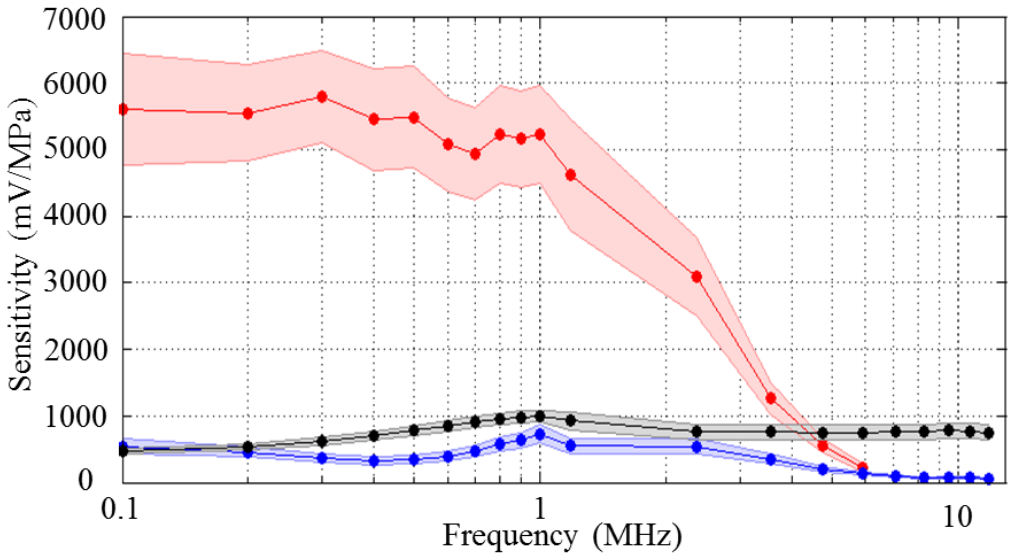

Figure 7.9. Sensitivity vs. Frequency (log scale) of stage 3 swPCD and commercial detectors. The needle hydrophone (black) previously calibrated by NPL was used to determine sensitivity, using the discrete frequency method to calibrate between 0.1 - 1 MHz (Preston et al., 1983), with swPCD (red) and Sonic Concepts PCD (blue) corrected for spatial averaging between 0.5 - 1 MHz (Smith, 1989). The multi-frequency method was used for calibration between 1 - 10 MHz (Smith and Bacon, 1990), See Appendix B.1. Shaded regions indicate uncertainty in the calibration, (Preston et al., 1988, Smith and Bacon, 1990, Ziskin, 2003), which is discussed in Appendix B.2

The method of the calibration is discussed in Appendix B.1 and the origin of the uncertainty in the calibration is detailed in Appendix B.2, fig. 7.9. indicates the relative increase in sensitivity of the stage 3 swPCD (red) at lower frequencies in comparison to both commercial detectors. The swPCD sensitivity from 0.1 - 1 MHz, is an average value

of 5345 mV/MPa ± 15%. with sensitivity decreasing rapidly from 1 – 6 MHz, and no sensitivity above 6 MHz. The Sonic Concepts PCD had the lowest sensitivity of the commercial detectors.

7.2.4.2 OBSW and BCSW

Comparison of shockwave measurements between the three detectors fig. 7.10 (a, b) demonstrates the relative difference between voltage-time waveforms from the stage 3 swPCD and the commercial detectors.

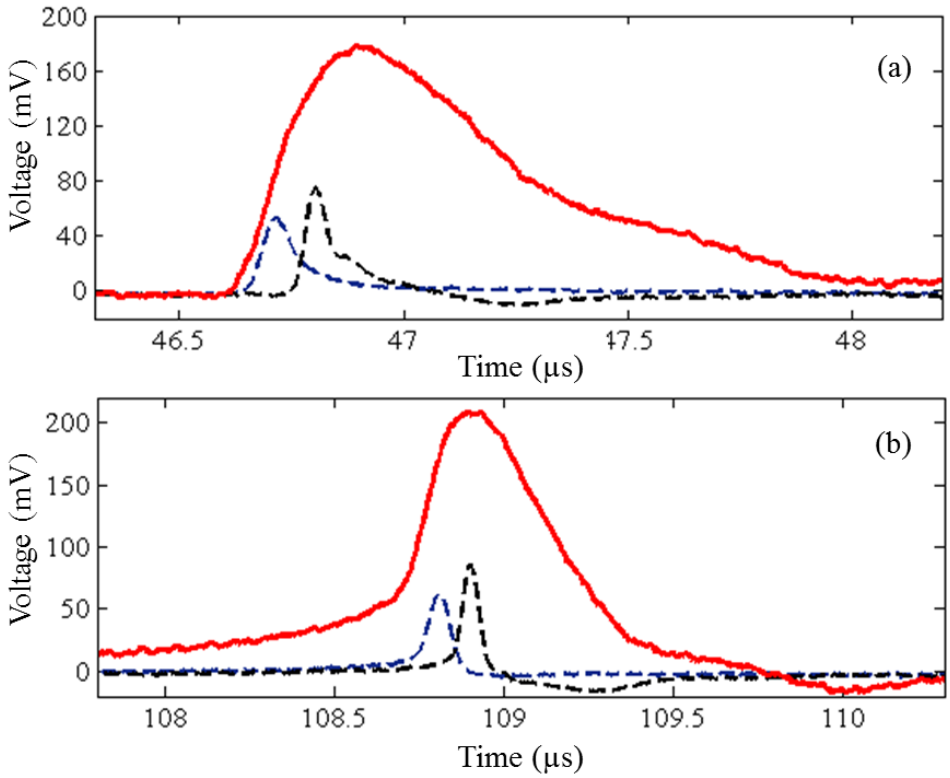

Figure 7.10. Experimental (a) OBSW and (b) BCSW voltage comparison of stage 3 swPCD (red line), needle hydrophone (dashed black) and Sonic Concepts PCD (blue dashed).

Fig. 7.10 (a) it is shown that the swPCD maximum voltage from an OBSW is ~ 2.3x greater than the needle hydrophone and ~ 3.3x greater than the Sonic Concepts PCD. The second most notable difference is the FWHM, measured to be 545 ns for swPCD,

compared to 48 ns needle hydrophone and 68 ns for the (focused) Sonic Concepts PCD. This demonstrates that by increasing the thickness of the PVdF film and adding a backing, matching layer the sensitivity of the swPCD is increased but the temporal resolution is reduced. As the overall goal for the swPCD was to maximise sensitivity, this is an acceptable trade-off.

The relative differences from a range of different sized LIB and the maximum voltage from an OBSW is compared for swPCD stages 1-3 and commercial detectors, fig. 7.11.

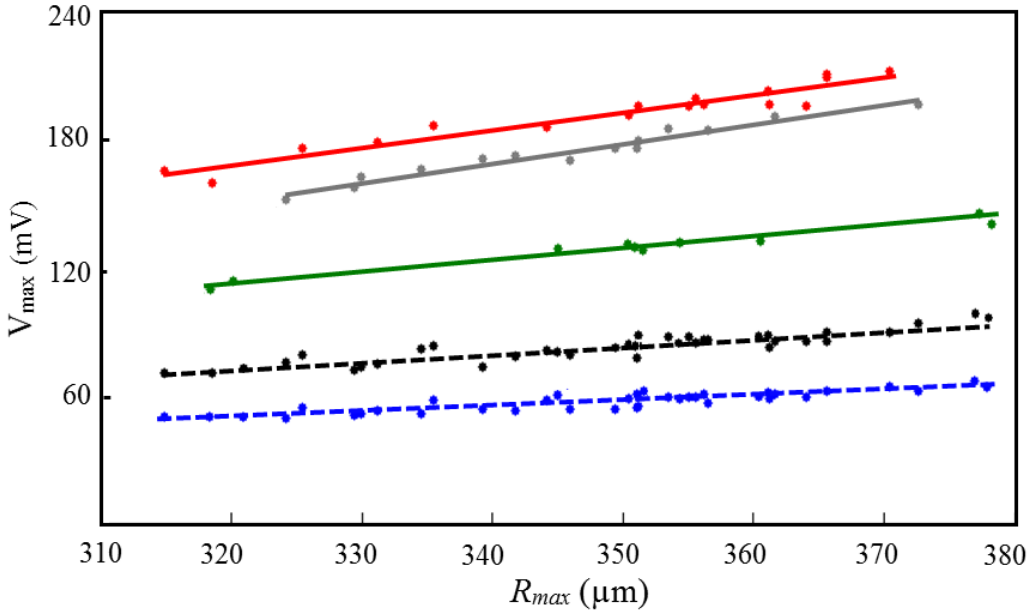

Figure 7.11. Comparison of OBSW maximum voltage vs. maximum bubble radius for different construction stages and commercial detectors Stage 1. PVdF film only (green), stage 2. backing layer (grey) and stage 3. matching layer (red), needle hydrophone (black dash) and Sonic Concepts PCD (blue dash).

A variation of the pulsed laser energy, leads to a variation of the energy absorbed into the medium and results in differently sixed R_{max} (Noack et al., 1998). As the maximum radius of the LIB increases, maximum voltage increased for both stage 1-3

swPCD and commercial detectors. The needle hydrophone (dash black) has the greatest sensitivity to a OBSW compared to the Sonic Concepts PCD (dashed blue). The relative increase in voltage amplitudes resulting from the addition of a backing layer, compared to PVdF film only, is demonstrated and also by adding a matching layer compared to just a backing layer. The data from fig. 7.11. is extracted in Table 7.4.

Table 7.4 Comparison of maximum voltage *vs.* maximum radius of OBSW.

PCD	N	V_{max} (mV) ± SD	R_{max} (µm) ± SD
Needle	40	85.2 ± 9.0	349.8 ± 15
Sonic Concept	40	57.4 ± 4.4	349.8 ± 15
PVdF film only	9	131.4 ± 10.5	354.6 ± 18
Backing	14	174.3 ± 12.6	345.7 ± 13
Matching	17	191.7 ± 14.8	348.6 ± 17

Therefore, the relative increase for all experimental data from the addition of a backing layer compared to PVdF film only is 1.32x and increase from adding a matching layer 1.09x. Stage 3 swPCD comparison to needle hydrophone and Sonic Concept PCD is 2.25x and 3.3x respectively.

7.2.4.3 Laser nucleated acoustic cavitation

Fig. 7.12 (a) are representative images of a HSC sequence of a LNAC cloud, imaged at 1 Mfps, and the corresponding voltage waveforms, collected by needle hydrophone fig. 7.12 (b), Sonic Concept PCD (c) and swPCD (d), with all PCD positioned according to fig 7.1 (b).

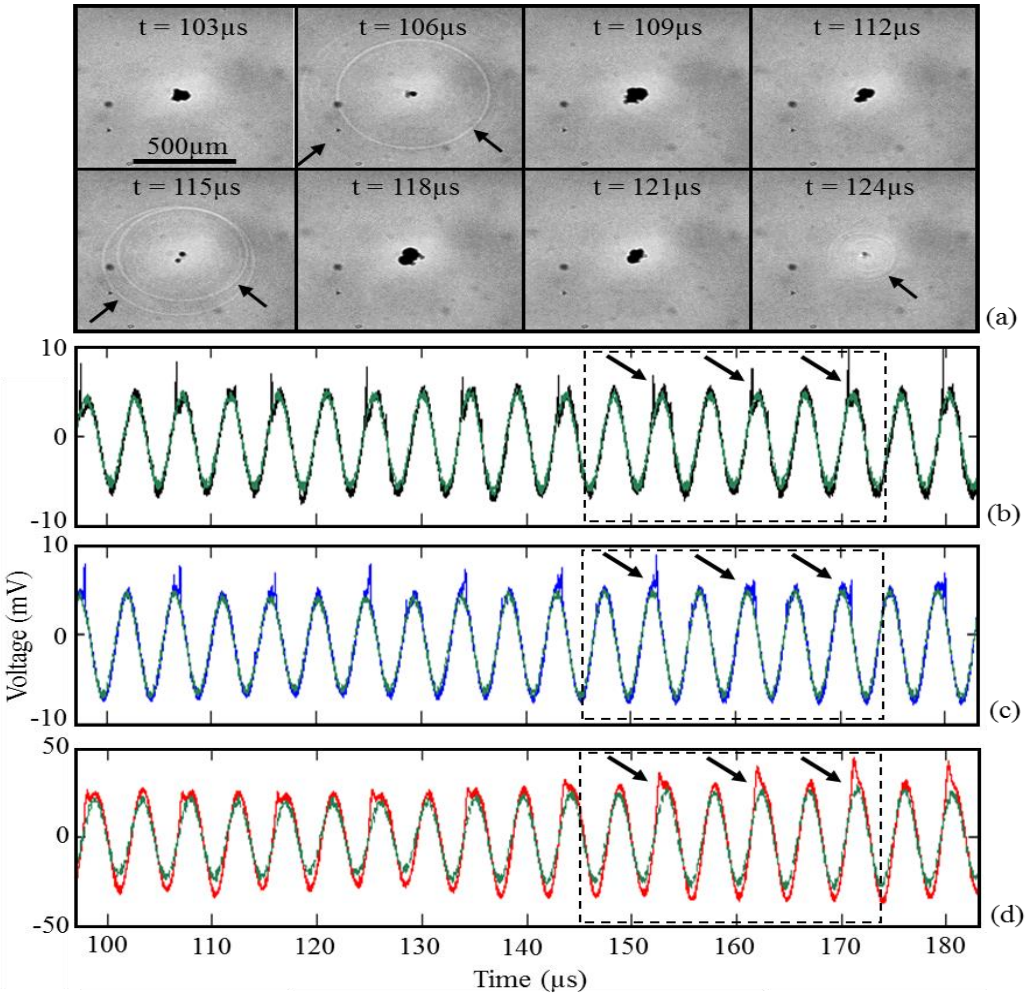

Figure 7.12. High-speed imaging of LNAC and corresponding voltage-time waveforms collected by swPCD and commercial detectors. (a) Imaging at 1Mfps illustrating periodic shockwaves (arrowed) emitted at $f_0/2$, corresponding to 9.12 ± 0.13 µs, with the driving frequency f_0 = 220 kHz. (b) Needle hydrophone waveform is collected from the imaged cloud, and corresponding shockwaves (arrowed), with a delay ~ 47 µs to account for 70 mm propagation distance. Also included is a control experiment overlaid (green) carried out with the nucleating laser blocked.

Fig 7.12 (b-d) shows ten shockwaves visible in the raw voltage signals for all PCD, with three shockwaves (arrowed) corresponding to HSC images, Fig. 7.12 (a). The time period between cloud collapse and shockwaves (measured by needle) emitted is 9.12 ± 0.13 µs corresponding to the $f_0/2$ subharmonic. The detection of the fundamental is

prominent in all waveforms, therefore the control (green) for each PCD, fig 7.12 (b-d) is subtracted to show PSWs for comparison to the swPCD, fig. 7.13 (a-c).

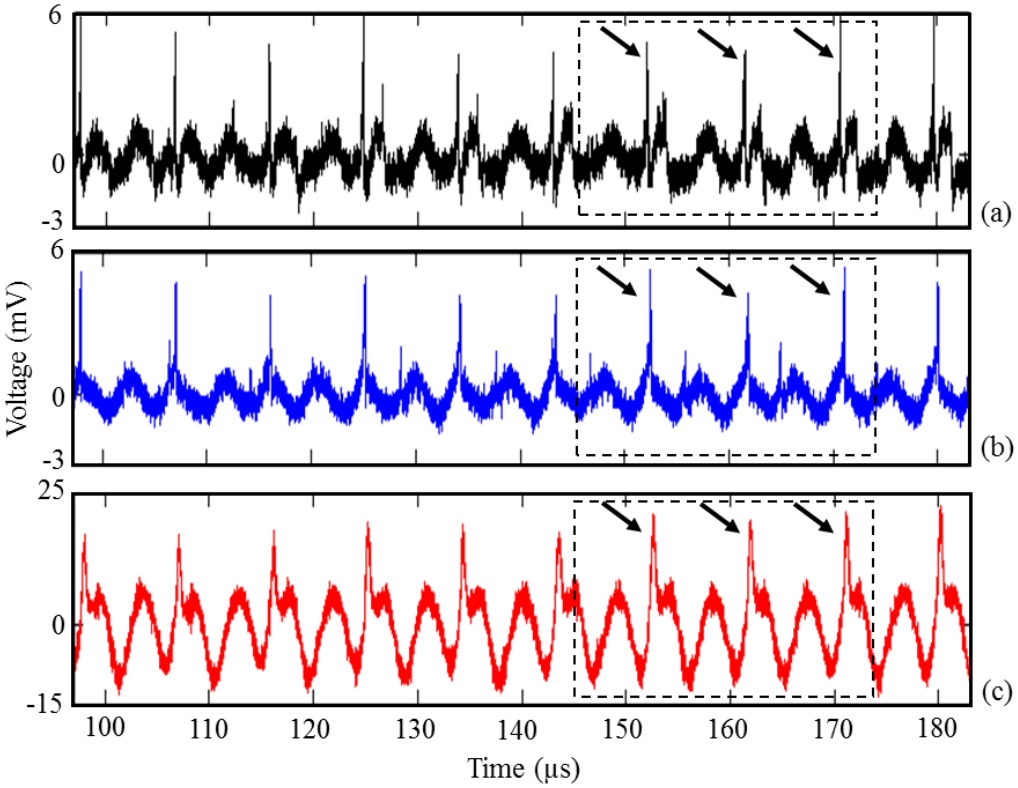

Figure 7.13. Control subtracted voltage-time waveforms of stage 3 swPCD and commercial detectors. (a) Needle hydrophone, (b) Sonic Concepts PCD and (c) the swPCD. Shockwaves arrowed correspond to the HSC images in fig.7.12 (a). Note different voltage scales from commercial detector (a, b) and swPCD (c).

The measured PPA for all ten shockwaves visible in fig. 7.13. (a-c) for needle hydrophone, Sonic Concepts and swPCD is 5.34 ± 1.28 mV, 4.66 ± 0.48 mV and 19.41 ± 1.91 mV. Therefore, in this experiment the swPCD is 3.63x greater at detecting low PPA PSWs compared to needle hydrophone and 4.16x greater than the Sonic Concepts PCD. This can also be represented in the frequency domain, by applying an FFT to the control-subtracted voltage response in fig 7.13 (a-c), as shown in fig 7.14 (a-c).

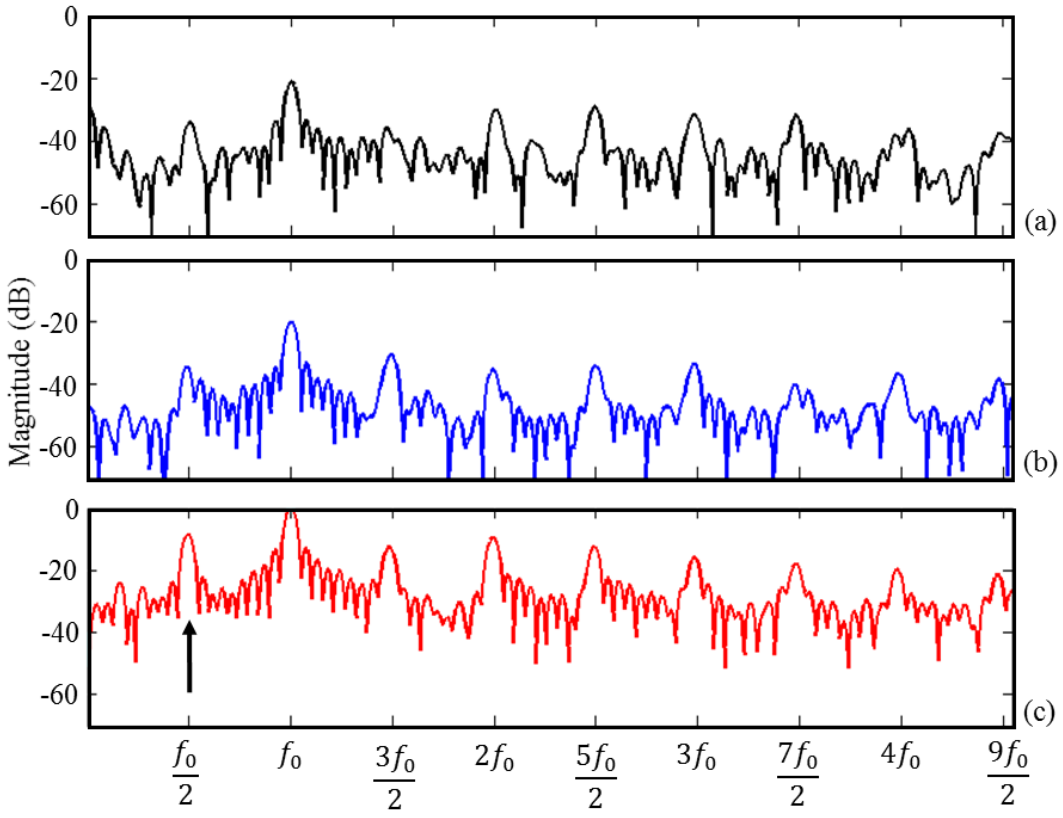

Figure 7.14. Spectra of the emissions collected from the LNAC cloud by stage 3 swPCD and commercial detectors. The FFT of the subtracted voltage waveform in fig 7.12 (a) The needle hydrophone (b) Sonic Concepts and (c) swPCD. All detectors are normalised to f_0 as detected by the swPCD, for comparison in dB.

Fig. 7.14 (a-c) shows the subharmonic $f_0/2$ (arrowed), harmonics and ultraharmonics are for all detectors. Both commercial detectors are normalised to swPCD for a comparison of the detected fundamental and subharmonic in dB. The measured power of the fundamental f_0 detected by needle, Sonic Concepts PCD and swPCD was -21.5, -21 and 0 dB and corresponding $f_0/2$ dB values are -34.6, -33.9 and -8.6. Therefore, the relative difference between swPCD and needle at f_0 is -21 dB and Sonic Concepts -21.5 and the relative difference between the swPCD at $f_0/2$ for the needle is 25.3 dB and Sonic Concepts -26 dB. This result demonstrates that by building a PCD sensitive to the

low frequency components of a shockwave increases the subharmonic power detected in the frequency domain.

7.2.4.4 Multi-fronted shockwaves

The decreased temporal resolution of the swPCD is further illustrated from a single high-speed image and comparing the shockwave detected by the swPCD and commercial detector, fig 7.15.

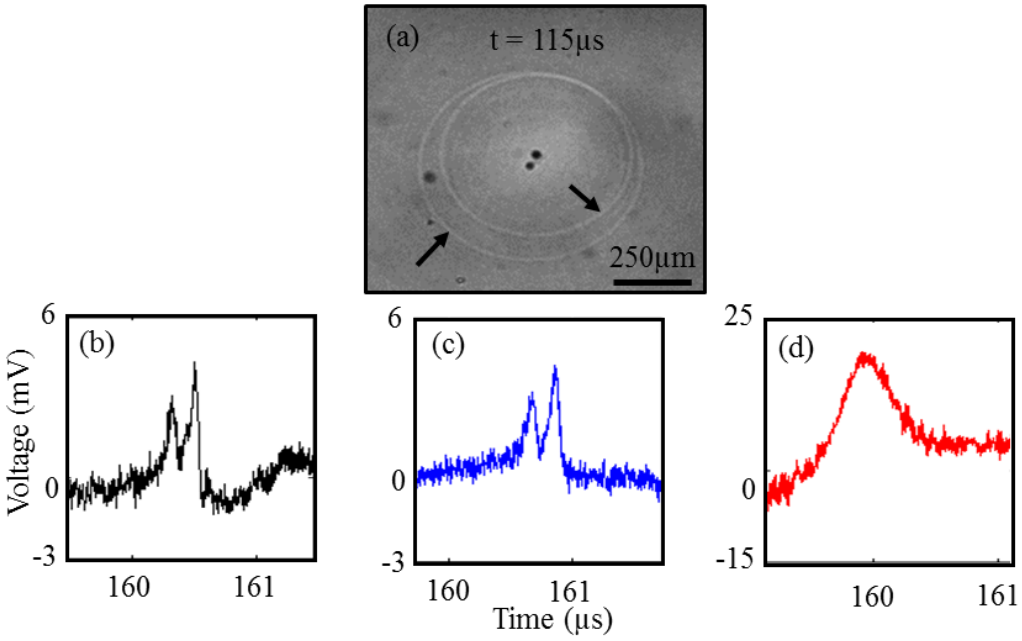

Figure 7.15. Single high-speed image and corresponding shockwave detection of stage 3 swPCD and commercial detectors. (a) A selected high-speed camera image of a multi-fronted shockwave (black arrowed) and corresponding PCD voltage-time signal (b) Sonic Concepts PCD (c) needle and (d) swPCD positioned ~ 70 mm from laser focus.

Fig 7.15 (a) is a high-speed image capturing a double fronted shockwaves emitted from the collapse of a cloud, which is detected by needle hydrophone (b), Sonic Concepts PCD (c) and swPCD (d). Both the needle and (focused) Sonic Concepts PCD are able to resolve the component shockwaves with the PPA of the needle 2.9/4.3 mV, compared to 3/4.1 mV for Sonic Concepts and a single peak voltage of 19.5 mV for the swPCD,

corresponding to the relative increase also demonstrated by OBSW comparison §7.2.4.2. The swPCD is unable to resolve the two shockwave due to its poor temporal resolution, and has a measured a FWHM of 424 ns, compared to the needle 42 ns and the Sonic Concepts 61 ns. The low temporal resolution of the swPCD explains why the PSWs are prominent in the subtracted voltage waveform of fig. 7.13 (c).

7.2.5 Discussion

The key driver to the results presented in the chapter is the identification of PSWs as the source of the subharmonic and identifying the need for a PCD that is optimised to detect them. This has led to the development of the swPCD, for comparison to a commonly reported PCD supplied by Sonic Concepts, using PZFlex to guide development and the dimension of the Sonic Concepts PCD to set the initial design. In this work, the emphasis has been on maximising shockwave sensitivity, but the general method of using PZFlex, OBSW for testing and a simple construction method can be applied to develop a PCD, specifically designed for the parameter considered most important, including low / high temporal resolution or maximising shockwave pressure. By selecting the thickness and active diameter, the sensitivity and temporal resolution of a shockwave measurement can be controlled. Decreasing film thickness increases the temporal resolution but decreases output voltage. Increasing active area increases the voltage output but the effect of shockwave spreading over a planar PCD surface, will further decrease temporal resolution, dependent on positioning relative to the cavitation. Whatever thickness and active area are selected, the addition of a heavy impedance backing and a matching layer can increase shockwave sensitivity. The relatively simple

design, and cost of ~£15, make the swPCD a useful alternative to commercial detectors to detect low PPA PSWs from LNAC.

7.2.6 Conclusion

PZFlex FE-simulations provide an effective means of virtually designing a PCD to maximise sensitivity from a shockwave. Basic understanding of the principles of how a PVdF film generates a voltage response is fundamental in understanding the FE simulation results. The addition of both a backing and matching layer has been shown to increase sensitivity to the low frequency components of a shockwave, confirmed by the frequency response, but decreases the temporal resolution. These two characteristics combine to clearly detect PSWs from cavitation clouds in the voltage-time domain, which corresponds to a higher magnitude subharmonic peak in the spectrum, when compared to needle hydrophone and Sonic Concepts PCD.

8 Conclusions and Future Work

The following points summarise the key results from the research presented in this thesis. This is followed by a brief discussion of how the experimental results may influence future work.

- The development of sonoptic chambers 1 and 2, combined with the high-speed camera and pulsed laser illumination, passive cavitation detection, and the laser nucleation technique, facilitated the observation and detection of periodic shockwaves as a mechanistic source of the subharmonic signal. This is considered the most significant result in this thesis.
- Full waveform deconvolution of the calibrated needle hydrophone from the cloud data, demonstrated the low peak positive pressure amplitude of shockwaves emitted from acoustic cavitation, prompting the development of a passive cavitation detector optimised for the detection of shockwaves.
- The design of a passive cavitation detector can be optimised for shockwave detection, using finite element simulation software, PZFlex. Detector performance was characterised using shockwaves from laser-induced bubbles, and shown to have superior sensitivity to the subharmonic signal, in comparison to commercial detectors.

Overall, the results presented in chapter 5 – 7 have increased knowledge of the acoustic signals emitted and detected from a single cavitation cloud, whereby the cloud dynamics can be resolved due to the transparent medium. The progression from understanding a single cloud dynamics over a relatively short 100 – 200 µs time scale

could be advanced into studying multiple clouds over a longer time period, using pulsed ms HIFU burst lengths. The interaction of multiple clouds dynamics, particularly the associated shockwave emissions and their influence on the frequency spectrum would have important implications for real cavitating systems. This could provide an incremental step to translate to cavitation cloud activity that occurs in tissue. In this medium the opaque nature of biological tissue, means optical techniques cannot be used. This further emphasises the clear need to objectively understand the signals detected by a single element PCD. In doing so a single element can be combined into a multi element array for passive acoustic mapping of the HIFU field. An array can achieve a high spatial and temporal resolution from several bubble clouds, using the frequencies spectrum as a method to observe the cavitation dynamics. In identifying the location and frequency response of the cavitating regions i.e. the subharmonic or higher order subharmonics could be used to develop control algorithms to feedback acoustic parameters, such as frequencies, pulse duration or acoustic pressure, to limit or promote cavitation activity to a specific locations identified. Cavitation is a complex phenomenon, developing algorithm and methods to control the cavitation dynamics, can only be beneficial to harness the power of collapsing bubbles to enhance lesion development for the treatment of cancer, for example. This would facilitate the translation of applying the results presented in this thesis for clinical applications, such as using the swPCD to detect acoustic emission in *ex vivo* tissue as part of a pre-clinical study.

A review of the various passive cavitation detectors commonly used to correlate bioeffects in HIFU, identified a current discussion in literature in relation to the subharmonic signal in the presence of microbubbles, particularly for the opening of the

blood brain barrier. The role from microbubbles or acoustic cavitation is still heavily under debate. Future work will aim to carry out experiments to observe the dynamics of microbubbles, driven by HIFU. The typically small µm diameter of a microbubble and the rapid movement within a HIFU field makes observations of microbubble dynamics a challenging task in the current sonoptic chambers. Therefore, a newly developed experimental setup, specifically designed to limit microbubble movement and allow a high magnification-imaging lens to observe 1) if a solution of microbubble under HIFU insonation collapse, emitting shockwaves / periodic shockwaves or 2) the microbubble shell or collapse fragment act as nuclei for acoustic cavitation and the correlate the results to the subharmonic signal. Indeed acoustic signals, which propagate through the skull, or tissue are poorly understood. The skull and tissue surely has an effect of changing the temporal shape of the detected voltage signal from shockwaves in the time domain, through attenuation for example. Clearly identifying the time domain signature from periodic shockwaves that propagate through the skull or tissue could provide an avenue for future work and would increase understanding of cavitation activity in relation to a range of bioeffects, including haemolysis, enhanced heated, mechanical tissue damage and blood brain barrier disruption. This could be achieved by using tissue mimicking phantoms or ex-vivo tissue experiments and comparing voltage signals and frequency response from single elements on the multi element arrays or by using the swPCD.

Further work will aim to more clearly distinguish between the stable and inertial cavitation classification and focus on broadband emissions, which are commonly reported to originate from inertial cavitation. Chapter 4 demonstrated that the subharmonic signal is generated by periodic shockwaves emitted at a time period corresponding to half the

driving. It would seem plausible to suggest that broadband emission may be connected to the periodicity between multi-fronted shockwaves emitted from the collapse of larger clouds, which collapse non uniformly. These clouds are characterised by spatially separated sub-clusters within the cloud, that collapse at different time intervals and each independently emit a single shock-front. Alternatively a medium that contains a significant number of clouds, which are independently undergoing growth, oscillation and collapse cycles emitting periodic shockwaves, at different locations, may appear as a broadband signal to a high temporal resolution passive cavitation detector. Thus researching the dynamics of multi cloud cavitation systems would seem a natural next step.

It is through simple experiments and small incremental steps in understanding that the complexity of cavitation dynamics can be understood. As technology develops, and greater optical and acoustic detection methods are combined with specialised control algorithm, the once wild, destructive and chaotic reputation of cavitation can be altered and the technology will lead to a controlled spatial nucleation and growth of a cloud of bubbles.

Appendix A: Cavitation-cloud manipulation in dual frequency focused ultrasound

Real time control of cavitation clouds is a formidable challenge due to the clouds stochastic nature and rapid dynamics. The following presents a novel technique of using dual frequency focused ultrasound to control the physical size and direction of the translation of the cloud.

Two focused bowl ultrasound transducers, operating at 1.184 MHz and 254 kHz are positioned diametrically inside the sonoptic chamber version 1 (V.1) (see §5.1.2), with the foci designed to overlap centrally inside the glass chamber. High-speed imaging of the cloud dynamics is undertaken using shimadzu HPV-1 high-speed camera at 1 x 10^6 frames per second.

To achieve a degree of spatial targeting, laser nucleated acoustic cavitation (see §3.3) is initiated using the tighter focus of the higher frequency burst, fig. A.1. (t = 0 – 20 µs). The 1.184 MHz transducer is positioned at the top of V.1 therefore the cloud propagates downwards under the action of radiation force.

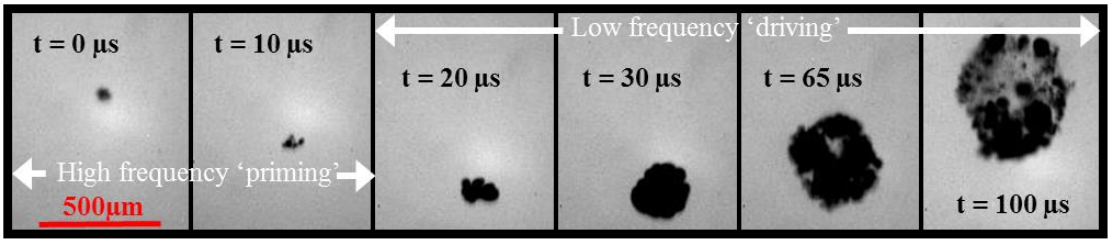

Figure A.1. Sample observations of cavitation cloud manipulation using dual frequency focused bowl transducers. Cavitation is nucleated using a burst of 1.184 MHz, driven downward with a secondary low frequency burst f_0 = 254 KHz, timed to drive the cloud upwards, increasing the size dependant on driving pressure.

A secondary, low frequency burst (propagating upwards) is delayed and timed to arrive at t = 20 μs, to drive the cloud upwards (t = 20 – 100 μs), increasing the cloud size, dependant on the driving pressure. This experiment demonstrates cavitation control using dual frequency transducers, but the experiment was limited due to a reflection of the opposing focused bowl which affecting the clouds dynamics after the initial bursts.

Appendix B1: Magnitude calibration

Calibration of the shockwave PCD and Sonic Concepts PCD took place in Precision Acoustics 1 x 1 x 1 m^3 scanning tank, using a degassed and filtration water system. Two techniques were used to characterise the frequency response, discrete frequency method (Preston et al., 1983) calibrated from 0.1-1Mhz and multiple frequency technique (Smith and Bacon, 1990) from 1.184 – 10MHz.

The discrete frequency method involves positioning the needle hydrophone (Calibrated by NPL, from 0.125- 20MHz) into the far field ~285 mm from the front face of a 35 mm diameter planar transducer, resonant frequency: 2.5 MHz. The hydrophone signal was maximised in the (x/z) planes perpendicular to the transducer face. The transducer was excited by 50 cycle burst using signal generator (DG4102, Rigol Technologies, Beijing, China) and power amplifier (ENI 2100L, Electronics and Innovation, NY, USA) from 0.1-1 MHz, in 0.1 MHz intervals, recording voltage-time signal using an oscilloscope (MS07104A, Agilent Technologies) at 4 GSs^{-1}. Peak pressure was calculated using Eq. (B.1) and the previously calibrated needle sensitivity, where sensitivity, (M (f)) is a function of frequency:

$$M(f) = \frac{\text{voltage (mV)}}{\text{Pressure (MPa)}} \quad \text{(B.1)}$$

For calibration of the swPCD and Sonic Concepts PCD, involves a substituted process into the same position in the far field, with the time delay from the transmitted pressure pulse to be received by the PCD, used to accurately positon the detector in the y-axis. The signal is also maximised in the planes (x/z) perpendicular to the transducer face. A 50 cycle burst from 0.1-1 MHz in 0.1 MHz intervals, recording voltage-time response. Sensitivity at each frequency interval was calculated using the peak voltage and previously calculated peak pressure by the needle hydrophone.

Additional 40 mm line scans at each frequency interval were undertaken though the focal region using the needle hydrophone, to assess for plane wave conditions. The International Electrotechnical Commission (IEC), released a criterion that suggests if the -1 dB beamwidth is greater than the effective diameter, then a corrective method is required to adjust for spatial averaging (Smith, 1989, Zeqiri and Bond, 1992). A linear line scan using the needle hydrophone at y = 285mm for each frequency interval, revealed a -1 dB beamwidth greater than the theoretical effective diameter, from 0.5-1 MHz. The effective hydrophone diameter, is not determined from the geometric active area diameter but by the directional response of the hydrophone (Radulescu et al., 2003). Assuming a circular piston model, the directional response can be expressed as:

$$D(\theta) = \frac{2J_1\{k\,.\,a\,.\,sin(\theta)]}{k\,.\,a\,.\,sin(\theta)} \quad \text{(B.2)}$$

Where $D(\theta)$ is the directivity of the hydrophone determined at angle θ and k are the wave number given by $k = 2\pi f / c$; f is the frequency and c is the speed of sound in water, a is

the geometric radius of the active element of the hydrophone and J_1 is the Bessel function of first order. The hydrophone effective radius is calculated from the mean of a_3 and a_6.

$$a_3 = \frac{1.62}{k\,.\sin(\theta_3)}\;;\; a_6 = \frac{2.22}{k\,.\sin(\theta_6)} \tag{B.3}$$

Where a_3 and a_6 are the effective radius calculated for the -3 and -6 dB respectively and $\theta_{-3}\theta_{-6}$ are the corresponding half angles.

The spatial averaging corrective method used here to correct both the swPCD, Sonic Concepts peak voltage response uses a standard theoretical model of a plane piston field to produce a relationship between the measured -6dB beam width in the far field of a plane circular transducer and the pressure correction, (δ) on axis, (Smith, 1989). The correction coefficient *(C)* is multiplied by the measured value to be corrected, where *C* is defined as $C = \delta + 1$. And delta (δ) is expressed as:

$$\delta = \frac{0.3}{\alpha^4}(\alpha^2 + 4.5) \tag{B.4}$$

Where

$$\alpha = \frac{measured - 6\ dB\ beamwidth}{effective\ hydrophone\ diameter} \tag{B.5}$$

The -6 dB beamwidth is measured from each linear line scan and combined with the effective hydrophone to determine the correction factor C, which is applied to measured peak voltage response from 0.5 - 1 MHz data. swPCD and Sonic Concepts sensitivity was calculated using the corrected peak voltage and previously calculated peak pressure by the needle hydrophone at each frequency interval, using Eq. (B.1).

The multiple frequency technique uses the harmonics present in a nonlinear waveform to calibrate over a wide frequency range simultaneously. The needle hydrophone is positioned ~390 mm in the y-axis from a focused bowl transducer, 64 mm diameter, 100 mm focal length, fundamental frequency 1.184 MHz. The voltage signal was maximised in the planes (x/z) perpendicular to the transducer face and the transducer was driven using a 50-cycle burst at 1V peak input driven by power amplifier, to produce a nonlinear waveform, fig. B.1 (a). The voltage signals were recorded to be analysed in MATLAB, peak pressure amplitude at each harmonics component is calculated via FFT, magnitude only deconvolution, (Hurrell, 2004) using interpolated sensitivity values, 1-20MHz. The detector to be calibrated is substituted into the far field, with the time delay from the transmitted pressure pulse to be received by the PCD, used to accurately positon the sensor in the y-axis. The voltage signal is maximised in the planes (x/z) perpendicular to the transducer face using a 50 cycle burst at 1.184 MHz and recording voltage-time waveform. A FFT reveals the peak voltage amplitude at each harmonic component; sensitivity is calculated using the peak voltage at each harmonic divided by the peak pressure previously calculated from the needle hydrophone. Fig. B.1 demonstrated the (a) nonlinear waveform and (b) harmonic component and the experientially determined (c) sensitivity in comparison to sensitivity calibrated by National Physics Laboratory, indicating a good experimental setup.

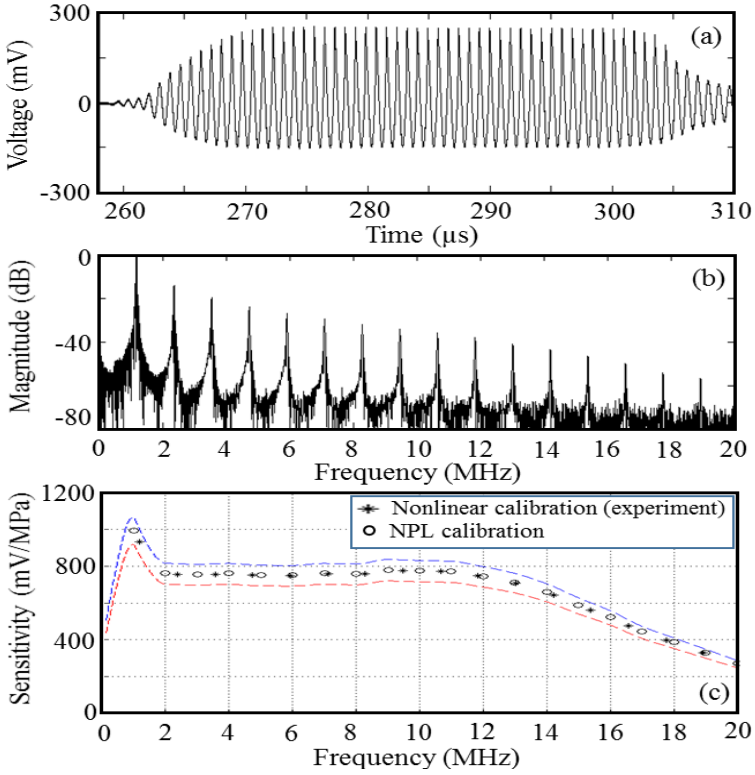

Figure B.1. (a) Needle hydrophone nonlinear experimental calibration compared to NPL (a) Voltage-time waveform **(b)** Fast Fourier Transform illustrating harmonic frequency content over calibrated frequency range in dB, (1.184 - 20MHz) **(c)** Sensitivity vs. frequency, comparing experimental non-linear calibration results of needle hydrophone using Multi-frequency technique at f_0 = 1.184MHz and NPL sensitivity calibration carried out at f_0 = 1MHz.

Appendix B2: Uncertainty in the measurement

When carrying out measurements of an ultrasound field, a measurement of the uncertainty involved in the calibration procedure should be undertaken. To quantify an uncertainty, two numbers are required. One is the width of the margin, or interval and the second is the level of confidence (i.e. 95% confidence level). Existing standards and guidelines require that the absolute sensitivity of the hydrophone to be calibrated involves inter-comparison with a reference hydrophone, whose sensitivity is determined by a

national Laboratory (Smith and Bacon, 1990, Preston et al., 1988, Ziskin, 2003). The primary calibration of the 1 mm needle hydrophone was carried out at NPL in the frequency range 0.1-20 MHz, with an overall uncertainty of ± 9% from 0.1-1MHz and ± 15% from 1-20MHz.

There are two main types of uncertainty, random and systematic, both are required to calculate total uncertainty. Random uncertainties are calculated by repeating an experiment and calculated by mean ($\bar{x}$) of the measurement (x_i).

$$\bar{x} = \frac{\sum_{i=1}^{n} x_i}{n} \tag{B.6}$$

And also the standard deviation (S_x) of the measurement.

$$S_x = \sqrt{\frac{\sum_{i=1}^{n} (x_i - \bar{x})^2}{n-1}} \tag{B.7}$$

Potential sources of random uncertainty include, misalignment of the hydrophone and acoustic source, variations in the signal to noise ratio between measurements, electrical noise including RF pick up, averaging error of the oscilloscope, instability in the transducer drive signal (Smith and Bacon, 1990) and environmental uncertainties such as air bubbles on the acoustic source or hydrophone or temperature changes between measurements. As it is difficult to quantify the exact contribution of each of the individual factors for this setup, uncertainty in the measurement of peak voltage are considered here. Random Uncertainties at the 95% Confidence interval are calculated by:

$$U_r = t_{0.95} \frac{S_x}{\sqrt{n}} \tag{B.8}$$

Where *t* is the appropriate student t factor, S_x is the standard deviation of the experiments and n is the number of measurements. For comparative purposes the random uncertainty expressed in percentage is calculated by:

$$\% \, U_r = \left(\frac{U_r}{\bar{x}}\right) . 100 \tag{B.9}$$

Systematic uncertainties (U_s) are determined by considering all of the non-random uncertainty and assessing the probability distribution and magnitude. Systematic uncertainty results from a repeatable fault in the measuring process, which has the same effects on every measurement. It is determined by analysing the various source of bias in each measurement. During experiments the same signal generator, power amplifier and oscilloscope was used to record voltage output from each detector. It is assumed that the systematic contribution from each source is the same and having a rectangular distribution. The main source of systematic error include the uncertainty in the primary calibration of the reference hydrophone by NPL and repeatability of the function generator (Rigol 4102), estimated to be ±2%, linearity of the power amplifier (ENI 2100L) over frequency range, estimated to be ±3%, and the recording the output of the sensor voltage via an oscilloscope, specified accuracy (±2% as per manufacturing data), Table B.1. A systematic error associated with the spatial averaging correction algorithm over both the sonic concepts and cavitation sensors area from 0.5 – 1MHz, estimated to be ± 7%.

Although the Sonic Concepts PCD was corrected for spatial averaging, no additional correction techniques could be found in the literature to correct for its geometric focus. As such, a large systemic error exists, included in all calculations,

therefore a ±10% error is included to compensate, included in both techniques and the entire frequency.

Table B.1: Systematic Uncertainty

		Frequency (MHz)		
No	Description	0.1 - 0.5	0.5 - 1	1 - 12
1	NPL Needle calibration	9	9	15
2	Signal Generator	2	2	2
3	Power Amplifier	3	3	3
4	Oscilliscope	2	2	3
5	Spatial Avaraging algorithm	0	7	0
6	Sonic Concepts geometric correction	10	10	10

When systematic uncertainties are combined, the resulting probability is approximated to be a normal distribution. Denoting the semi range of each contribution $a_{1,}a_{2,},etc$, the total variance of the resulting distribution (σ^2) is calculated by:

$$\sigma^2 = \sigma_1^2 + \sigma_2^2 \ldots + \sigma_n^2 \tag{B.10}$$

And the resulting systematic uncertainty (U_s) will be:

$$U_s = \sqrt{\sigma^2} = \sqrt{\frac{a_1^2 + a_2^2 \ldots + a_n^2}{3}} \tag{B.11}$$

The combined uncertainty (U_c), combines both the random and systematic uncertainty, after all corrections have been made, calculated by :

$$U_c = \sqrt{{U_r}^2 + {U_s}^2} \tag{B.12}$$

The total uncertainty (U) may be thought of as equivalent to 'one standard deviation', but to state the overall uncertainty at 95% confidence level, then the total uncertainty needs to be rescaled by a coverage factor (K):

$$U = k\, U_c \tag{B.13}$$

A coverage factor of k = 2 is used to scale the total uncertainty to give a level of confidence at 95% assuming a normal distribution. Table B.2 is an example of the method undertaken to calculate uncertainty in the measurement of peak voltage from the swPCD, using the multi-frequency hydrophone calibration technique, f_0 =.1.184 MHz.

Table B.2: An example of uncertainty of measurement for swPCD at $f_0 = 1.184$ MHz

Eq.	Measurements (x_i).	836.25, 846.93, 839.73, 840.04, 843.41, 843.63
B.6	Mean $\bar{x} = \frac{\sum_{i=1}^{6} x_i}{6}$	841.63
B.7	Standard deviation $S_x = \sqrt{\frac{\sum_{i=1}^{6}(x_i - \bar{\mathrm{x}})^2}{5}}$	3.73
B.8	Random uncertainty $U_r = t_{0.95}\frac{S_x}{\sqrt{n}}$	$U_r = 2.78\,.\frac{3.73}{\sqrt{6}} = 3.91$
B.9	Random uncertainty % $U_r\% = \left(\frac{U_r}{\bar{x}}\right).100$	$\%\, U_r = \left(\frac{3.73}{841.63}\right).100 = 0.46\ \%$
B.11	Systematic Uncertainty $U_s = \sqrt{\frac{a_1^2 + a_2^2 \ldots + a_n^2}{3}}$	$U_s = \sqrt{\frac{15^2 + 2^2 + 3^2 + 2^2}{3}} = 8.98$
B.12	Combined Uncertainty	$U_c = \sqrt{0.46^2 + 8.98^2} = 8.99$

$$U_c = \sqrt{{U_r}^2 + {U_s}^2}$$

B.13 Total Uncertainty

$$U = k\, U_T \qquad U = 2 \text{ x } 8.99 = 17.99$$

Measurement Result: 841.63mv ± 18% (95% C.I.)

References

APFEL, R. E. 1981. Acoustic cavitation prediction. *The Journal of the Acoustical Society of America,* 69**,** 1624-1633.

APFEL, R. E. & HOLLAND, C. K. 1991. Gauging the likelihood of cavitation from short-pulse, low-duty cycle diagnostic ultrasound. *Ultrasound in medicine & biology,* 17**,** 179-185.

ARVANITIS, C. D., CLEMENT, G. T. & MCDANNOLD, N. 2015. Transcranial Assessment and Visualization of Acoustic Cavitation: Modeling and Experimental Validation. *IEEE Transactions on Medical Imaging,* 34**,** 1270-1281.

ARVANITIS, C. D., LIVINGSTONE, M. S., VYKHODTSEVA, N. & MCDANNOLD, N. 2012. Controlled ultrasound-induced blood-brain barrier disruption using passive acoustic emissions monitoring. *PLoS One,* 7**,** e45783.

ASASE, T. & WATANABE, Y. 2004. Observation of shock wave propagation by a sonoluminescing bubble. *Japanese Journal of Applied Physics,* 43**,** 403.

AUBRY, J.-F., TANTER, M., PERNOT, M., THOMAS, J.-L. & FINK, M. 2003. Experimental demonstration of noninvasive transskull adaptive focusing based on prior computed tomography scans. *The Journal of the Acoustical Society of America,* 113**,** 84-93.

BACON, D. R. & CARSTENSEN, E. L. 1990. Increased heating by diagnostic ultrasound due to nonlinear propagation. *The Journal of the Acoustical Society of America,* 88**,** 26-34.

BADER, K. B. & HOLLAND, C. K. 2012. Gauging the likelihood of stable cavitation from ultrasound contrast agents. *Physics in medicine and biology,* 58**,** 127.

BANG, J. H. & SUSLICK, K. S. 2010. Applications of ultrasound to the synthesis of nanostructured materials. *Advanced materials,* 22**,** 1039-1059.

BARNETT, S. 1998. Nonthermal issues: Cavitation—Its nature, detection and measurement. *Ultrasound in medicine & biology,* 24**,** S11-S21.

BEARD, P. C., HURRELL, A. M. & MILLS, T. N. 2000. Characterization of a polymer film optical fiber hydrophone for use in the range 1 to 20 MHz: A comparison with PVDF needle and membrane hydrophones. *IEEE transactions on ultrasonics, ferroelectrics, and frequency control,* 47**,** 256-264.

BECKETT, M. A. & HUA, I. 2001. Impact of ultrasonic frequency on aqueous sonoluminescence and sonochemistry. *The Journal of Physical Chemistry A,* 105**,** 3796-3802.

BIRKIN, P. R., OFFIN, D. G., VIAN, C. J. & LEIGHTON, T. G. 2011. Multiple observations of cavitation cluster dynamics close to an ultrasonic horn tip. *The Journal of the Acoustical Society of America,* 130**,** 3379-3388.

BIRKIN, P. R., POWER, J. F., VINÇOTTE, A. M. & LEIGHTON, T. G. 2003. A 1 kHz resolution frequency study of a variety of sonochemical processes. *Physical Chemistry Chemical Physics,* 5**,** 4170-4174.

BLAKE JR, F. 1949. Bjerknes forces in stationary sound fields. *The Journal of the Acoustical Society of America,* 21**,** 551-551.

BRENNEN, C. E. 2011. An introduction to cavitation fundamentals.
BRENNEN, C. E. 2015. Cavitation in medicine. *Interface Focus,* 5**,** 20150022.
BROWN, L. F. 2000. Design considerations for piezoelectric polymer ultrasound transducers. *Ultrasonics, Ferroelectrics, and Frequency Control, IEEE Transactions on,* 47**,** 1377-1396.
BRUJAN, E.-A. & VOGEL, A. 2006. Stress wave emission and cavitation bubble dynamics by nanosecond optical breakdown in a tissue phantom. *Journal of Fluid Mechanics,* 558**,** 281-308.
BRUJAN, E., IKEDA, T. & MATSUMOTO, Y. 2012. Shock wave emission from a cloud of bubbles. *Soft Matter,* 8**,** 5777-5783.
BULL, V., CIVALE, J., RIVENS, I. & TER HAAR, G. 2013. A comparison of acoustic cavitation detection thresholds measured with piezo-electric and fiber-optic hydrophone sensors. *Ultrasound in medicine & biology,* 39**,** 2406-2421.
BUSCH, G. 1987. Early history of ferroelectricity. *Ferroelectrics,* 74**,** 267-284.
CANNEY, M. S., KHOKHLOVA, V. A., BESSONOVA, O. V., BAILEY, M. R. & CRUM, L. A. 2010. Shock-induced heating and millisecond boiling in gels and tissue due to high intensity focused ultrasound. *Ultrasound in medicine & biology,* 36**,** 250-267.
CAUPIN, F. & HERBERT, E. 2006. Cavitation in water: a review. *Comptes Rendus Physique,* 7**,** 1000-1017.
CHEN, W.-S., BRAYMAN, A. A., MATULA, T. J. & CRUM, L. A. 2003. Inertial cavitation dose and hemolysis produced in vitro with or without Optison®. *Ultrasound in medicine & biology,* 29**,** 725-737.
CHOI, J. J., CARLISLE, R. C., COVIELLO, C., SEYMOUR, L. & COUSSIOS, C.-C. 2014. Non-invasive and real-time passive acoustic mapping of ultrasound-mediated drug delivery. *Physics in medicine and biology,* 59**,** 4861.
CHUANG, K.-C., MA, C.-C. & LIOU, H.-C. 2012. Experimental investigation of the cross-sensitivity and size effects of polyvinylidene fluoride film sensors on modal testing. *Sensors,* 12**,** 16641-16659.
CHURCH, C. C. 1989. A theoretical study of cavitation generated by an extracorporeal shock wave lithotripter. *The Journal of the Acoustical Society of America,* 86**,** 215-227.
CHURCH, C. C. 2005. Frequency, pulse length, and the mechanical index. *Acoustics Research Letters Online,* 6**,** 162-168.
CHURCH, C. C. & CARSTENSEN, E. L. 2001. "Stable" inertial cavitation. *Ultrasound in medicine & biology,* 27**,** 1435-1437.
CLEMENT, G., SUN, J., GIESECKE, T. & HYNYNEN, K. 2000. A hemisphere array for non-invasive ultrasound brain therapy and surgery. *Physics in medicine and biology,* 45**,** 3707.
CLEVELAND, R. O. & MCATEER, J. A. 2012. Physics of Shock-Wave Lithotripsy. *Smith's Textbook of Endourology.* Wiley-Blackwell.
CLEVELAND, R. O., SAPOZHNIKOV, O. A., BAILEY, M. R. & CRUM, L. A. 2000. A dual passive cavitation detector for localized detection of lithotripsy-induced cavitation in vitro. *The Journal of the Acoustical Society of America,* 107**,** 1745-1758.

COAKLEY, W. 1971. Acoustical detection of single cavitation events in a focused field in water at 1 MHz. *The Journal of the Acoustical Society of America,* 49**,** 792-801.
COX, B. 2012. Acoustics for ultrasound imaging. *Lecture Notes, University College London*.
CRUM, L. & LAW, W. The relative roles of thermal and nonthermal effects in the use of high intensity focused ultrasound for the treatment of benign prostatic hyperplasia. Proceedings of the 15th International Congress on Acoustics, Trondheim, Norway, 1995. 315-318.
CRUM, L. A. 1975. Bjerknes forces on bubbles in a stationary sound field. *The Journal of the Acoustical Society of America,* 57**,** 1363-1370.
DALECKI, D., RAEMAN, C. H., CHILD, S. Z. & CARSTENSEN, E. L. 1997. Effects of pulsed ultrasound on the frog heart: III. The radiation force mechanism. *Ultrasound in medicine & biology,* 23**,** 275-285.
DANIELS, S., KODAMA, T. & PRICE, D. J. 1995. Damage to red blood cells induced by acoustic cavitation. *Ultrasound in medicine & biology,* 21**,** 105-111.
DATTA, S., COUSSIOS, C.-C., AMMI, A. Y., MAST, T. D., DE COURTEN-MYERS, G. M. & HOLLAND, C. K. 2008. Ultrasound-enhanced thrombolysis using Definity® as a cavitation nucleation agent. *Ultrasound in medicine & biology,* 34**,** 1421-1433.
DE SANTIS, P., SETTE, D. & WANDERLINGH, F. 1967. Cavitation detection: the use of the subharmonics. *The Journal of the Acoustical Society of America,* 42**,** 514-516.
DOINIKOV, A. A. 2001. Translational motion of two interacting bubbles in a strong acoustic field. *Physical review E,* 64**,** 026301.
DUCK, F. A. 2002. Nonlinear acoustics in diagnostic ultrasound. *Ultrasound in medicine & biology,* 28**,** 1-18.
EDWARD, H. W. & FORD, T. A. 1948. Polyvinylidene fluoride and process for obtaining the same. Google Patents.
EICHSTÄDT, S. & WILKENS, V. 2016. GUM2DFT—a software tool for uncertainty evaluation of transient signals in the frequency domain. *Measurement Science and Technology,* 27**,** 055001.
ELDER, S. A. 1959. Cavitation Microstreaming. *The Journal of the Acoustical Society of America,* 31**,** 54-64.
ELIAS, W. J., HUSS, D., VOSS, T., LOOMBA, J., KHALED, M., ZADICARIO, E., FRYSINGER, R. C., SPERLING, S. A., WYLIE, S. & MONTEITH, S. J. 2013. A pilot study of focused ultrasound thalamotomy for essential tremor. *New England Journal of Medicine,* 369**,** 640-648.
ELLER, A. & FLYNN, H. G. 1969. Generation of Subharmonics of Order One-Half by Bubbles in a Sound Field. *The Journal of the Acoustical Society of America,* 46**,** 722-727.
ELLER, A. I. & CRUM, L. A. 1970. Instability of the motion of a pulsating bubble in a sound field. *The Journal of the Acoustical Society of America,* 47**,** 762-767.
ESCHE, R. 1952. Untersuchung der schwingungskavitation in flüssigkeiten. *Acta Acustica united with Acustica,* 2**,** 208-218.

ESCOFFRE, J.-M. & BOUAKAZ, A. 2015. Therapeutic ultrasound. *Advances in experimental medicine and biology,(en cours d'édition)*.
EVERBACH, E. C., MAKIN, I. R. S., AZADNIV, M. & MELTZER, R. S. 1997. Correlation of ultrasound-induced hemolysis with cavitation detector output in vitro. *Ultrasound in medicine & biology,* 23**,** 619-624.
FARNY, C. H., HOLT, R. G. & ROY, R. A. 2010. The correlation between bubble-enhanced HIFU heating and cavitation power. *IEEE Transactions on Biomedical Engineering,* 57**,** 175-184.
FAY, B., LUDWIG, G., LANKJAER, C. & LEWIN, P. 1994. Frequency response of PVDF needle-type hydrophones. *Ultrasound in medicine & biology,* 20**,** 361-366.
FELVER, B., KING, D. C., LEA, S. C., PRICE, G. J. & WALMSLEY, A. D. 2009. Cavitation occurrence around ultrasonic dental scalers. *Ultrasonics sonochemistry,* 16**,** 692-697.
FERRARA, K., POLLARD, R. & BORDEN, M. 2007. Ultrasound microbubble contrast agents: fundamentals and application to gene and drug delivery. *Biomedical Engineering,* 9.
FLYNN, H. G. 1975. Cavitation dynamics. I. A mathematical formulation. *The Journal of the Acoustical Society of America,* 57**,** 1379-1396.
FOSTER, R. S., BIHRLE, R., SANGHVI, N. T., FRY, F. J. & DONOHUE, J. P. 1993. High-intensity focused ultrasound in the treatment of prostatic disease. *European urology,* 23 Suppl 1**,** 29-33.
FOWLKES, J. B. & HOLLAND, C. K. 2000. Section 2: definitions and description of nonthermal mechanisms. *Journal of ultrasound in medicine,* 19**,** 77-84.
FRY, F. J. 1958. Precision high intensity focusing ultrasonic machines for surgery. *American Journal of Physical Medicine & Rehabilitation,* 37**,** 152-156.
FRY, F. J., GOSS, S. A. & PATRICK, J. T. 1981. Transkull focal lesions in cat brain produced by ultrasound. *Journal of neurosurgery,* 54**,** 659-663.
FRY, W. & MEYERS, R. 1962. Ultrasonic method of modifying brain structures. *Stereotactic and Functional Neurosurgery,* 22**,** 315-327.
FURUKAWA, T. 1989. Piezoelectricity and pyroelectricity in polymers. *Electrical Insulation, IEEE Transactions on,* 24**,** 375-394.
GAITAN, D. F., CRUM, L. A., CHURCH, C. C. & ROY, R. A. 1992. Sonoluminescence and bubble dynamics for a single, stable, cavitation bubble. *The Journal of the Acoustical Society of America,* 91**,** 3166-3183.
GEROLD, B. 2013. *Cavitation in focused ultrasound.* University of Dundee.
GEROLD, B., KOTOPOULIS, S., MCDOUGALL, C., MCGLOIN, D., POSTEMA, M. & PRENTICE, P. 2011. Laser-nucleated acoustic cavitation in focused ultrasound. *Review of Scientific Instruments,* 82**,** 044902.
GEROLD, B., RACHMILEVITCH, I. & PRENTICE, P. 2013. Bifurcation of ensemble oscillations and acoustic emissions from early stage cavitation clouds in focused ultrasound. *New Journal of Physics,* 15**,** 033044.
GILMORE, F. R. 1952. The growth or collapse of a spherical bubble in a viscous compressible liquid.
GRANZ, B. 1989. PVDF hydrophone for the measurement of shock waves [lithotripsy]. *IEEE Transactions on Electrical Insulation,* 24**,** 499-502.

GYÖNGY, M. & COUSSIOS, C.-C. 2010a. Passive cavitation mapping for localization and tracking of bubble dynamics. *The Journal of the Acoustical Society of America,* 128**,** EL175-EL180.

GYÖNGY, M. & COUSSIOS, C.-C. 2010b. Passive spatial mapping of inertial cavitation during HIFU exposure. *IEEE Transactions on Biomedical Engineering,* 57**,** 48-56.

HAERTLING, G. H. 1999. Ferroelectric ceramics: history and technology. *J. Am. Ceram. Soc.,* 82**,** 797-818.

HALLOW, D. M., MAHAJAN, A. D., MCCUTCHEN, T. E. & PRAUSNITZ, M. R. 2006. Measurement and correlation of acoustic cavitation with cellular bioeffects. *Ultrasound in medicine & biology,* 32**,** 1111-1122.

HANSSON, I. & MØRCH, K. 1980. The dynamics of cavity clusters in ultrasonic (vibratory) cavitation erosion. *Journal of Applied Physics,* 51**,** 4651-4658.

HARPUT, S., RAITON, B., MCLAUGHLAN, J. R., EVANS, S. D. & FREEAR, S. The periodicity between the aggregated microbubbles by secondary radiation force. 2011 IEEE International Ultrasonics Symposium, 18-21 Oct. 2011 2011. 1630-1633.

HARRIS, G. R., PRESTON, R. C. & DEREGGI, A. S. 2000. The impact of piezoelectric PVDF on medical ultrasound exposure measurements, standards, and regulations. *IEEE transactions on ultrasonics, ferroelectrics, and frequency control,* 47**,** 1321-1335.

HENTSCHEL, W. & LAUTERBORN, W. 1982. Acoustic emission of single laser-produced cavitation bubbles and their dynamics. *Applied Scientific Research,* 38**,** 225-230.

HERRING, C. 1941. *Theory of the pulsations of the gas bubble produced by an underwater explosion*, Columbia Univ., Division of National Defense Research.

HOCKHAM, N., COUSSIOS, C. C. & ARORA, M. 2010. A real-time controller for sustaining thermally relevant acoustic cavitation during ultrasound therapy. *IEEE transactions on ultrasonics, ferroelectrics, and frequency control,* 57**,** 2685-2694.

HOERIG, C. L., SERRONE, J. C., BURGESS, M. T., ZUCCARELLO, M. & MAST, T. D. 2014. Prediction and suppression of HIFU-induced vessel rupture using passive cavitation detection in an ex vivo model. *Journal of Therapeutic Ultrasound,* 2**,** 1-18.

HOLLAND, C. K. & APFEL, R. E. 1989. An improved theory for the prediction of microcavitation thresholds. *Ultrasonics, Ferroelectrics, and Frequency Control, IEEE Transactions on,* 36**,** 204-208.

HOLLAND, C. K., DENG, C. X., APFEL, R. E., ALDERMAN, J. L., FERNANDEZ, L. A. & TAYLOR, K. J. 1996. Direct evidence of cavitation in vivo from diagnostic ultrasound. *Ultrasound in medicine & biology,* 22**,** 917-925.

HOLT, R. G. & ROY, R. A. 2001. Measurements of bubble-enhanced heating from focused, MHz-frequency ultrasound in a tissue-mimicking material. *Ultrasound in medicine & biology,* 27**,** 1399-1412.

HSIEH, D. 1974. On thresholds for surface waves and subharmonics of an oscillating bubble. *The Journal of the Acoustical Society of America,* 56**,** 392-393.

HURRELL, A. Voltage to pressure conversion: are you gettingphased'by the problem? Journal of Physics: Conference Series, 2004. IOP Publishing, 57.

HUSSEINI, G. A., DE LA ROSA, M. A. D., RICHARDSON, E. S., CHRISTENSEN, D. A. & PITT, W. G. 2005. The role of cavitation in acoustically activated drug delivery. *Journal of Controlled Release,* 107**,** 253-261.

HYNYNEN, K. 1991. The threshold for thermally significant cavitation in dog's thigh muscle in vivo. *Ultrasound in medicine & biology,* 17**,** 157-169.

HYNYNEN, K., CHUNG, A. H., COLUCCI, V. & JOLESZ, F. A. 1996. Potential adverse effects of high-intensity focused ultrasound exposure on blood vessels in vivo. *Ultrasound in medicine & biology,* 22**,** 193-201.

HYNYNEN, K. & JOLESZ, F. A. 1998. Demonstration of potential noninvasive ultrasound brain therapy through an intact skull. *Ultrasound in medicine & biology,* 24**,** 275-283.

HYNYNEN, K., MCDANNOLD, N., VYKHODTSEVA, N. & JOLESZ, F. A. 2001a. Noninvasive MR Imaging–guided Focal Opening of the Blood-Brain Barrier in Rabbits 1. *Radiology,* 220**,** 640-646.

HYNYNEN, K., POMEROY, O., SMITH, D. N., HUBER, P. E., MCDANNOLD, N. J., KETTENBACH, J., BAUM, J., SINGER, S. & JOLESZ, F. A. 2001b. MR imaging-guided focused ultrasound surgery of fibroadenomas in the breast: a feasibility study. *Radiology,* 219**,** 176-85.

HYNYNEN, K., VYKHODTSEVA, N. I., CHUNG, A. H., SORRENTINO, V., COLUCCI, V. & JOLESZ, F. A. 1997. Thermal effects of focused ultrasound on the brain: determination with MR imaging. *Radiology,* 204**,** 247-253.

IKEDA, T., YOSHIZAWA, S., TOSAKI, M., ALLEN, J. S., TAKAGI, S., OHTA, N., KITAMURA, T. & MATSUMOTO, Y. 2006. Cloud cavitation control for lithotripsy using high intensity focused ultrasound. *Ultrasound in medicine & biology,* 32**,** 1383-1397.

ILLING, R. O., KENNEDY, J. E., WU, F., TER HAAR, G. R., PROTHEROE, A. S., FRIEND, P. J., GLEESON, F. V., CRANSTON, D. W., PHILLIPS, R. R. & MIDDLETON, M. R. 2005. The safety and feasibility of extracorporeal high-intensity focused ultrasound (HIFU) for the treatment of liver and kidney tumours in a Western population. *Br J Cancer,* 93**,** 890-895.

J R BLAKE, A. & GIBSON, D. C. 1987. Cavitation Bubbles Near Boundaries. *Annual Review of Fluid Mechanics,* 19**,** 99-123.

JAFFE, B. 2012. *Piezoelectric ceramics,* Elsevier.

JAFFE, B., ROTH, R. S. & MARZULLO, S. 1954. Piezoelectric Properties of Lead Zirconate-Lead Titanate Solid-Solution Ceramics. *Journal of Applied Physics,* 25**,** 809-810.

JAGANNATHAN, J., SANGHVI, N. K., CRUM, L. A., YEN, C.-P., MEDEL, R., DUMONT, A. S., SHEEHAN, J. P., STEINER, L., JOLESZ, F. & KASSELL, N. F. 2009. High intensity focused ultrasound surgery (HIFU) of the brain: A historical perspective, with modern applications. *Neurosurgery,* 64**,** 201.

JENSEN, C. R., RITCHIE, R. W., GYÖNGY, M., COLLIN, J. R. T., LESLIE, T. & COUSSIOS, C.-C. 2012. Spatiotemporal Monitoring of High-Intensity Focused Ultrasound Therapy with Passive Acoustic Mapping. *Radiology,* 262**,** 252-261.

JOHNSTON, K., PRENTICE, P. & GEROLD, B. Cavitation cloud translation in focused ultrasound. 2014 IEEE International Ultrasonics Symposium, 3-6 Sept. 2014 2014a. 61-64.

JOHNSTON, K., TAPIA-SILES, C., GEROLD, B., POSTEMA, M., COCHRAN, S., CUSCHIERI, A. & PRENTICE, P. 2014b. Periodic shock-emission from acoustically driven cavitation clouds: A source of the subharmonic signal. *Ultrasonics,* 54**,** 2151-2158.

JONES, R. M., O'REILLY, M. A. & HYNYNEN, K. 2013. Transcranial passive acoustic mapping with hemispherical sparse arrays using CT-based skull-specific aberration corrections: a simulation study. *Physics in medicine and biology,* 58**,** 4981.

KATZIR, S. 2003. The discovery of the piezoelectric effect. *Archive for history of exact sciences,* 57**,** 61-91.

KAWAI, H. 1969. The piezoelectricity of poly (vinylidene fluoride). *Japanese Journal of Applied Physics,* 8**,** 975.

KELLER, J. B. & MIKSIS, M. 1980. Bubble oscillations of large amplitude. *The Journal of the Acoustical Society of America,* 68**,** 628-633.

KENNEDY, J., TER HAAR, G. & CRANSTON, D. 2014. High intensity focused ultrasound: surgery of the future? *The British journal of radiology*.

KHANNA, S., AMSO, N. N., PAYNTER, S. J. & COAKLEY, W. T. 2003. Contrast agent bubble and erythrocyte behavior in a 1.5-MHz standing ultrasound wave. *Ultrasound in medicine & biology,* 29**,** 1463-1470.

KHARAT, D., MITRA, S., AKHTAR, S. & KUMAR, V. 2007. Polymeric piezoelectric transducers for hydrophone applications. *Defence Science Journal,* 57**,** 7-22.

KIESSLING, F., FOKONG, S., KOCZERA, P., LEDERLE, W. & LAMMERS, T. 2012. Ultrasound microbubbles for molecular diagnosis, therapy, and theranostics. *Journal of nuclear medicine,* 53**,** 345-348.

KIM, Y., HALL, T. L., XU, Z. & CAIN, C. A. 2014. Transcranial histotripsy therapy: a feasibility study. *IEEE transactions on ultrasonics, ferroelectrics, and frequency control,* 61**,** 582-593.

KOCH, C. 2014. Sound field measurement in a double layer cavitation cluster by rugged miniature needle hydrophones. *Ultrasonics sonochemistry*.

KOCH, M., LECHNER, C., REUTER, F., KÖHLER, K., METTIN, R. & LAUTERBORN, W. 2016. Numerical modeling of laser generated cavitation bubbles with the finite volume and volume of fluid method, using OpenFOAM. *Computers & Fluids,* 126**,** 71-90.

KRANG, S. W., LEE, Y. P., KIM, K.-Y. & KWAK, H.-Y. 2003. Implosion mechanism for a sonoluminescing gas bubble. *Journal of the Korean Physical Society,* 43**,** 135-144.

KREIDER, W., CRUM, L. A., BAILEY, M. R. & SAPOZHNIKOV, O. A. 2011. A reduced-order, single-bubble cavitation model with applications to therapeutic ultrasound. *The Journal of the Acoustical Society of America,* 130**,** 3511-3530.

KREMKAU, F. W. 1979. Cancer therapy with ultrasound: a historical review. *Journal of Clinical Ultrasound,* 7**,** 287-300.

KRÖNINGER, D., KÖHLER, K., KURZ, T. & LAUTERBORN, W. 2010. Particle tracking velocimetry of the flow field around a collapsing cavitation bubble. *Experiments in fluids,* 48**,** 395-408.

KYRIAKOU, Z., CORRAL-BAQUES, M. I., AMAT, A. & COUSSIOS, C.-C. 2011. HIFU-induced cavitation and heating in ex vivo porcine subcutaneous fat. *Ultrasound in medicine & biology,* 37**,** 568-579.

LAUTERBORN, W. & CRAMER, E. 1981. Subharmonic route to chaos observed in acoustics. *Physical Review Letters,* 47**,** 1445.

LAUTERBORN, W. & KURZ, T. 2010. Physics of bubble oscillations. *Reports on progress in physics,* 73**,** 106501.

LAUTERBORN, W. & METTIN, R. 2015. 3 - Acoustic cavitation: bubble dynamics in high-power ultrasonic fields. *Power Ultrasonics.* Oxford: Woodhead Publishing.

LAUTERBORN, W. & PARLITZ, U. 1988. Methods of chaos physics and their application to acoustics. *The Journal of the Acoustical Society of America,* 84**,** 1975-1993.

LAW, W., FRIZZELL, L. & DUNN, F. 1985. Determination of the nonlinearity parameter B/A of biological media. *Ultrasound in medicine & biology,* 11**,** 307-318.

LEGRAND, J. 1989. Structure and ferroelectric properties of P (VDF-TrFE) copolymers. *Ferroelectrics,* 91**,** 303-317.

LEIGHTON, T. 1995. Bubble population phenomena in acoustic cavitation. *Ultrasonics sonochemistry,* 2**,** S123-S136.

LEIGHTON, T. 2012. *The acoustic bubble,* Academic press.

LEIGHTON, T. & CLEVELAND, R. 2010. Lithotripsy. *Proceedings of the Institution of Mechanical Engineers, Part H: Journal of Engineering in Medicine,* 224**,** 317-342.

LEIGHTON, T., FEDELE, F., COLEMAN, A., MCCARTHY, C., JAMALUDDIN, A., TURANGAN, C., BALL, G., RYVES, S., HURRELL, A. & WHITE, P. 2008. The development of a passive acoustic device for monitoring the effectiveness of shockwave lithotripsy in real time. *Hydroacoustics,* 11**,** 159-180.

LEIGHTON, T., TURANGAN, C., JAMALUDDIN, A., BALL, G. & WHITE, P. Prediction of far-field acoustic emissions from cavitation clouds during shock wave lithotripsy for development of a clinical device. Proc. R. Soc. A, 2013. The Royal Society, 20120538.

LEIGHTON, T., WALTON, A. & PICKWORTH, M. 1990. Primary bjerknes forces. *European Journal of Physics,* 11**,** 47.

LEIGHTON, T. G. 1997. A strategy for the development and standardisation of measurement methods for high power/cavitating ultrasonic fields: review of cavitation monitoring techniques. 22.

LEONG, T., ASHOKKUMAR, M. & KENTISH, S. 2011. The fundamentals of power ultrasound—a review. *Acoust. Aust,* 39**,** 54-63.

LI, H., DENG, Z. D. & CARLSON, T. J. 2012. Piezoelectric materials used in underwater acoustic transducers. *Sensor Letters,* 10**,** 679-697.

LIN, H., STOREY, B. D. & SZERI, A. J. 2002. Inertially driven inhomogeneities in violently collapsing bubbles: the validity of the Rayleigh–Plesset equation. *Journal of Fluid Mechanics,* 452**,** 145-162.

LINDSTROM, P. A. 1954. PRefrontal ultrasonic irradiation—a substitute for lobotomy. *A.M.A. Archives of Neurology & Psychiatry,* 72**,** 399-425.

LONGUET-HIGGINS, M. S. 1989. Monopole emission of sound by asymmetric bubble oscillations. Part 1. Normal modes. *Journal of Fluid Mechanics,* 201**,** 525-541.

LOUISNARD, O. & GONZÁLEZ-GARCÍA, J. 2011. Acoustic cavitation. *Ultrasound technologies for food and bioprocessing.* Springer.

LU, Y., KATZ, J. & PROSPERETTI, A. 2013. Dynamics of cavitation clouds within a high-intensity focused ultrasonic beam. *Physics of Fluids (1994-present),* 25**,** 073301.

LYNN, J. G., ZWEMER, R. L., CHICK, A. J. & MILLER, A. E. 1942. A new method for the generation and use of focused ultrasound in experimental biology. *The Journal of general physiology,* 26**,** 179.

MACDONALD, J. R. 1966. Some simple isothermal equations of state. *Reviews of Modern Physics,* 38**,** 669.

MASON, T. J. 2016. Ultrasonic cleaning: An historical perspective. *Ultrasonics sonochemistry,* 29**,** 519-523.

MCDANNOLD, N., VYKHODTSEVA, N. & HYNYNEN, K. 2006. Targeted disruption of the blood–brain barrier with focused ultrasound: association with cavitation activity. *Physics in medicine and biology,* 51**,** 793.

MCLAUGHLAN, J., RIVENS, I., HAAR, G. T., SHAW, A., LEIGHTON, T., HUMPHREY, V., BIRKIN, P. & VIAN, C. The design and implementation of a passive cavitation detection system for use with ex vivo tissue. Therapeutic Ultrasound: 5 th International Symposium on Therapeutic Ultrasound, 2006. 338-342.

MCLAUGHLAN, J., RIVENS, I., LEIGHTON, T. & TER HAAR, G. 2010. A Study of Bubble Activity Generated in Ex Vivo Tissue by High Intensity Focused Ultrasound. *Ultrasound in medicine & biology,* 36**,** 1327-1344.

METTIN, R., AKHATOV, I., PARLITZ, U., OHL, C. & LAUTERBORN, W. 1997. Bjerknes forces between small cavitation bubbles in a strong acoustic field. *Physical review E,* 56**,** 2924.

MILLER, D. L. 2007. Overview of experimental studies of biological effects of medical ultrasound caused by gas body activation and inertial cavitation. *Progress in Biophysics and Molecular Biology,* 93**,** 314-330.

MILLER, D. L., SMITH, N. B., BAILEY, M. R., CZARNOTA, G. J., HYNYNEN, K., MAKIN, I. R. S. & MEDICINE, B. C. O. T. A. I. O. U. I. 2012. Overview of therapeutic ultrasound applications and safety considerations. *Journal of ultrasound in medicine,* 31**,** 623-634.

MINNAERT, M. 1933. XVI. On musical air-bubbles and the sounds of running water. *The London, Edinburgh, and Dublin Philosophical Magazine and Journal of Science,* 16**,** 235-248.

MORRIS, P., HURRELL, A. & BEARD, P. Moving towards an ideal frequency response with fibre-optic hydrophones. 2009 IEEE International Ultrasonics Symposium, 2009. IEEE, 944-947.

MORTON, K., TER HAAR, G., STRATFORD, I. & HILL, C. 1983. Subharmonic emission as an indicator of ultrasonically-induced biological damage. *Ultrasound in medicine & biology,* 9**,** 629-633.

MUIR, T. & CARSTENSEN, E. 1980. Prediction of nonlinear acoustic effects at biomedical frequencies and intensities. *Ultrasound in medicine & biology,* 6**,** 345-357.

NELSON, T. R., FOWLKES, J. B., ABRAMOWICZ, J. S. & CHURCH, C. C. 2009. Ultrasound biosafety considerations for the practicing sonographer and sonologist. *Journal of ultrasound in medicine,* 28**,** 139-150.

NEPPIRAS, E. 1969. Subharmonic and Other Low-Frequency Emission from Bubbles in Sound-Irradiated Liquids. *The Journal of the Acoustical Society of America,* 46**,** 587-601.

NEPPIRAS, E. A. 1980. Acoustic cavitation. *Physics reports,* 61**,** 159-251.

NEWELL, J. 1963. Ultrasonics in medicine. *Physics in medicine and biology,* 8**,** 241.

NIGHTINGALE, K. R., KORNGUTH, P. J. & TRAHEY, G. E. 1999. The use of acoustic streaming in breast lesion diagnosis: a clinical study. *Ultrasound in medicine & biology,* 25**,** 75-87.

NOACK, J., HAMMER, D. X., NOOJIN, G. D., ROCKWELL, B. A. & VOGEL, A. 1998. Influence of pulse duration on mechanical effects after laser-induced breakdown in water. *Journal of Applied Physics,* 83**,** 7488-7495.

NOMURA, S., MUKASA, S., KUROIWA, M., OKADA, Y. & MURAKAMI, K. 2005. Cavitation bubble streaming in ultrasonic-standing-wave field. *Japanese Journal of Applied Physics,* 44**,** 3161.

O'REILLY, M. A. & HYNYNEN, K. 2012. Blood-brain barrier: real-time feedback-controlled focused ultrasound disruption by using an acoustic emissions–based controller. *Radiology,* 263**,** 96-106.

OGUZ, H. N. & PROSPERETTI, A. 1990. A generalization of the impulse and virial theorems with an application to bubble oscillations. *Journal of Fluid Mechanics,* 218**,** 143-162.

OHL, C. D., KURZ, T., GEISLER, R., LINDAU, O. & LAUTERBORN, W. 1999. Bubble dynamics, shock waves and sonoluminescence. *Philosophical Transactions of the Royal Society of London A: Mathematical, Physical and Engineering Sciences,* 357**,** 269-294.

OREILLY, M. & HYNYNEN, K. 2010. A PVDF receiver for ultrasound monitoring of transcranial focused ultrasound therapy. *Biomedical Engineering, IEEE Transactions on,* 57**,** 2286-2294.

PARDRIDGE, W. M. 2002. Drug and Gene Delivery to the Brain. *Neuron,* 36**,** 555-558.

PARLITZ, U., ENGLISCH, V., SCHEFFCZYK, C. & LAUTERBORN, W. 1990. Bifurcation structure of bubble oscillators. *The Journal of the Acoustical Society of America,* 88**,** 1061-1077.

PARLITZ, U., METTIN, R., LUTHER, S., AKHATOV, I., VOSS, M. & LAUTERBORN, W. 1999. Spatio–temporal dynamics of acoustic cavitation

bubble clouds. *Philosophical Transactions of the Royal Society of London A: Mathematical, Physical and Engineering Sciences,* 357**,** 313-334.

PELEKASIS, N. A., GAKI, A., DOINIKOV, A. & TSAMOPOULOS, J. A. 2004. Secondary Bjerknes forces between two bubbles and the phenomenon of acoustic streamers. *Journal of Fluid Mechanics,* 500**,** 313-347.

PHILIPP, A. & LAUTERBORN, W. 1998. Cavitation erosion by single laser-produced bubbles. *Journal of Fluid Mechanics,* 361**,** 75-116.

POLIACHIK, S. L., CHANDLER, W. L., MOURAD, P. D., BAILEY, M. R., BLOCH, S., CLEVELAND, R. O., KACZKOWSKI, P., KEILMAN, G., PORTER, T. & CRUM, L. A. 1999. Effect of high-intensity focused ultrasound on whole blood with and without microbubble contrast agent. *Ultrasound in medicine & biology,* 25**,** 991-998.

POLIACHIK, S. L., CHANDLER, W. L., OLLOS, R. J., BAILEY, M. R. & CRUM, L. A. 2004. The relation between cavitation and platelet aggregation during exposure to high-intensity focused ultrasound. *Ultrasound in medicine & biology,* 30**,** 261-269.

POSTEMA, M., MARMOTTANT, P., LANCÉE, C. T., HILGENFELDT, S. & DE JONG, N. 2004a. Ultrasound-induced microbubble coalescence. *Ultrasound in medicine & biology,* 30**,** 1337-1344.

POSTEMA, M., VAN WAMEL, A., LANCÉE, C. T. & DE JONG, N. 2004b. Ultrasound-induced encapsulated microbubble phenomena. *Ultrasound in medicine & biology,* 30**,** 827-840.

PRENTICE, P., CUSCHIERI, A., DHOLAKIA, K., PRAUSNITZ, M. & CAMPBELL, P. 2005. Membrane disruption by optically controlled microbubble cavitation. *Nature Physics,* 1**,** 107-110.

PRESTON, R., BACON, D., LIVETT, A. & RAJENDRAN, K. 1983. PVDF membrane hydrophone performance properties and their relevance to the measurement of the acoustic output of medical ultrasonic equipment. *Journal of Physics E: Scientific Instruments,* 16**,** 786.

PRESTON, R., BACON, D. R. & SMITH, R. A. 1988. Calibration of medical ultrasonic equipment-procedures and accuracy assessment. *Ultrasonics, Ferroelectrics, and Frequency Control, IEEE Transactions on,* 35**,** 110-121.

PROKOP, A. F., SOLTANI, A. & ROY, R. A. 2007. Cavitational mechanisms in ultrasound-accelerated fibrinolysis. *Ultrasound in medicine & biology,* 33**,** 924-933.

PROSPERETTI, A. 1975. Nonlinear oscillations of gas bubbles in liquids. Transient solutions and the connection between subharmonic signal and cavitation. *The Journal of the Acoustical Society of America,* 57**,** 810-821.

PROSPERETTI, A. 2013. A general derivation of the subharmonic threshold for non-linear bubble oscillations. *The Journal of the Acoustical Society of America,* 133**,** 3719-3726.

PROSPERETTI, A. & LEZZI, A. 1986. Bubble dynamics in a compressible liquid. Part 1. First-order theory. *Journal of Fluid Mechanics,* 168**,** 457-478.

RADULESCU, E., LEWIN, P., NOWICKI, A. & BERGER, W. 2003. Hydrophones' effective diameter measurements as a quasi-continuous function of frequency. *Ultrasonics,* 41**,** 635-641.

RAYLEIGH, L. 1917. VIII. On the pressure developed in a liquid during the collapse of a spherical cavity. *The London, Edinburgh, and Dublin Philosophical Magazine and Journal of Science,* 34**,** 94-98.

REN, X.-L., ZHOU, X.-D., ZHANG, J., HE, G.-B., HAN, Z.-H., ZHENG, M.-J., LI, L., YU, M. & WANG, L. 2007. Extracorporeal ablation of uterine fibroids with high-intensity focused ultrasound imaging and histopathologic evaluation. *Journal of ultrasound in medicine,* 26**,** 201-212.

RICHARDS, W. T. & LOOMIS, A. L. 1927. The chemical effects of high frequency sound waves I. A preliminary survey. *Journal of the American Chemical Society,* 49**,** 3086-3100.

RIESZ, P. & KONDO, T. 1992. Free radical formation induced by ultrasound and its biological implications. *Free Radical Biology and Medicine,* 13**,** 247-270.

ROBINSON, S., PRESTON, R., SMITH, M. & MILLAR, C. 2000. PVDF reference hydrophone development in the UK-from fabrication and lamination to use as secondary standards. *IEEE transactions on ultrasonics, ferroelectrics, and frequency control,* 47**,** 1336-1344.

ROY, R. A., MADANSHETTY, S. I. & APFEL, R. E. 1990. An acoustic backscattering technique for the detection of transient cavitation produced by microsecond pulses of ultrasound. *The Journal of the Acoustical Society of America,* 87**,** 2451-2458.

SALGAONKAR, V. A., DATTA, S., HOLLAND, C. K. & MAST, T. D. 2009. Passive cavitation imaging with ultrasound arrays. *The Journal of the Acoustical Society of America,* 126**,** 3071-3083.

SAYERS, C. & TAIT, C. 1984. Ultrasonic properties of transducer backings. *Ultrasonics,* 22**,** 57-60.

SCHAFER, M., KRAYNAK, T. & KRAKHMAN, V. Development of a cost-effective shock wave hydrophone. Ultrasonics Symposium, 1994. Proceedings., 1994 IEEE, 1994. IEEE, 1805-1808.

SCHAFER, M. E., KRAYNAK, T. L. & LEWIN, P. Design of a miniature in-vivo shock wave hydrophone. Ultrasonics Symposium, 1990. Proceedings., IEEE 1990, 1990. IEEE, 1623-1626.

SCHOELLHAMMER, C. M., SCHROEDER, A., MAA, R., LAUWERS, G. Y., SWISTON, A., ZERVAS, M., BARMAN, R., DICICCIO, A. M., BRUGGE, W. R. & ANDERSON, D. G. 2015. Ultrasound-mediated gastrointestinal drug delivery. *Science translational medicine,* 7**,** 310ra168-310ra168.

SEDGEWICK, S. & TREVENA, D. 1976. Limiting negative pressure of water under dynamic stressing. *Journal of Physics D: Applied Physics,* 9**,** 1983.

SESSLER, G. M. 1981. Piezoelectricity in polyvinylidenefluoride. *The Journal of the Acoustical Society of America,* 70**,** 1596-1608.

SHAW, A. & HODNETT, M. 2008. Calibration and measurement issues for therapeutic ultrasound. *Ultrasonics,* 48**,** 234-252.

SHAW, S. & SPELT, P. 2010. Shock emission from collapsing gas bubbles. *Journal of Fluid Mechanics,* 646**,** 363-373.

SHERMAN, C. H. & BUTLER, J. L. 2007. *Transducers and arrays for underwater sound*, Springer.
SHI, X., MARTIN, R. W., VAEZY, S. & CRUM, L. A. 2002. Quantitative investigation of acoustic streaming in blood. *The Journal of the Acoustical Society of America,* 111**,** 1110-1121.
SMITH, R. A. 1989. Are hydrophones of diameter 0.5 mm small enough to characterise diagnostic ultrasound equipment? *Physics in medicine and biology,* 34**,** 1593.
SMITH, R. A. & BACON, D. R. 1990. A multiple-frequency hydrophone calibration technique. *The Journal of the Acoustical Society of America,* 87**,** 2231-2243.
SOKKA, S., KING, R. & HYNYNEN, K. 2003. MRI-guided gas bubble enhanced ultrasound heating in in vivo rabbit thigh. *Physics in medicine and biology,* 48**,** 223.
SPECIALTIES, M. 2013. Piezo Film Sensors Technical Manual.
STAUDENRAUS, J. & EISENMENGER, W. 1993. Fibre-optic probe hydrophone for ultrasonic and shock-wave measurements in water. *Ultrasonics,* 31**,** 267-273.
STRUBE, H. 1971. Numerical investigations on the stability of bubbles oscillating non-spherically. *Acta Acustica united with Acustica,* 25**,** 289-303.
SUN, E. & CAO, W. 2014. Relaxor-based ferroelectric single crystals: Growth, domain engineering, characterization and applications. *Progress in materials science,* 65**,** 124-210.
SUSLICK, K. S. & CRUM, L. A. 1998. *Sonochemistry and sonoluminescence*, Wiley-Interscience: New York.
SUSLICK, K. S., MDLELENI, M. M. & RIES, J. T. 1997. Chemistry induced by hydrodynamic cavitation. *Journal of the American Chemical Society,* 119**,** 9303-9304.
SZABO, T. L. 2004. *Diagnostic ultrasound imaging: inside out*, Academic Press.
TANCRELL, R., WILSON, D. & RICKETTS, D. Properties of PVDF polymer for sonar. IEEE 1985 Ultrasonics Symposium, 1985. IEEE, 624-629.
TAVAKKOLI, J., BIRER, A. & CATHIGNOL, D. 1996. Development of a PVDF low-cost shock-wave hydrophone. *Shock Waves,* 5**,** 369-374.
TER, G. R., CLARKE, R. L., VAUGHAN, M. G. & HILL, C. R. 1991. Trackless surgery using focused ultrasound: Technique and case report. *Minimally Invasive Therapy,* 1**,** 13-19.
TER HAAR, G., SINNETT, D. & RIVENS, I. 1989. High intensity focused ultrasound-a surgical technique for the treatment of discrete liver tumours. *Physics in medicine and biology,* 34**,** 1743.
TER HARR, G., DANIELS, S. & MORTON, K. 1986. Evidence for acoustic cavitation in vivo: Thresholds for bubble formation with 0.75-MHz continuous wave and pulsed beams. *IEEE transactions on ultrasonics, ferroelectrics, and frequency control,* 33**,** 162-164.
TERVO, J. T., METTIN, R. & LAUTERBORN, W. 2006. Bubble cluster dynamics in acoustic cavitation. *Acta Acustica united with Acustica,* 92**,** 178-180.
THIEMANN, A., NOWAK, T., METTIN, R., HOLSTEYNS, F. & LIPPERT, A. 2011. Characterization of an acoustic cavitation bubble structure at 230kHz. *Ultrasonics sonochemistry,* 18**,** 595-600.

TORR, G. R. 1984. The acoustic radiation force. *American Journal of Physics,* 52**,** 402-408.

TSAI, C.-H., ZHANG, J.-W., LIAO, Y.-Y. & LIU, H.-L. 2016. Real-time monitoring of focused ultrasound blood-brain barrier opening via subharmonic acoustic emission detection: implementation of confocal dual-frequency piezoelectric transducers. *Physics in medicine and biology,* 61**,** 2926.

TUNG, Y.-S., VLACHOS, F., CHOI, J. J., DEFFIEUX, T., SELERT, K. & KONOFAGOU, E. E. 2010a. In vivo transcranial cavitation threshold detection during ultrasound-induced blood–brain barrier opening in mice. *Physics in medicine and biology,* 55**,** 6141.

TUNG, Y. S., CHOI, J. J. & KONOFAGOU, E. E. 2010b. Identifying the Inertial Cavitation Pressure Threshold and Skull Effects in a Vessel Phantom Using Focused Ultrasound and Microbubbles. *AIP Conference Proceedings,* 1215**,** 186-189.

VAEZY, S., SHI, X., MARTIN, R. W., CHI, E., NELSON, P. I., BAILEY, M. R. & CRUM, L. A. 2001. Real-time visualization of high-intensity focused ultrasound treatment using ultrasound imaging. *Ultrasound in medicine & biology,* 27**,** 33-42.

VAN TERWISGA, T. J., FITZSIMMONS, P. A., ZIRU, L. & FOETH, E. J. Cavitation Erosion–A review of physical mechanisms and erosion risk models. 7th International Symposium on Cavitation, 2009. 1-13.

VAUGHAN, P. W. 1968. Investigation of acoustic cavitation thresholds by observation of the first subharmonic. *Journal of Sound and Vibration,* 7**,** 236-246.

VERSLUIS, M., GOERTZ, D. E., PALANCHON, P., HEITMAN, I. L., VAN DER MEER, S. M., DOLLET, B., DE JONG, N. & LOHSE, D. 2010. Microbubble shape oscillations excited through ultrasonic parametric driving. *Physical review E,* 82**,** 026321.

VOGEL, A. 1997. Nonlinear absorption: intraocular microsurgery and laser lithotripsy. *Physics in medicine and biology,* 42**,** 895.

VOGEL, A., BUSCH, S. & PARLITZ, U. 1996. Shock wave emission and cavitation bubble generation by picosecond and nanosecond optical breakdown in water. *The Journal of the Acoustical Society of America,* 100**,** 148-165.

VYKHODTSEVA, N., HYNYNEN, K. & DAMIANOU, C. 1995. Histologic effects of high intensity pulsed ultrasound exposure with subharmonic emission in rabbit brain in vivo. *Ultrasound in medicine & biology,* 21**,** 969-979.

WADA, Y. & HAYAKAWA, R. 1976. Piezoelectricity and pyroelectricity of polymers. *Japanese Journal of Applied Physics,* 15**,** 2041.

WANG, H., RITTER, T. A., CAO, W. & SHUNG, K. K. 2001. High frequency properties of passive materials for ultrasonic transducers. *Ultrasonics, Ferroelectrics, and Frequency Control, IEEE Transactions on,* 48**,** 78-84.

WATKIN, N. A., TER HAAR, G. R. & RIVENS, I. 1996. The intensity dependence of the site of maximal energy deposition in focused ultrasound surgery. *Ultrasound in medicine & biology,* 22**,** 483-491.

WEITENDORF, E. On the history of propeller cavitation and cavitation tunnels. Fourth International Symposium on Cavitation, 2001.

WIKLUND, M., GREEN, R. & OHLIN, M. 2012. Acoustofluidics 14: Applications of acoustic streaming in microfluidic devices. *Lab on a Chip,* 12**,** 2438-2451.

WILKENS, V., SONNTAG, S. & GEORG, O. 2016. Robust spot-poled membrane hydrophones for measurement of large amplitude pressure waveforms generated by high intensity therapeutic ultrasonic transducers. *The Journal of the Acoustical Society of America,* 139**,** 1319-1332.

WU, F., CHEN, W.-Z., BAI, J., ZOU, J.-Z., WANG, Z.-L., ZHU, H. & WANG, Z.-B. 2001. Pathological changes in human malignant carcinoma treated with high-intensity focused ultrasound. *Ultrasound in medicine & biology,* 27**,** 1099-1106.

WU, F., WANG, Z.-B., CHEN, W.-Z., WANG, W., GUI, Y., ZHANG, M., ZHENG, G., ZHOU, Y., XU, G. & LI, M. 2004. Extracorporeal high intensity focused ultrasound ablation in the treatment of 1038 patients with solid carcinomas in China: an overview. *Ultrasonics sonochemistry,* 11**,** 149-154.

WU, F., WANG, Z. B., CAO, Y. D., CHEN, W. Z., BAI, J., ZOU, J. Z. & ZHU, H. 2003. A randomised clinical trial of high-intensity focused ultrasound ablation for the treatment of patients with localised breast cancer. *Br J Cancer,* 89**,** 2227-2233.

WU, J., ROSS, J. P. & CHIU, J.-F. 2002. Reparable sonoporation generated by microstreaming. *The Journal of the Acoustical Society of America,* 111**,** 1460-1464.

WU, S.-Y., TUNG, Y.-S., MARQUET, F., DOWNS, M. E., SANCHEZ, C. S., CHEN, C., FERRERA, V. & KONOFAGOU, E. 2014. Transcranial cavitation detection in primates during blood-brain barrier opening-a performance assessment study. *Ultrasonics, Ferroelectrics, and Frequency Control, IEEE Transactions on,* 61**,** 966-978.

WUST, P., HILDEBRANDT, B., SREENIVASA, G., RAU, B., GELLERMANN, J., RIESS, H., FELIX, R. & SCHLAG, P. M. 2002. Hyperthermia in combined treatment of cancer. *The Lancet Oncology,* 3**,** 487-497.

YANG, X., ROY, R. A. & HOLT, R. G. 2004. Bubble dynamics and size distributions during focused ultrasound insonation. *The Journal of the Acoustical Society of America,* 116**,** 3423-3431.

YIN, H., QIAO, Y., CAO, H., LI, Z. & WAN, M. 2014. Cavitation mapping by sonochemiluminescence with less bubble displacement induced by acoustic radiation force in a 1.2 MHz HIFU. *Ultrasonics sonochemistry,* 21**,** 559-565.

YOSHIDA, K., MORIOKA, S., KAGAWA, Y., KOYAMA, D. & WATANABE, Y. 2015. Power-law dependence describing subharmonic generation from a non-spherically oscillating bubble. *Acoustical Science and Technology,* 36**,** 191-200.

YOSHIZAWA, S., IKEDA, T., ITO, A., OTA, R., TAKAGI, S. & MATSUMOTO, Y. 2009. High intensity focused ultrasound lithotripsy with cavitating microbubbles. *Medical & biological engineering & computing,* 47**,** 851-860.

YOUNG, F. 1989. Cavitation. McGraw-Hill, New York.

ZEQIRI, B. & BOND, A. D. 1992. The influence of waveform distortion on hydrophone spatial-averaging corrections—Theory and measurement. *The Journal of the Acoustical Society of America,* 92**,** 1809-1821.

ZHOU, Y. 2012. Reduction of bubble cavitation by modifying the diffraction wave from a lithotripter aperture. *Journal of Endourology,* 26**,** 1075-1084.

ZHOU, Y. & GAO, X. W. 2013. Variations of bubble cavitation and temperature elevation during lesion formation by high-intensity focused ultrasound. *The Journal of the Acoustical Society of America,* 134**,** 1683-1694.

ZISKIN, M. C. 2003. Specification of acoustic output level and measurement uncertainty in ultrasonic exposimetry. *Ultrasonics, Ferroelectrics, and Frequency Control, IEEE Transactions on,* 50**,** 1023-1034.